APPLICATION OF MOMENTUM POTENTIAL THEORY IN THE STUDY OF HYPERSONIC BOUNDARY LAYER INSTABILITIES

Long Tiehan

PhD

The Hong Kong Polytechnic University

2022

The Hong Kong Polytechnic University

Department of Mechanical Engineering

APPLICATION OF MOMENTUM POTENTIAL THEORY IN THE STUDY OF HYPERSONIC BOUNDARY LAYER INSTABILITIES

Long Tiehan

A thesis submitted in partial fulfillment of the

requirements for the degree of Doctor of Philosophy

August 2021

CERTIFICATE OF ORIGINALITY

I hereby declare that this thesis is my work and that, to the best of my knowledge and belief, it reproduces no material previously published or written, nor material that has been accepted for the award of any other degree or diploma, except where due acknowledgment has been made in the text.

(Signed)

Long Tiehan

(Name of student)

Acknowledgments

My deepest gratitude goes first and foremost to my supervisor, Prof. Wen Chih-Yung, for encouraging me to explore and appreciate life in itself. Without his constant encouragement and guidance, this thesis could not reach its present form.

Second, I would like to thank our collaborators, Dr. Zhao Rui and Dr. Hao Jiaao, for their invaluable assistance throughout my Ph.D. study. I have benefited a great deal from their professional knowledge in DNS.

On a more personal level, I must acknowledge the role of my beloved family in my development and education. Special appreciation should go to my girlfriend, Dr. Yao Yao, for her nonfungible accompanies over this period. I also owe my sincere gratitude to all my friends here at PolyU. Their friendship has made my stay in PolyU enjoyable.

Abstract

This thesis improves the momentum potential theory (MPT) proposed by Doak to study the physical mechanism underlying high-speed boundary layer instabilities. The MPT approach decomposes random disturbances into well-defined vortical, acoustic, and thermal components and derives an energy budget equation. However, the application of the original MPT approach in the study of high-speed boundary layer instabilities in previous research is questionable. The first problem is that the effect of different source terms on different energy fluxes is not clarified. Three independent energy budget equations for each MPT component are obtained for the first time. The effect of different source terms on each energy flux is clarified and energy exchange terms between MPT components are revealed. Then, the "sound radiation" mechanism of the supersonic mode and the stabilization mechanism of the porous coating to the supersonic mode is elucidated with these independent energy budget equations. The second problem is that the growth rate of the instability mode is not related to the energy budget equation explicitly. The integral energy budget equation is thus derived to evaluate contribution of different source terms to the growth rate. The growth rate analysis is performed for the unstable S mode of a Mach 6.0 boundary layer with the adiabatic wall in the spatial LST. The result indicates that the thermal diffusion source P_{diff} plays a key role in the amplification of the unstable S mode. Furthermore, the growth rate analysis is performed for DNS results of different acoustic metasurfaces to clarify the stabilization mechanism of acoustic metasurfaces.

Publication List

Journal Paper:

1. T. Long, Y. Dong, R. Zhao, and C. Wen, "Mechanism of stabilization of porous coatings on unstable supersonic mode in hypersonic boundary layers," *Physics of Fluids*, vol. 33, no. 5, p. 054105, 2021.

2. R. Zhao, C. Y. Wen, T. H. Long, X. D. Tian, and Y. Wu, "Spatial Direct Numerical Simulation of the Hypersonic Boundary-Layer Stabilization Using Porous Coatings," *AIAA Journal*, vol. 57, no. 1, pp. 1-5, 2019.

3. X. Tian, R. Zhao, T. Long, and C. Y. Wen, "Reverse Design of Ultrasonic Absorptive Coating for the Stabilization of Mack Modes," *AIAA Journal*, vol. 57, no. 6, pp. 2264-2269, 2019.

Contents

Nomenclatures

a	=	local speed of sound, m/s
C_p	=	specific heat at constant pressure, J/(kg·K)
c	=	phase speed, m/s
f	=	frequency, Hz
H	=	total enthalpy per unit mass, J/kg
h	=	specific enthalpy per unit mass, J/kg
e	=	internal energy per unit mass, J/kg
M_r	=	relative Mach number
M	=	Mach number
Re	=	Reynolds number
ρ	=	density, kg/m^3
T	=	temperature, K
p	=	pressure, Pa
$\boldsymbol{m}$	=	momentum density, kg/(m^2·s)
$\boldsymbol{m}'_A$	=	the acoustic component of momentum density, kg/(m^2·s)
$\boldsymbol{m}'_B$	=	the vortical component of momentum density, kg/(m^2·s)
$\boldsymbol{m}'_T$	=	the thermal component of momentum density, kg/(m^2·s)
R	=	gas constant of air, J/(kg·K)
S	=	entropy, J/(kg·K)
$\bar{\bar{S}}$	=	viscous stress tensor, kg/(m·s^2)
t	=	time, s
u	=	streamwise velocity, m/s
v	=	normal velocity, m/s
x	=	streamwise coordinate, m
y	=	normal coordinate, m
$\boldsymbol{u}$	=	velocity vector, m/s
$\boldsymbol{a}$	=	acceleration vector, m/s^2

α = streamwise wavenumber, m^{-1}

β = spanwise wavenumber, m^{-1}

ω = circular frequency, s^{-1}

$\boldsymbol{\Omega}$ = vorticity vector, s^{-1}

σ = growth rate, m^{-1}

ψ = scalar potential of the momentum density, m^2/s

ψ_A = acoustic potential, m^2/s

ψ_T = thermal potential, m^2/s

γ = specific heat ratio

Superscripts

$'$ = fluctuation quantity

$\bar{}$ = mean quantity

Subscripts

$_\infty$ = freestream quantity

$_w$ = wall quantity

1. Introduction

1.1 Background

High-speed boundary layer (HBL) transition presents critical challenges to high-performance supersonic and hypersonic vehicles' design. Laminar-to-turbulent transition in the HBL leads to a significant increase of convective heating rates from the high-temperature air to the vehicle surface, requiring an effective thermal protection system (TPS) protect the hypersonic vehicle from burning out. The high convective heat transfer rate due to the HBL transition is illustrated in **Figure 1-1**. The heat transfer rate for a laminar boundary layer can be 40% less than that of a turbulent boundary layer on a sharp cone at M_∞=5.5 [1]. Therefore, predicting and delaying the transition in the HBL is of particular importance for the design of future supersonic and hypersonic vehicles' TPS.

Research studies of the laminar-turbulent transition mechanisms in the HBL have been a long history. Numerous investigations by experiment[2-13], linear stability theory (LST)[14-19], and direct numerical simulation (DNS)[20-26] have been conducted to understand the physic mechanisms underlying the laminar-turbulent transition in the HBL. It is generally acknowledged that the transition from the laminar flow to the turbulent flow is a multifold process developing in several paths[27].

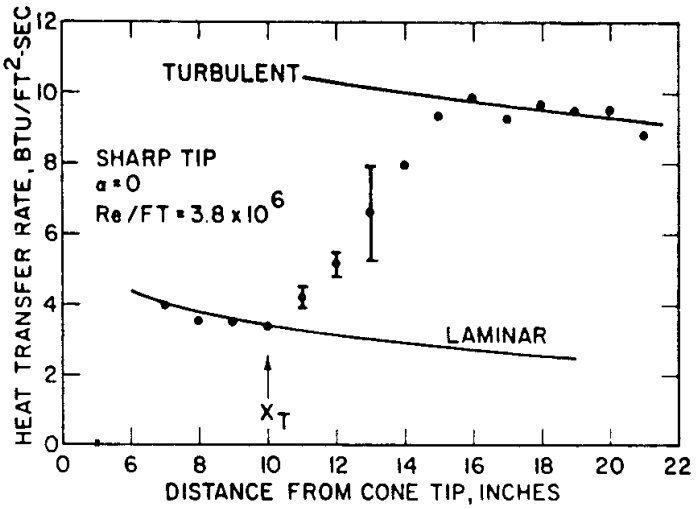

Figure 1-1. Heat transfer rate on a sharp cone at M_∞=5.5 [1]

Figure 1-2 [28] shows different ways to turbulence in boundary-layer flows depending on the environment's perturbation disturbance levels. In the free-flight case of hypersonic vehicles, disturbances in the atmosphere are usually negligible. The transition from laminar to turbulence is in the HBL is mainly through path A. Path A is the modal growth of boundary-layer instabilities, including Mack's first and second modes, the 3D crossflow instability, and the concave-wall Görtler instability. For the high-speed flow over a 2-D flat plate or an axisymmetric body, the dominant instability modes in the boundary layer are Mack's first and second modes. As the external disturbances level increases, laminar to turbulent transition will be triggered through other pathways. Path B is the transient growth of the eigenmodes in the HBL with higher-level external disturbances. Path C is the transient growth attributed to the non-orthogonal eigenmodes in the HBL. Path D is associated with the internal flows at a considerable turbulence level. Path E is the nonlinear case with such large amplitude disturbances that the linear assumption is invalid.

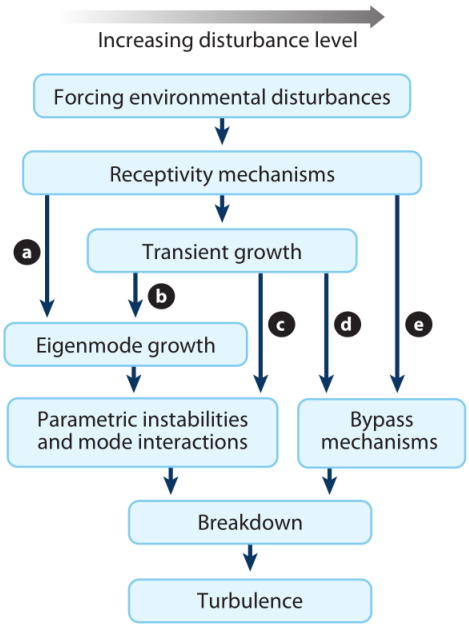

Figure 1-2. Paths to turbulence in boundary-layer flows [28]

1.2 Linear Stability Theory

When the disturbance level is low enough that the linearization assumption is valid, laminar-to-turbulent transition in the hypersonic boundary layer over a flat plate or axisymmetric cone is dominated by the modal growth of Mack's first and second modes. In this case, LST as a powerful theoretical tool is widely utilized to identify unstable boundary layer modes and analyze their downstream development.

In LST, physical quantities in the flow field $\phi(x, y, z, t)$ are divided into two parts: steady mean terms $\bar{\phi}(x, y, z)$ and small unsteady disturbance terms $\phi'(x, y, z, t)$. It can be expressed as $\phi(x, y, z, t) = \bar{\phi}(x, y, z) + \phi'(x, y, z, t)$, where x is the stream-wise direction, y is the normal direction to the wall, z is the span-wise direction and t is the time. By substituting the above equation into the Navier-Stokes (N-S) equations, the linearized N-S equations are derived by dropping the quadratic nonlinear terms. The local parallel

assumption is adopted in LST that the growth of boundary thickness is negligible and the steady mean terms $\bar{\phi}$ do not vary in the *x*-direction. Thus, the disturbance term $\phi'(x,y,z,t)$ is expressed in the harmonic waveform $\phi'(x,y,z,t) = \hat{\phi}(y)e^{i(\alpha x+\beta z-\omega t)} + c.c.$, c.c. means the complex conjugate. Here, ω is the circular frequency, α and β are the streamwise and spanwise wave number, respectively. With the local parallel assumption, the linearized N-S equations result in an eigenvalue problem. The mode solution $\hat{\phi}(y)$ and the dispersion relation $D(\alpha,\beta,\omega) = 0$ are obtained by solving the eigenvalue problem. There are two frameworks for LST. If α and β are real numbers and allowing $\omega = \omega_r + i\omega_i$ to be a complex number, a typical temporal stability analysis is performed. In this case, the mode solution with positive ω_i represents an exponential growth unstable wave. If ω and β are real numbers and allowing $\alpha = \alpha_r + i\alpha_i$ to be a complex number, it is a typical spatial stability analysis. Similarly, the mode solution with negative α_i is an exponential growth unstable wave.

1.3 Instability Modes in HBL

Mack [14] firstly identified that multiple unstable modes exist in the compressible boundary layer at a high Mach number. As shown in **Figure 1-3**, Mack's numerical study showed that the most unstable mode in the supersonic boundary layer (Mach>2.0) over the adiabatic wall is mode 2, which is referred to as Mack's second mode. Mack also found that the most unstable mode 1 (Mack's first mode), which corresponds to the Tollmien-Schlichting (TS) wave in the incompressible boundary layer, is oblique ($\beta \neq 0$) as shown in **Figure 1-4**. On the contrary, higher modes are two-dimensional ($\beta = 0$) and do not have any counterpart in the incompressible boundary layer.

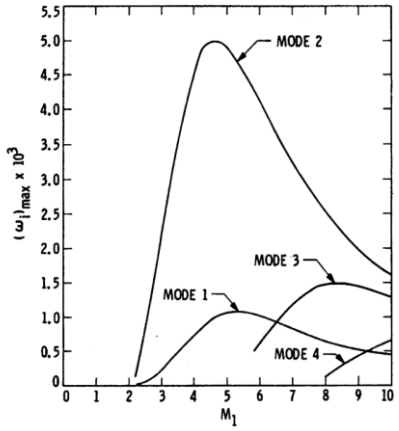

Figure 1-3. Maximum temporal amplification rate of first four two-dimensional modes in the supersonic boundary layer over the adiabatic wall. From Mack [14].

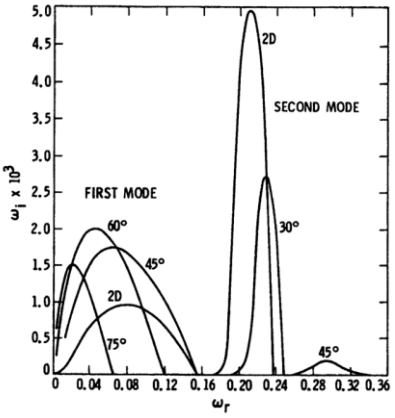

Figure 1-4. Temporal amplification rate of first and second modes for different wave angles at Mach 4.0 over the adiabatic wall. The total temperature of the freestream is 311K. From Mack [14].

Following Mack [14], the relative Mach number is defined as

$$M_r = \frac{\bar{u}(y)-c}{\bar{a}(y)} \tag{1.1}$$

Here, $\bar{u}(y)$ is the mean streamwise velocity, c is the phase speed of disturbance waves, and $\bar{a}(y)$ is local acoustic speed. In the case of Mack's second mode, there exists a sonic line, where $M_r = -1.0$, in the boundary layer. Between the sonic line and the solid wall, the mean flow is supersonic ($M_r < -1.0$) relative to the phase speed of disturbance waves. In this

supersonic region, the acoustic rays are reflected by the wall and the sonic line. Thus, the boundary layer forms a waveguide for disturbance waves. As schematically shown in **Figure 1-5**, Mack's second mode and higher modes belong to the family of acoustic waves trapped in the waveguide [27].

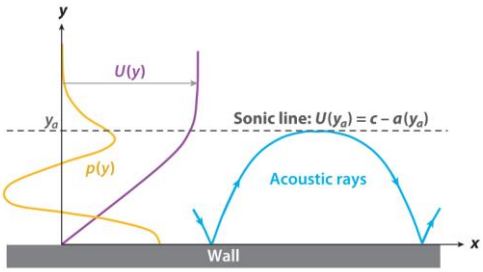

Figure 1-5. The waveguide in a high-speed boundary layer. From Fedorov [27].

Mathematically, eigen-modes can be used to expand PDE solutions. Fedorov and Tumin [18] suggest using the terminology of discrete and continuous modes instead of Mack's terminology. In the framework of spatial LST, the solution of the eigenvalue problems is a unique expansion into several discrete and continuous normal modes. Normal modes in discrete spectrum vanish as $y \to \infty$, while the continuous modes are bounded as $y \to \infty$. Figure 1-6 shows the continuous and discrete spectrum in the complex α-plane in the spatial LST framework. In **Figure 1-6**, $\alpha_{c,1}^{+}$ represent vorticity waves, $\alpha_{c,2}^{+}$ represent entropy waves, $\alpha_{c,3}^{+}$ represent fast acoustic waves, $\alpha_{c,4}^{+}$ represent slow acoustic waves, $\alpha_{c,1}^{-}$, $\alpha_{c,2}^{-}$, $\alpha_{c,3}^{-}$ represent upstream propagating waves, and α_n represent discrete modes.

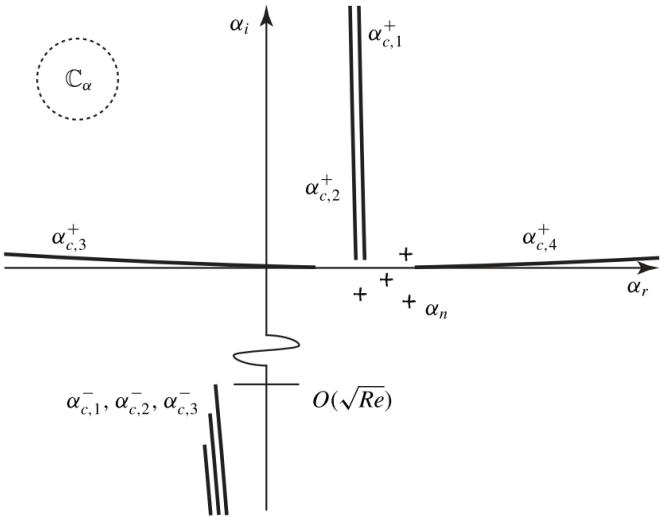

Figure 1-6. The schematic pattern of the continuous (lines) and discrete (crosses) spectrum in the complex α-plane in the spatial LST framework. From Chuvakhov and Fedorov [29].

In the discrete spectrum of spatial LST, the phase speed of one mode tends to $c_r = 1 + \frac{1}{M}$ at the leading edge of the boundary layer, which is the phase speed of fast acoustic waves in the freestream. The phase speed of the other mode tends to $c_r = 1 - \frac{1}{M}$ at the leading edge of the boundary layer, which is the phase speed of slow acoustic waves in the freestream. Thus, the former is named slow mode (S mode) and the latter is named fast mode (F mode) [18]. **Figure 1-7** shows the phase speed for slow and fast modes of the Mach 4.5 boundary layer with the adiabatic wall. As shown in **Figure 1-7**a, there are two unstable regions ($c_i < 0$) for the S mode, which corresponds to Mack's first mode and second mode respectively. In **Figure 1-7**b, the F mode synchronizes with fast sound waves in region 1 (R=0, the leading edge), whereas the S mode synchronizes with slow sound waves. As R increases, the F mode synchronizes with entropy/vorticity waves in region 2. Further downstream, the F mode synchronizes with the slow mode in region 3, which causes the most unstable Mack's second mode [18].

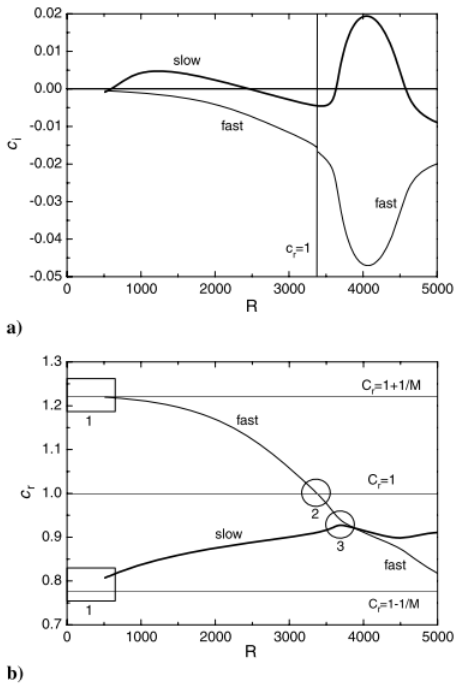

Figure 1-7. a) Imaginary and b) real parts of the phase speed, $c = \frac{\omega}{\alpha}$, for slow and fast modes at M=4.5, adiabatic wall, and the dimensionless frequency, $F = \frac{\omega}{Re}$, is 5×10^{-5} with spatial stability analysis. Here, Re is the Reynolds number based on the local boundary layer thickness. From Fedorov and Tumin [18].

1.4 Ultrasonic Absorptive Coating

As mentioned above, the desire to delay even suppress the transition in HBL is of particular importance in the design of high-performance hypersonic vehicles. Under a low disturbance environment, the modal growth of Mack's second mode is the major cause of boundary layer transition over a smooth flat plate or a sharp cone with a high Mach number. Numerous studies[30-49] have been conducted to control the laminar to turbulence transition in the HBL by suppressing the growth of Mack's second mode. Mack's second mode belongs to the family of trapped acoustic waves in the waveguide formed by the sonic line and the solid wall in the high-speed boundary layer. The wavelength of Mack's second mode is

around twice the boundary thickness, and the phase speed of Mack's second mode is slightly less than the freestream velocity. Thus, the frequency of Mack's second mode is typically on the order of 100kHz, which is in the ultrasonic frequency band. Given the acoustic nature of Mack's second mode, Malmuth, et al. [30] proposed to absorb the acoustic energy of Mack's second mode by ultrasonic porous coating (UAC). The LST analysis performed by Fedorov, et al. [31] indicated that UAC reduces the growth rate of Mack's second mode substantially. Rasheed, et al. [35] conducted boundary layer transition experiments on a sharp 5.06-deg half-angle round cone at zero angle of attack in Caltech's T5 Hypervelocity Shock Tunnel. The test cone had a smooth surface over half the cone and the UAC surface over the other half. In Figure 1-8, The resonantly enhanced shadowgraph of the flow field around the test cone showed that laminar-to-turbulence transition happened on the smooth side while the boundary layer is laminar on the porous side. The UAC was proved to be highly effective in delaying the transition dominated by Mack's second mode.

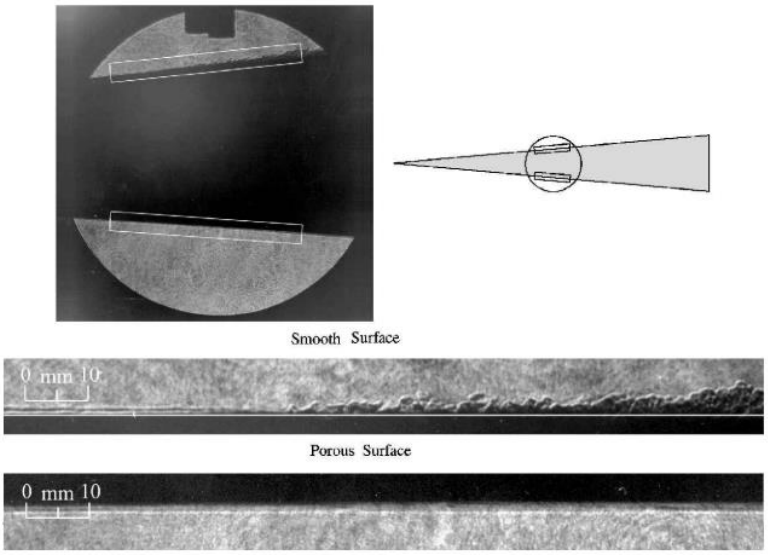

Figure 1-8. Resonantly enhanced shadowgraph of the boundary layer on the smooth side and the porous side. From [35].

Fedorov, et al. [32] studied the boundary layer transition experimentally and theoretically on a thin coating of fibrous absorbent material (felt metal) in the Mach 6 wind tunnel on a 7◦ half-angle sharp cone. This kind of UAC has a random microstructure. Their results showed that Mack's second mode is stabilized effectively by the UAC with random microstructure, while Mack's first mode is destabilized marginally. Wang and Zhong [36] compared the growth rate of S mode on regular porous coating and felt-metal porous coating by numerical simulation. It was found that regular porous coating is weaker than felt-metal porous coating in Mack's first mode destabilization and Mack's second mode stabilization. Wagner, et al. [38] confirmed that ultrasonically absorptive carbon-carbon material delays the boundary layer transition effectively in the High Enthalpy Shock Tunnel Göttingen of the German Aerospace Center (DLR) at Mach 7.5.

The stabilization effect of above mentioned UAC materials on Mack's second mode is attributed to the dissipation of acoustic energy by porous microstructure. Wang and Zhong [50] studied the effect of porous coating admittance phase angle on the boundary layer stabilization and found that the destabilization effect of Mack's first mode decreases with the phase angle of admittance decreasing. Based on the different effects of porous coating admittance phase angle on Mack's first mode and second mode, Tian, et al. [44] proposed an optimal design of UAC which stabilized Mack's second mode effectively and destabilized Mack's first mode weakly.

Besides the absorptive UAC materials, Zhao, et al. [46] found that Mack's second mode is suppressed significantly with near-zero surface acoustic impedance. When the surface acoustic impedance approaches zero, a minimum fluctuation pressure is achieved near the

surface due to the cancellation of the incident and reflected acoustic waves. As shown in Figure 1-9, the amplitude of the fluctuation pressure decreases significantly in the cavity of the absorptive UAC, while it remains almost the same intensity in the cavity of the impedance-near-zero UAC.

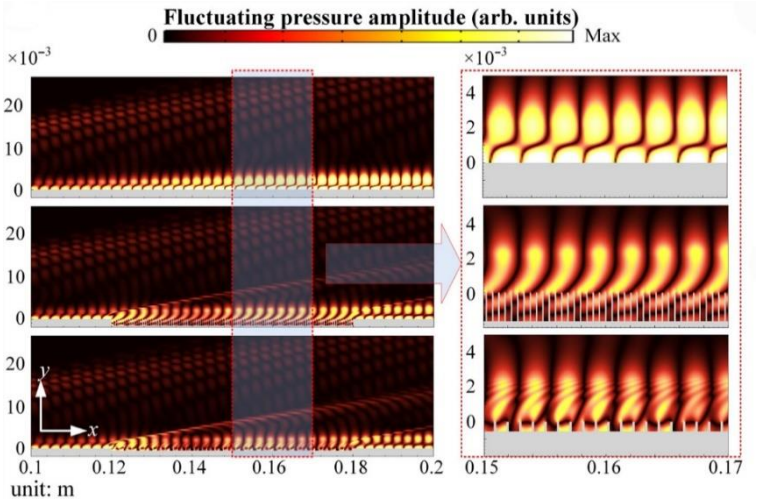

Figure 1-9. Fluctuating pressure amplitude contours for rigid boundary (upper), absorptive UAC (middle), and impedance-near-zero UAC (lower).

1.5 Energy approaches

The linear stability theory shows the existence of unstable modes in the high-speed boundary layer by giving the growth rate of these modes mathematically. However, it does not give any insight into the actual physics underlying the growth of unstable modes. There have been attempts to provide a physical interpretation of the growth of small disturbances in the flow field based on energy approaches. The first energy approach to the incompressible instability theory was originated by Reynolds [51]. In the incompressible boundary layer, the kinetic energy of a small 2D disturbance is given by multiplying the dimensionless x and y linearized momentum equations by u' and v', respectively, and add,

$$\left(\frac{\partial}{\partial t}+\bar{u}\frac{\partial}{\partial x}\right)e+u'v'\frac{\partial \bar{u}}{\partial y}=-u'\frac{\partial p'}{\partial x}-v'\frac{\partial p'}{\partial y}+\frac{1}{R}(u'\nabla^2 u'+v'\nabla^2 v') \tag{1.2}$$

Here, $e=\frac{1}{2}(u'^2+v'^2)$ is the kinetic energy of the 2D disturbance. Then, equation (1.2) is integrated from $y=0$ to infinity and is taken average over a wavelength,

$$\frac{\partial E}{\partial t}=\bar{P}-\bar{D}=\int_0^\infty \tau\frac{\partial \bar{u}}{\partial y}dy-\int_0^\infty\langle\zeta^2\rangle dy \tag{1.3}$$

Here, $E=\frac{1}{2}\langle u'^2\rangle+\frac{1}{2}\langle v'^2\rangle$ is the total disturbance kinetic energy per wavelength, $\tau=-\langle u'v'\rangle$ is the Reynolds stress, and $\zeta=\frac{\partial u'}{\partial y}-\frac{\partial v'}{\partial x}$ is the z-component of the fluctuation vorticity. The symbol $\langle\cdot\rangle$ means the average over a wavelength. In equation (1.3), $\bar{P}=\int_0^\infty \tau\frac{\partial \bar{u}}{\partial y}dy$ is the total energy production term over a wavelength due to the Reynolds stress and $\bar{D}=\int_0^\infty\langle\zeta^2\rangle dy$ is the total energy dissipated by the viscous effect. As a consequence, the small 2D disturbance in the incompressible boundary layer grows if and only if $\bar{P}$ outweigh $\bar{D}$.

Reynolds' kinetic energy approach is only applicable to the incompressible parallel flow. For the compressible boundary layer with a high Mach number, Kuehl [52] derived a Lagrangian acoustic energy equation by ignoring the viscous effect. Considering the inviscid N-S equation,

$$\frac{D\rho}{Dt}=-\rho\nabla\cdot\boldsymbol{u} \tag{1.4}$$

$$\rho\frac{D\boldsymbol{u}}{Dt}=-\nabla p \tag{1.5}$$

$$\rho\frac{DT}{Dt}-\frac{1}{C_p}\frac{Dp}{Dt}=0 \tag{1.6}$$

Following below steps:

$$\boldsymbol{u}\cdot(1.4)+R(T\cdot(1.4)+(1.6))$$

The acoustic energy equation is derived as

$$\frac{1}{2}\rho\frac{D\boldsymbol{u}^2}{Dt}+\frac{1}{2\rho a^2}\frac{Dp^2}{Dt}+\nabla\cdot(p\boldsymbol{u})=0 \tag{1.7}$$

where $\frac{D}{Dt}$ is the material derivative, $a=\gamma RT$ is the sound speed, and γ is the ratio of specific

heat. The first two terms on the left-hand side are the Lagrangian derivative of acoustic energy and the third term represents the divergence of acoustic power.

From equation (1.7), one can derive the ideal gas, one-dimensional (1-D), parallel flow cycle-averaged disturbance acoustic energy equation:

$$\frac{D\langle e\rangle}{Dt} = -\left[\frac{d}{dy}(\bar{\rho}\langle T'v'\rangle) + \frac{d}{dy}(\bar{T}\langle \rho'v'\rangle)\right] \tag{1.8}$$

where,

$$\langle e\rangle = \frac{1}{2}\bar{\rho}\langle \boldsymbol{u}'^2\rangle + \frac{1}{2\bar{\rho}\bar{a}^2}\langle p'^2\rangle \tag{1.9}$$

is the disturbance energy norm adopted by Kuehl [52]. Compared to equation (1.3), the thermoacoustic Reynolds stresses $\langle T'v'\rangle$ and $\langle \rho'v'\rangle$ in equation (1.8) plays the similar roles as the viscous Reynolds stress $\tau = -\langle u'v'\rangle$.

With the Lagrangian acoustic energy equation (1.8), Kuehl [52] showed that Mack's second mode is related to a forced, resonating, thermoacoustic standing wave trapped in a thermoacoustic impedance well which is formed by the sonic line and the solid wall. The thermoacoustic Reynold stress derives energy from the mean flow, which is the energy source for the amplification of Mack's second mode. Kuehl's Lagrangian acoustic energy equation provides an insight into the physic mechanism of Mack's second mode growth in the compressible boundary layer with a high Mack number. However, viscosity is not included in Kuehl's approach.

Tian and Wen [53] performed the stability analysis for Mack's second mode in a Mach 6.0 boundary layer based on the fluctuating internal energy. Mack's second mode has the largest growth rate when the wall-normal transport of energy is in phase to the change in fluctuating internal energy in the vicinity of the critical layer, similar to the mechanism of the

Rijke tube in generating acoustic waves.

Doak's momentum potential theory (MPT) [54] provides a completed description of the development of disturbances in time-stationary fluctuating flows. By decomposing the fluctuation momentum density into its vortical, acoustic, and thermal components, a mean energy balance equation is derived for the mean (time-averaged) energy flux carried by momentum fluctuations can be expressed as a linear superposition of vortical, acoustic and thermal energy fluxes. MPT approach is firstly introduced to the study of the instability of high-speed boundary layer by Unnikrishnan and Gaitonde [55]. By applying MPT for LST and DNS results, Unnikrishnan and Gaitonde found that the vortical component displays a series of rope-shaped recirculation-cell patterns in the boundary layer, while both acoustic and thermal components display 'trapped' structures. Furthermore, Unnikrishnan and Gaitonde examined source terms in the boundary layer with different wall temperatures based on MPT's energy budget equation and claimed that the thermal source is the primary source to the growth of Mack's second mode. However, their conclusion on the energy source for Mack's second mode is quite doubtful. The original energy budget equation in Doak [54] is restricted to the interpretation for the growth of disturbances because the growth rate of unstable modes is not explicitly linked to source terms in Doak's MPT energy budget equation. Different from the energy norm defined in Reynolds' kinetic energy approach and Kuelh's Lagrangian's approach, the energy fluxes in Doak's MPT approach are not positive definite, which makes it difficult to identify the effect of source terms on the amplification of disturbances. With above problems, the physic interpretation for the instability mechanism of high speed boundary layer based on Doak's original MPT approach is not logically consistent.

1.6 Overview

This introductory chapter has given a brief introduction to the unstable modes in the high-speed boundary layer and different UAC materials that stabilize Mack's second mode effectively. Then, energy approaches that aim to provide a physical interpretation for the boundary layer instability mechanism are reviewed. Among these energy approaches, Doak's MPT approach is an elegant method that provides a physical description of the development of disturbances in the high-speed boundary layer. However, the energy fluxes and source terms in Doak's MPT approach are not explicitly linked to key features of unstable modes. For this reason, the original energy budget equation in Doak's MPT approach is still questionable to give a substantial interpretation for the development of disturbances in the boundary layer. The primary object of this work is to develop the MPT approach for a substantial and self-consistent physical interpretation of the instability mechanism of the high-speed boundary layer. In chapter 2, the MPT approach proposed by Doak [54] is reviewed in detail. This includes 1) the decomposition of the momentum density into the vortical, acoustic, and thermal components, and 2) the energy budget equation that governs the balance between mean energy fluxes and source terms. Besides the original energy budget equation proposed by Doak [54], three independent energy budget equations for each component are derived for the first time to clarify the effect of source terms on mean fluxes. In chapter 3, three independent energy budget equations are implemented to DNS results of the supersonic mode over the highly cooled wall. The sound radiation mechanism of the supersonic mode is clarified under MPT's framework. In chapter 4, the integration form of MPT's energy budget equation is developed to study the growth rate of Mack's second mode in LST. The source

term that is responsible for the growth of Mack's second mode is identified. In chapter 5, the integration form of MPT's energy budget equation is implemented to the DNS results of both the solid wall case and porous wall cases. The different stabilization mechanisms of different UAC structures are revealed. Finally, chapter 6 gives a summary of the current work.

2. Momentum potential theory

2.1 MPT decomposition

It is generally acknowledged that Mack's second mode and higher modes belong to the family of trapped acoustic waves in the waveguide formed by the sonic line and the solid wall. However, the term "acoustic wave" adopted here is not well defined. Kovásznauy [56] showed that random fluctuations in the flow field with uniform mean velocity and temperature can be decomposed into vorticity, entropy, and acoustic modes. Under the small disturbance assumption, the interaction between different modes is negligible and the modes obey three independent governing equations. If the intensity of fluctuation is large that the linear assumption is invalid, quadratic interaction terms between different modes appear in the governing equation as source terms. However, Kovásznay's approach is not suitable for extension to the boundary layer flows, where the gradient of mean velocity and mean temperature are strong. In the flow field with a strong gradient, complicated interaction terms exist between different modes even fluctuations are small.

The MPT approach proposed by Doak [54] overcomes the restriction in Kovásznay's approach for a general flow which is time stationary. In the time stationary flow, any physic quantity ϕ can be expressed as the sum of the time-averaged quantity $\bar{\phi}$ and the fluctuation quantity ϕ'. The time-averaged term $\bar{\phi}$ is independent on time t. In Doak's MPT approach, the momentum density, $\boldsymbol{m} = \rho \boldsymbol{u}$, is split into its vortical, acoustic, and thermal components. Considering the continuity equation,

$$\frac{\partial \rho}{\partial t} + \nabla \cdot \boldsymbol{m} = 0 \tag{2.1}$$

Then, the vector field $\boldsymbol{m}$ is decomposed into the rotational part $\boldsymbol{m}_B$ and irrotational part $-\nabla\varphi$ through the Helmholtz decomposition.

$$\boldsymbol{m} = \boldsymbol{m}_B - \nabla\varphi, \nabla \cdot \boldsymbol{m}_B = 0 \tag{2.2}$$

Here, the scalar field φ is the momentum potential.

The time average of equation (2.1) is

$$\nabla \cdot \bar{\boldsymbol{m}} = 0 \tag{2.3}$$

The vector field $\bar{\boldsymbol{m}} = \bar{\boldsymbol{m}}_B$ is solenoidal. Thus, the fluctuation momentum density $\boldsymbol{m}'$ is expressed as

$$\boldsymbol{m}' = \boldsymbol{m}'_B - \nabla\varphi, \nabla \cdot \boldsymbol{m}'_B = 0 \tag{2.4}$$

Subtract equation (2.1) by equation (2.3), we have the fluctuation continuity equation

$$\frac{\partial \rho'}{\partial t} + \nabla \cdot \boldsymbol{m}' = 0 \tag{2.5}$$

Furthermore, substitute equation (2.4) into equation (2.5), we obtain the Poisson equation

$$\frac{\partial \rho'}{\partial t} = \nabla^2\varphi \tag{2.6}$$

For a general flow in the thermal equilibrium state, we can express the density ρ as the function of the pressure p and the entropy S.

$$\rho = \rho(p, S) \tag{2.7}$$

With the small disturbance assumption, we have

$$\rho' = \left(\frac{\partial \rho}{\partial p}\right)_S p' + \left(\frac{\partial \rho}{\partial S}\right)_p S' \tag{2.8}$$

Here,

$$\left(\frac{\partial \rho}{\partial p}\right)_S = \frac{1}{\bar{a}^2} = \frac{1}{\gamma R \bar{T}}, \left(\frac{\partial \rho}{\partial S}\right)_p = -\frac{(\gamma-1)\bar{\rho}}{\gamma R} \tag{2.9}$$

Hence, equation (2.6) can be written as

$$\frac{1}{\bar{a}^2}\frac{\partial p'}{\partial t} - \frac{(\gamma-1)\bar{\rho}}{\gamma R}\frac{\partial S'}{\partial t} = \nabla^2\varphi \tag{2.10}$$

Because the momentum potential φ is linear in equation (2.10), φ can be regarded as the linear superposition of uniquely defined acoustic component φ_A and thermal component φ_T.

$$\varphi = \varphi_A + \varphi_T, \frac{1}{\bar{a}^2}\frac{\partial p'}{\partial t} = \nabla^2\varphi_A, -\frac{(\gamma-1)\bar{\rho}}{\gamma R}\frac{\partial S'}{\partial t} = \nabla^2\varphi_T \tag{2.11}$$

As a consequence, the fluctuation momentum density $\boldsymbol{m}'$ can be written as the sum of the vortical component $\boldsymbol{m}'_B$, the acoustic component $\boldsymbol{m}'_A$, and the thermal component $\boldsymbol{m}'_T$.

$$\boldsymbol{m}' = \boldsymbol{m}'_B + \boldsymbol{m}'_A + \boldsymbol{m}'_T, \nabla \cdot \boldsymbol{m}'_B = 0, \boldsymbol{m}'_A = -\nabla\varphi_A, \boldsymbol{m}'_T = -\nabla\varphi_T \tag{2.12}$$

Vortical component $\boldsymbol{m}'_B$ is solenoidal, isobaric, and isentropic. Acoustic component $\boldsymbol{m}'_A$ represents the irrotational and isentropic part of $\boldsymbol{m}'$, which is related to the fluctuation pressure p' in the flow field. Thermal component $\boldsymbol{m}'_T$ represents the irrotational and isobaric part of $\boldsymbol{m}'$, which is related to the fluctuation entropy S' in the flow field.

The definition of momentum potential φ can be extended into the multi-chemical-component flow with chemical reaction by expressing the fluctuation density ρ' in the form

$$\rho = \rho(p, S, \alpha, \beta, \cdots) \tag{2.13}$$

$\alpha, \beta, \cdots$ are chemical-component concentrations or other suitable independent thermodynamic variables. Consequently, equation (2.8) can be rewritten as

$$\rho' = \left(\frac{\partial\rho}{\partial p}\right)_{S,\alpha,\beta,\cdots} p' + \left(\frac{\partial\rho}{\partial S}\right)_{p,\alpha,\beta,\cdots} S' + \left(\frac{\partial\rho}{\partial\alpha}\right)_{p,S,\beta,\cdots} \alpha' + \left(\frac{\partial\rho}{\partial\beta}\right)_{p,S,\alpha,\cdots} \beta' + \cdots \tag{2.14}$$

and the definitions (2.11) can be extended to

$$\varphi = \varphi_A + \varphi_T + \varphi_\alpha + \varphi_\beta + \cdots$$

$$\left(\frac{\partial\rho}{\partial\alpha}\right)_{p,S,\beta,\cdots}\frac{\partial\alpha'}{\partial t} = \nabla^2\varphi_\alpha, \left(\frac{\partial\rho}{\partial\beta}\right)_{p,S,\alpha,\cdots}\frac{\partial\beta'}{\partial t} = \nabla^2\varphi_\beta, \cdots \tag{2.15}$$

Similarly, we can define components related to chemical components $\boldsymbol{m}'_\alpha, \boldsymbol{m}'_\beta, \cdots$ as

$$\boldsymbol{m}'_\alpha = -\nabla\varphi_\alpha, \boldsymbol{m}'_\beta = -\nabla\varphi_\beta, \cdots \tag{2.16}$$

2.2 MPT energy budget equation

Besides the MPT decomposition which provides a unique definition of vortical, acoustic, and thermal components in a general time-stationary flow, the other important aspect of the MPT approach is the energy budget equation governing the fluctuation energy transported by different components. The derivation of the energy budget equation is reviewed as follows.

Firstly, considering the momentum conservation equation

$$\frac{\partial \boldsymbol{u}}{\partial t} + (\boldsymbol{u} \cdot \nabla)\boldsymbol{u} = -\frac{1}{\rho}\nabla p + \frac{1}{\rho}\nabla \cdot \overline{\overline{\boldsymbol{S}}} \tag{2.17}$$

Here, $\overline{\overline{\boldsymbol{S}}}$ is the viscous stress tensor.

Since

$$(\boldsymbol{u} \cdot \nabla)\boldsymbol{u} = \boldsymbol{\Omega} \times \boldsymbol{u} + \nabla\left(\frac{\boldsymbol{u}^2}{2}\right) \tag{2.18}$$

and

$$\nabla h = T\nabla S + \frac{1}{\rho}\nabla p \tag{2.19}$$

Equation (2.17) can be expressed as

$$\frac{\partial \boldsymbol{u}}{\partial t} + \nabla\left(\frac{\boldsymbol{u}^2}{2} + h\right) = -\boldsymbol{\Omega} \times \boldsymbol{u} + T\nabla S + \frac{1}{\rho}\nabla \cdot \overline{\overline{\boldsymbol{S}}} \tag{2.20}$$

Here, $\boldsymbol{\Omega} = \nabla \times \boldsymbol{u}$ is the vorticity vector and $-\boldsymbol{\Omega} \times \boldsymbol{u}$ is the Coriolis acceleration. h is the enthalpy per unit mass.

For the convenience of discussion, equation (2.20) is rewritten as

$$\frac{\partial \boldsymbol{u}}{\partial t} + \nabla H = \boldsymbol{\alpha} \tag{2.21}$$

Here, $H = \frac{\boldsymbol{u}^2}{2} + h$ is the total enthalpy per unit mass and $\boldsymbol{\alpha} = -\boldsymbol{\Omega} \times \boldsymbol{u} + T\nabla S + \frac{1}{\rho}\nabla \cdot \overline{\overline{\boldsymbol{S}}}$ is the so-called “acceleration” vector.

Thus, the fluctuation momentum conservation equation is

$$\frac{\partial \boldsymbol{u}'}{\partial t} + \nabla H' = \boldsymbol{\alpha}' \tag{2.22}$$

Taking the scalar production of equation (2.22) and the fluctuation momentum density $\boldsymbol{m}'$

$$\boldsymbol{m}' \cdot \frac{\partial \boldsymbol{u}'}{\partial t} + \boldsymbol{m}' \cdot \nabla H' = \boldsymbol{m}' \cdot \boldsymbol{\alpha}' \tag{2.23}$$

From equation (2.23), we have

$$\frac{\partial}{\partial t}(\boldsymbol{m}' \cdot \boldsymbol{u}') + \nabla \cdot (\boldsymbol{m}' H') - \boldsymbol{u}' \cdot \frac{\partial \boldsymbol{m}'}{\partial t} - (\nabla \cdot \boldsymbol{m}')H' = \boldsymbol{m}' \cdot \boldsymbol{\alpha}' \tag{2.24}$$

Noting that

$$\boldsymbol{m}' = \bar{\rho}\boldsymbol{u}' + \bar{\boldsymbol{u}}\rho' \tag{2.25}$$

With the continuity equation (2.5) and equation (2.25),

$$\frac{\partial}{\partial t}\left(\boldsymbol{m}' \cdot \boldsymbol{u}' - \frac{1}{2}\bar{\rho}\boldsymbol{u}'^2\right) + \nabla \cdot (\boldsymbol{m}' H') + h' \frac{\partial \rho'}{\partial t} = \boldsymbol{m}' \cdot \boldsymbol{\alpha}' \tag{2.26}$$

The time-average of equation (2.26) is

$$\nabla \cdot \left(\overline{\boldsymbol{m}' H'}\right) + \overline{h' \frac{\partial \rho'}{\partial t}} = \overline{\boldsymbol{m}' \cdot \boldsymbol{\alpha}'} \tag{2.27}$$

It is easy to obtain that

$$\overline{h' \frac{\partial \rho'}{\partial t}} = -\overline{\frac{p'}{R}} \overline{\frac{\partial S'}{\partial t}} \tag{2.28}$$

Finally, we get the energy budget equation

$$\nabla \cdot \left(\overline{\boldsymbol{m}' H'}\right) = \overline{\boldsymbol{m}' \cdot \boldsymbol{\alpha}'} + \overline{\frac{p'}{R}} \overline{\frac{\partial S'}{\partial t}} \tag{2.29}$$

Because $\boldsymbol{m}'$ is the linear superposition of the vortical component $\boldsymbol{m}'_B$, the acoustic component $\boldsymbol{m}'_A$, and the thermal component $\boldsymbol{m}'_T$, the energy budget equation (2.29) can be expressed as

$$\nabla \cdot \left(\overline{\boldsymbol{m}'_B H'} + \overline{\boldsymbol{m}'_A H'} + \overline{\boldsymbol{m}'_T H'}\right) = \overline{\boldsymbol{m}'_B \cdot \boldsymbol{\alpha}'} + \overline{\boldsymbol{m}'_A \cdot \boldsymbol{\alpha}'} + \overline{\boldsymbol{m}'_T \cdot \boldsymbol{\alpha}'} + \overline{\frac{p'}{R}} \overline{\frac{\partial S'}{\partial t}} \tag{2.30}$$

On the left-hand side of equation (2.30), $\overline{\boldsymbol{m}'_B H'}$, $\overline{\boldsymbol{m}'_A H'}$, and $\overline{\boldsymbol{m}'_T H'}$ are fluctuation energy fluxes carried by $\boldsymbol{m}'_B$, $\boldsymbol{m}'_A$, and $\boldsymbol{m}'_T$, respectively. On the right-hand side, $\overline{\boldsymbol{m}'_B \cdot \boldsymbol{\alpha}'}$, $\overline{\boldsymbol{m}'_A \cdot \boldsymbol{\alpha}'}$, and $\overline{\boldsymbol{m}'_T \cdot \boldsymbol{\alpha}'}$ are source terms due to $\boldsymbol{m}'_B$, $\boldsymbol{m}'_A$, and $\boldsymbol{m}'_T$, respectively. The additional source term

$\overline{\frac{p'}{R}\frac{\partial S'}{\partial t}}$ is the source term due to the thermal diffusion process. Source terms represent the energy exchange between disturbances and mean flow.

2.3 Decomposition of fluctuation velocity $\boldsymbol{u'}$

The energy budget equation (2.30) proposed by Doak obtains an energy balance between energy fluxes and source terms. The existence of multiple energy fluxes, as well as source terms, makes it hard to clarify how the energy flux due to each component is affected by different source terms. Hence, the independent energy budget equation for each component is pursued to remove the ambiguity in the equation (2.30).

First of all, the fluctuation velocity $\boldsymbol{u'}$ is decomposed into different parts corresponding to different components of $\boldsymbol{m'}$. From equation (2.25),

$$\boldsymbol{u'} = \frac{\boldsymbol{m'}}{\bar{\rho}} - \frac{\bar{\boldsymbol{u}}}{\bar{\rho}}\rho' = \frac{\boldsymbol{m'}}{\bar{\rho}} - \frac{\bar{\boldsymbol{u}}}{\bar{\rho}}\left(\frac{p'}{\gamma R\bar{T}} - \frac{(\gamma-1)\bar{\rho}S'}{\gamma R}\right) \tag{2.31}$$

Based on equation (2.31), we define

$$\begin{cases} \boldsymbol{u}'_B = \frac{\boldsymbol{m}'_B}{\bar{\rho}} \\ \boldsymbol{u}'_A = \frac{\boldsymbol{m}'_A}{\bar{\rho}} - \frac{\bar{\boldsymbol{u}}}{\gamma\bar{p}}p' \\ \boldsymbol{u}'_T = \frac{\boldsymbol{m}'_T}{\bar{\rho}} + \frac{(\gamma-1)\bar{\boldsymbol{u}}}{\gamma R}S' \end{cases}, \boldsymbol{u'} = \boldsymbol{u}'_B + \boldsymbol{u}'_A + \boldsymbol{u}'_T \tag{2.32}$$

2.4 Vortical energy budget equation

Taking the scalar production of equation (2.22) and the fluctuation momentum density $\boldsymbol{m}'_B$

$$\boldsymbol{m}'_B \cdot \frac{\partial \boldsymbol{u'}}{\partial t} + \boldsymbol{m}'_B \cdot \nabla H' = \boldsymbol{m}'_B \cdot \boldsymbol{\alpha'} \tag{2.33}$$

Equation (2.33) can be rewritten as

$$\frac{\partial}{\partial t}(\boldsymbol{m}'_B \cdot \boldsymbol{u'}) - \boldsymbol{u'} \cdot \frac{\partial \boldsymbol{m}'_B}{\partial t} + \nabla \cdot (\boldsymbol{m}'_B H') = \boldsymbol{m}'_B \cdot \boldsymbol{\alpha'} \tag{2.34}$$

The second term on the left-hand side of equation (2.34)

$$\boldsymbol{u}' \cdot \frac{\partial \boldsymbol{m}_B'}{\partial t} = (\boldsymbol{u}_B' + \boldsymbol{u}_A' + \boldsymbol{u}_T') \cdot \bar{\rho} \frac{\partial \boldsymbol{u}_B'}{\partial t} \tag{2.35}$$

Instituting equation (2.35) into equation (2.34), we have

$$\frac{\partial}{\partial t}\left(\boldsymbol{m}_B' \cdot \boldsymbol{u}' - \frac{1}{2}\bar{\rho}\boldsymbol{u}_B'^{\,2}\right) + \nabla \cdot (\boldsymbol{m}_B' H') = \boldsymbol{m}_B' \cdot \boldsymbol{\alpha}' + \bar{\rho}\boldsymbol{u}_A' \cdot \frac{\partial \boldsymbol{u}_B'}{\partial t} + \bar{\rho}\boldsymbol{u}_T' \cdot \frac{\partial \boldsymbol{u}_B'}{\partial t} \tag{2.36}$$

Taking the time-average of equation (2.36), we obtain

$$\nabla \cdot \left(\overline{\boldsymbol{m}_B' H'}\right) = \overline{\boldsymbol{m}_B' \cdot \boldsymbol{\alpha}'} + \bar{\rho}\overline{\boldsymbol{u}_A' \cdot \frac{\partial \boldsymbol{u}_B'}{\partial t}} + \bar{\rho}\overline{\boldsymbol{u}_T' \cdot \frac{\partial \boldsymbol{u}_B'}{\partial t}} \tag{2.37}$$

The vortical energy flux $\overline{\boldsymbol{m}_B' H'}$ is governed by the vortical source $\overline{\boldsymbol{m}_B' \cdot \boldsymbol{\alpha}'}$ and two additional source terms. Additional source terms $\bar{\rho}\overline{\boldsymbol{u}_A' \cdot \frac{\partial \boldsymbol{u}_B'}{\partial t}}$ and $\bar{\rho}\overline{\boldsymbol{u}_T' \cdot \frac{\partial \boldsymbol{u}_B'}{\partial t}}$ don't present in Doak's energy budget equation (2.30).

2.5 Acoustic energy budget equation

Taking the scalar production of equation (2.22) and the fluctuation momentum density $\boldsymbol{m}_A'$

$$\boldsymbol{m}_A' \cdot \frac{\partial \boldsymbol{u}'}{\partial t} + \boldsymbol{m}_A' \cdot \nabla H' = \boldsymbol{m}_A' \cdot \boldsymbol{\alpha}' \tag{2.38}$$

Rewriting equation (2.38) as

$$\frac{\partial}{\partial t}(\boldsymbol{m}_A' \cdot \boldsymbol{u}') - \boldsymbol{u}' \cdot \frac{\partial \boldsymbol{m}_A'}{\partial t} + \nabla \cdot (\boldsymbol{m}_A' H') - (\nabla \cdot \boldsymbol{m}_A')H' = \boldsymbol{m}_A' \cdot \boldsymbol{\alpha}' \tag{2.39}$$

In the left-hand side of equation (2.39), we have

$$\boldsymbol{u}' \cdot \frac{\partial \boldsymbol{m}_A'}{\partial t} = \boldsymbol{u}' \cdot \left(\bar{\rho}\frac{\partial \boldsymbol{u}_A'}{\partial t} + \frac{\overline{\boldsymbol{u}}}{\bar{a}^2}\frac{\partial p'}{\partial t}\right) \tag{2.40}$$

$$(\nabla \cdot \boldsymbol{m}_A')H' = -\frac{1}{\bar{a}^2}\frac{\partial p'}{\partial t}(h' + \overline{\boldsymbol{u}} \cdot \boldsymbol{u}') \tag{2.41}$$

Hence, equation (2.39) is rewritten as

$$\frac{\partial}{\partial t}(\boldsymbol{m}_A' \cdot \boldsymbol{u}') + \nabla \cdot (\boldsymbol{m}_A' H') = \boldsymbol{m}_A' \cdot \boldsymbol{\alpha}' + \bar{\rho}\boldsymbol{u}_B' \cdot \frac{\partial \boldsymbol{u}_A'}{\partial t} + \bar{\rho}\boldsymbol{u}_T' \cdot \frac{\partial \boldsymbol{u}_A'}{\partial t} - \frac{h'}{\bar{a}^2}\frac{\partial p'}{\partial t} \tag{2.42}$$

The time-average of equation (2.42) is

$$\nabla \cdot \left(\overline{\boldsymbol{m}_A' H'}\right) = \overline{\boldsymbol{m}_A' \cdot \boldsymbol{\alpha}'} + \bar{\rho}\overline{\boldsymbol{u}_B' \cdot \frac{\partial \boldsymbol{u}_A'}{\partial t}} + \bar{\rho}\overline{\boldsymbol{u}_T' \cdot \frac{\partial \boldsymbol{u}_A'}{\partial t}} - \overline{\frac{h'}{\bar{a}^2}\frac{\partial p'}{\partial t}} \tag{2.43}$$

The fourth term on the right-hand side of equation (2.43) satisfies

$$\overline{\frac{h'}{\bar{a}^2}\frac{\partial p'}{\partial t}} = \overline{\frac{S'}{\gamma R}\frac{\partial p'}{\partial t}} = -\overline{\frac{p'}{\gamma R}\frac{\partial S'}{\partial t}} \tag{2.44}$$

Finally, we have

$$\nabla \cdot \left(\overline{\boldsymbol{m}_A' H'}\right) = \overline{\boldsymbol{m}_A' \cdot \boldsymbol{\alpha}'} + \bar{\rho}\overline{\boldsymbol{u}_B' \cdot \frac{\partial \boldsymbol{u}_A'}{\partial t}} + \bar{\rho}\overline{\boldsymbol{u}_T' \cdot \frac{\partial \boldsymbol{u}_A'}{\partial t}} + \overline{\frac{p'}{\gamma R}\frac{\partial S'}{\partial t}} \tag{2.45}$$

The acoustic energy flux $\overline{\boldsymbol{m}_A' H'}$ is governed by the acoustic source $\overline{\boldsymbol{m}_A' \cdot \boldsymbol{\alpha}'}$, $\bar{\rho}\overline{\boldsymbol{u}_B' \cdot \frac{\partial \boldsymbol{u}_A'}{\partial t}}$, $\bar{\rho}\overline{\boldsymbol{u}_T' \cdot \frac{\partial \boldsymbol{u}_A'}{\partial t}}$, and $\overline{\frac{p'}{\gamma R}\frac{\partial S'}{\partial t}}$ that is a part of the thermal diffusion term $\overline{\frac{p'}{R}\frac{\partial S'}{\partial t}}$ in equation (2.30). Source terms $\bar{\rho}\overline{\boldsymbol{u}_B' \cdot \frac{\partial \boldsymbol{u}_A'}{\partial t}}$ and $\bar{\rho}\overline{\boldsymbol{u}_T' \cdot \frac{\partial \boldsymbol{u}_A'}{\partial t}}$ also don't present in Doak's energy budget equation (2.30).

2.6 Thermal energy budget equation

Taking the scalar production of equation (2.22) and the fluctuation momentum density $\boldsymbol{m}_T'$

$$\boldsymbol{m}_T' \cdot \frac{\partial \boldsymbol{u}'}{\partial t} + \boldsymbol{m}_T' \cdot \nabla H' = \boldsymbol{m}_T' \cdot \boldsymbol{\alpha}' \tag{2.46}$$

Rewriting equation (2.46) as

$$\frac{\partial}{\partial t}(\boldsymbol{m}_T' \cdot \boldsymbol{u}') - \boldsymbol{u}' \cdot \frac{\partial \boldsymbol{m}_T'}{\partial t} + \nabla \cdot (\boldsymbol{m}_T' H') - (\nabla \cdot \boldsymbol{m}_T')H' = \boldsymbol{m}_A' \cdot \boldsymbol{\alpha}' \tag{2.47}$$

Similarly, we have

$$\boldsymbol{u}' \cdot \frac{\partial \boldsymbol{m}_T'}{\partial t} = \boldsymbol{u}' \cdot \left[\bar{\rho}\frac{\partial \boldsymbol{u}_T'}{\partial t} - \frac{(\gamma-1)\bar{\rho}\bar{\boldsymbol{u}}}{\gamma R}\frac{\partial S'}{\partial t}\right] \tag{2.48}$$

$$(\nabla \cdot \boldsymbol{m}_T')H' = \frac{(\gamma-1)\bar{\rho}}{\gamma R}(h' + \bar{\boldsymbol{u}} \cdot \boldsymbol{u}') \tag{2.49}$$

Hence, equation (2.47) is rewritten as

$$\frac{\partial}{\partial t}(\boldsymbol{m}_T' \cdot \boldsymbol{u}') + \nabla \cdot (\boldsymbol{m}_T' H') = \boldsymbol{m}_T' \cdot \boldsymbol{\alpha}' + \bar{\rho}\boldsymbol{u}_A' \cdot \frac{\partial \boldsymbol{u}_T'}{\partial t} + \bar{\rho}\boldsymbol{u}_B' \cdot \frac{\partial \boldsymbol{u}_T'}{\partial t} + \frac{(\gamma-1)\bar{\rho}h'}{\gamma R}\frac{\partial S'}{\partial t} \tag{2.50}$$

The time-average of equation (2.50) is

$$\nabla \cdot \left(\overline{\boldsymbol{m}_T' H'}\right) = \overline{\boldsymbol{m}_T' \cdot \boldsymbol{\alpha}'} + \bar{\rho}\overline{\boldsymbol{u}_A' \cdot \frac{\partial \boldsymbol{u}_T'}{\partial t}} + \bar{\rho}\overline{\boldsymbol{u}_B' \cdot \frac{\partial \boldsymbol{u}_T'}{\partial t}} + \frac{(\gamma-1)\bar{\rho}}{\gamma R}\overline{h' \frac{\partial S'}{\partial t}} \tag{2.51}$$

The fourth term on the right-hand side of equation (2.51) satisfies

$$\frac{(\gamma-1)\bar{\rho}}{\gamma R}\overline{h' \frac{\partial S'}{\partial t}} = \overline{\frac{(\gamma-1)p'}{\gamma R}\frac{\partial S'}{\partial t}} \tag{2.52}$$

Finally, we obtain

$$\nabla \cdot \left(\overline{\boldsymbol{m}_T' H'}\right) = \overline{\boldsymbol{m}_T' \cdot \boldsymbol{\alpha}'} + \bar{\rho}\overline{\boldsymbol{u}_A' \cdot \frac{\partial \boldsymbol{u}_T'}{\partial t}} + \bar{\rho}\overline{\boldsymbol{u}_B' \cdot \frac{\partial \boldsymbol{u}_T'}{\partial t}} + \overline{\frac{(\gamma-1)p'}{\gamma R}\frac{\partial S'}{\partial t}} \tag{2.53}$$

The thermal energy flux $\overline{\boldsymbol{m}_T' H'}$ is governed by the thermal source $\overline{\boldsymbol{m}_T' \cdot \boldsymbol{\alpha}'}$, $\bar{\rho}\overline{\boldsymbol{u}_A' \cdot \frac{\partial \boldsymbol{u}_T'}{\partial t}}$, $\bar{\rho}\overline{\boldsymbol{u}_B' \cdot \frac{\partial \boldsymbol{u}_T'}{\partial t}}$, and $\overline{\frac{(\gamma-1)p'}{\gamma R}\frac{\partial S'}{\partial t}}$ that is the other part of the thermal diffusion term $\overline{\frac{p'}{R}\frac{\partial S'}{\partial t}}$ in equation (2.30). Source terms $\bar{\rho}\overline{\boldsymbol{u}_A' \cdot \frac{\partial \boldsymbol{u}_T'}{\partial t}}$ and $\bar{\rho}\overline{\boldsymbol{u}_B' \cdot \frac{\partial \boldsymbol{u}_T'}{\partial t}}$ also don't present in Doak's energy budget equation (2.30).

2.7 Energy exchange terms

In three energy budget equations (2.37), (2.45), and (2.53), which govern the energy fluxes carried by each MPT component independently, we find source terms that don't present in Doak's original MPT budget equation. Those new source terms satisfy

$$\bar{\rho}\overline{\boldsymbol{u}_A' \cdot \frac{\partial \boldsymbol{u}_B'}{\partial t}} + \bar{\rho}\overline{\boldsymbol{u}_B' \cdot \frac{\partial \boldsymbol{u}_A'}{\partial t}} = 0, \bar{\rho}\overline{\boldsymbol{u}_A' \cdot \frac{\partial \boldsymbol{u}_T'}{\partial t}} + \bar{\rho}\overline{\boldsymbol{u}_T' \cdot \frac{\partial \boldsymbol{u}_A'}{\partial t}} = 0, \bar{\rho}\overline{\boldsymbol{u}_B' \cdot \frac{\partial \boldsymbol{u}_T'}{\partial t}} + \bar{\rho}\overline{\boldsymbol{u}_T' \cdot \frac{\partial \boldsymbol{u}_B'}{\partial t}} = 0 \tag{2.54}$$

Therefore, we conclude that the physical meaning of the source term $\bar{\rho}\overline{\boldsymbol{u}_a' \cdot \frac{\partial \boldsymbol{u}_b'}{\partial t}}$ is the energy transfer from *a* component to *b* component during the energy transport due to *b* component. This finding clarifies in which manner fluctuation energy exchanges between different components.

2.8 Summary

In this chapter, we first reviewed the MPT decomposition and the derivation of the energy budget equation in Doak's MPT approach. In the MPT decomposition, the fluctuation

momentum density $\boldsymbol{m}' = (\rho \boldsymbol{u})'$ is spilled into the rotational and the irrotational part by the Helmholtz decomposition. The rotational part of $\boldsymbol{m}'$ is defined as the vortical component $\boldsymbol{m}_B'$ of disturbances. Furthermore, the irrotational part of $\boldsymbol{m}'$ is decomposed into the acoustic component $\boldsymbol{m}_A'$ and the thermal component $\boldsymbol{m}_T'$ based on the continuity equation and the thermodynamic state equation. The MPT decomposition provides a unique definition of the vortical, acoustic, and thermal components for a general time stationary flow, while the classic decomposition in Kovásznay's approach is only applicable for the uniform flow. Besides the MPT decomposition, Doak obtained a mean energy budget equation for the fluctuation energy flux $\overline{\boldsymbol{m}'H'}$ based on the continuity equation and the momentum conservation equation. The energy flux $\overline{\boldsymbol{m}'H'}$ and the source term $\overline{\boldsymbol{m}' \cdot \boldsymbol{\alpha}'}$ can be expressed as a linear superposition of energy fluxes and source terms due to each MPT component. Besides the source term caused by the interaction between the acceleration vector $\boldsymbol{\alpha}'$ and each MPT component, there exists another source term $\frac{\overline{p'}}{R}\frac{\overline{\partial s'}}{\partial t}$ which is related to the fluctuation thermal diffusion process. Source terms due to each component and the thermal diffusion source term $\frac{\overline{p'}}{R}\frac{\overline{\partial s'}}{\partial t}$ indicate the energy exchange between disturbances and mean flow during the fluctuation energy transport carried by $\boldsymbol{m}'$.

However, Doak's original budget equation has energy fluxes and source terms in one equation. The effect of source terms on each energy fluxes is confused. The ambiguity in Doak's original budget equation makes it difficult to provide a distinct physical interpretation for the development of disturbances in the flow field. To this end, we proposed three independent energy budget equations for each MPT component by introducing the decomposition of the fluctuation velocity $\boldsymbol{u}'$. In the energy budget equation for the energy flux

carried by each MPT component, energy exchange terms $\overline{\bar{\rho}\boldsymbol{u}_a' \cdot \frac{\partial \boldsymbol{u}_b'}{\partial t}}$ from *a* component to *b* component are discovered for the first time. The effect of source terms on each energy flux is clear in these three independent energy budget equations. The vortical energy flux $\overline{\boldsymbol{m}_B' H'}$ is governed by the vortical source $\overline{\boldsymbol{m}_B' \cdot \boldsymbol{\alpha}'}$ and energy exchange terms, $\overline{\bar{\rho}\boldsymbol{u}_A' \cdot \frac{\partial \boldsymbol{u}_B'}{\partial t}}$ and $\overline{\bar{\rho}\boldsymbol{u}_T' \cdot \frac{\partial \boldsymbol{u}_B'}{\partial t}}$. The acoustic energy flux $\overline{\boldsymbol{m}_A' H'}$ is governed by the acoustic source $\overline{\boldsymbol{m}_A' \cdot \boldsymbol{\alpha}'}$, energy exchange terms $\overline{\bar{\rho}\boldsymbol{u}_B' \cdot \frac{\partial \boldsymbol{u}_A'}{\partial t}}$ and $\overline{\bar{\rho}\boldsymbol{u}_T' \cdot \frac{\partial \boldsymbol{u}_A'}{\partial t}}$, and the thermal diffusion source $\overline{\frac{p'}{\gamma R}\frac{\partial S'}{\partial t}}$. The thermal energy flux $\overline{\boldsymbol{m}_T' H'}$ is governed by the thermal source $\overline{\boldsymbol{m}_T' \cdot \boldsymbol{\alpha}'}$, energy exchange terms $\overline{\bar{\rho}\boldsymbol{u}_A' \cdot \frac{\partial \boldsymbol{u}_T'}{\partial t}}$ and $\overline{\bar{\rho}\boldsymbol{u}_B' \cdot \frac{\partial \boldsymbol{u}_A'}{\partial t}}$, and the thermal diffusion source $\overline{\frac{(\gamma-1)p'}{\gamma R}\frac{\partial S'}{\partial t}}$.

3. MPT analysis of the supersonic mode

3.1 Supersonic mode

In low-disturbance environments, the modal growth of Mack's second mode becomes the primary path to laminar-to-turbulence transition in a two-dimensional (2D) BL over adiabatic surfaces for Mach > 4 [27]. In the case of Mack's second mode over an adiabatic wall, a sonic line is present at y_{s1}, where $\bar{M}(y_{s1}) = \frac{\bar{u}(y_{s1})-c}{\bar{a}(y_{s1})} = -1$. Here, $\bar{u}$ is the mean velocity, c is the disturbance phase speed, and $\bar{a}$ is the local sound speed. The disturbances travel subsonically above the sonic line but supersonically between the wall and the sonic line as trapped sound waves. Outside the BL, the subsonic wave diminishes exponentially.

Bitter and Shepherd [57] studied Mack's second mode over a highly cooled wall. The wall-to-edge temperature ratio was $T_w/T_e < 1$, which corresponds to the state obtained in certain high-enthalpy wind tunnel experiments and real flight cases. They found that a special supersonic mode emerged at the edge of the BL and traveled outside it. Inside the BL over a highly cooled wall, another sonic line appeared, where $\bar{M}(y_{s2}) = \frac{\bar{u}(y_{s2})-c}{\bar{a}(y_{s2})} = 1$ above the first sonic line. The disturbance traveled subsonically between these sonic lines, but supersonically above the upper sonic line (along the edge of the BL) and below the lower sonic line. Notably, LST analysis [29, 58-61] showed that the synchronization of the free-stream slow sound waves and Mack's second mode leads to the supersonic mode. The supersonic mode was oscillatory outside the BL. This supersonic mode broadens the unstable frequency band for disturbance in the flow field. Chuvakhov and Fedorov [29] called this supersonic mode the "spontaneous radiation of sound," which emphasizes the oscillatory disturbance of the

supersonic mode outside the BL. Owing to the lower amplification rate of this supersonic mode compared with that of subsonic Mack's second mode, the supersonic mode is considered to be insignificant in the transition of the high-speed BL. However, Mortensen [62] recently reported that the rate of growth of the supersonic mode exceeds that of Mack's subsonic second mode in a Mach 20 flow over highly blunt cones. As Mack's second mode and supersonic mode both exhibits acoustic-wavelike behavior between the lower sonic line and the solid wall, it is reasonable that UAC, which suppresses Mack's second mode by dissipating the acoustic wave energy, can also stabilize the supersonic mode because of its similar acoustic characteristics.

Note that the above description of the supersonic mode as a "spontaneous radiation of sound" has not been rigorously validated in realistic circumstances. The difficulty pertains to the lack of a universal definition of an "acoustic" or "sound" wave in a high-speed BL that exhibits a strong gradient in the mean flow field. Doak's MPT approach provides an elegant tool for decomposing a time-stationary fluctuation flow field into three components and overcomes the restriction of Kovásznauy's approach in inhomogeneous systems. Unnikrishnan and Gaitonde [63] performed MPT decomposition of instability waves in the Mach 6 flat plate boundary layer at different wall temperatures. They showed that oscillatory waves outside the highly cooled BL were mostly composed of vortical and acoustic fluctuations. The net outward acoustic flux of the supersonic modes increased with higher levels of wall cooling, as did the perturbation in the wall pressure. Their inspirational work revealed that the MPT approach is promised in the analysis of supersonic modes. However, their energy consideration was based on Doak's original energy budget equation and thus

cannot clarify the effect of sources terms on the “sound radiation” of supersonic modes. To this end, MPT decomposition and three independent energy budget equations derived in Chapter 2 are applied to DNS data of supersonic modes with high-level wall cooling effect over smooth solid wall and UAC to provide a physical interpretation of the sound radiation mechanism in the supersonic mode and the stabilization mechanism of porous coatings to the supersonic mode.

3.2 Direct numerical simulation

The 2D Navier–Stokes equations in the conservation form which consist of a mass conservation equation, two momentum conservation equations, and an energy conservation equation is solved numerically. The dimensional governing equation in an arbitrary curvilinear coordinate system (ξ, η) can be written as

$$\frac{\partial \boldsymbol{Q}}{\partial t} + \frac{\partial \boldsymbol{E}}{\partial \xi} + \frac{\partial \boldsymbol{F}}{\partial \eta} = 0 \tag{3.1}$$

Here, $\boldsymbol{Q}$ is a vector of the conservative variables, and $\boldsymbol{E}$ and $\boldsymbol{F}$ is the flux vector in the ξ and η directions, respectively. Mapping the curvilinear coordinate system (ξ, η) into the Cartesian coordinate system (x, y), these vectors can be expressed in terms of the corresponding Cartesian vectors $\boldsymbol{Q}_c$, $\boldsymbol{E}_c$, and $\boldsymbol{F}_c$ as

$$\boldsymbol{Q} = J\boldsymbol{Q}_c, \boldsymbol{E} = J\left(\boldsymbol{E}_c \frac{\partial \xi}{\partial x} + \boldsymbol{F}_c \frac{\partial \xi}{\partial y}\right), \boldsymbol{F} = J\left(\boldsymbol{E}_c \frac{\partial \eta}{\partial x} + \boldsymbol{F}_c \frac{\partial \eta}{\partial y}\right) \tag{3.2}$$

Here, $J = \left|\frac{\partial(x,y)}{\partial(\xi,\eta)}\right|$ is the transformation Jacobian. Vectors in the Cartesian coordinate system are defined as

$$\boldsymbol{Q}_c = \begin{Bmatrix} \rho \\ \rho u \\ \rho v \\ e \end{Bmatrix} \tag{3.3}$$

$$\boldsymbol{E}_c = \begin{Bmatrix} \rho u \\ \rho u^2 + p - \tau_{xx} \\ \rho uv - \tau_{xy} \\ u(e+p) - u\tau_{xx} - v\tau_{xy} + q_x \end{Bmatrix} \tag{3.4}$$

$$\boldsymbol{F}_c = \begin{Bmatrix} \rho v \\ \rho uv - \tau_{xy} \\ \rho v^2 + p - \tau_{yy} \\ v(e+p) - u\tau_{xy} - v\tau_{yy} + q_y \end{Bmatrix} \tag{3.5}$$

Here, ρ is density, u and v denote the components of velocity in Cartesian coordinates, $e = \frac{p}{\gamma-1} + \frac{\rho(u^2+v^2)}{2}$ is the specific total energy, the specific heat ratio $\gamma = 1.4$, and p is pressure. The stress tensor τ and heat flux q are

$$\tau_{xx} = 2\mu\frac{\partial u}{\partial x} - \frac{2}{3}\mu\left(\frac{\partial u}{\partial x} + \frac{\partial v}{\partial y}\right),\ \tau_{xy} = \mu\left(\frac{\partial u}{\partial y} + \frac{\partial v}{\partial x}\right),\ \tau_{yy} = 2\mu\frac{\partial v}{\partial y} - \frac{2}{3}\mu\left(\frac{\partial u}{\partial x} + \frac{\partial v}{\partial y}\right) \tag{3.6}$$

$$q_x = -k\frac{\partial T}{\partial x},\ q_y = -k\frac{\partial T}{\partial y} \tag{3.7}$$

Here, T is the temperature. The perfect gas condition was assumed. The dynamic viscosity coefficient μ and heat conductivity k were calculated by Sutherland's law with Prandtl number $Pr = 0.72$.

A high-order, accurate, shock-fitting finite difference method is adopted in the DNS calculation. The fifth-order upwind compact scheme is utilized to discretize the inviscid flux derivatives and the sixth central difference scheme is used to discretize the viscous terms. The temporal integration is simulated by the third order Runge–Kutta method. Two numerical simulations are performed for Mach 6.0 BL flows on a solid wall and a porous coating with very low wall temperature. In both cases, the unit Reynolds number is 1×10^7 m^{-1}, and Mach number in the freestream M_∞ is 6.0. The freestream temperature and wall temperature are 300 K and 150 K, respectively. The length of the flat plate is $L = 0.6$ m, and the computational domain is extended from $x = 0\ m$ to $x = -0.02\ m$ with the symmetry condition at $y = 0$ in the extended region for numerical robustness. The computational grid has 3607×320 nodes

clustered at the leading edge and the plate surface. As shown in Figure 3-1, the numerical grid is verified by increasing the grid resolution by a factor of $\sqrt{2}$ in each direction (solid wall case), the discrepancy is less than 1%, and that suggests the grid independence for simulating the development of disturbance.

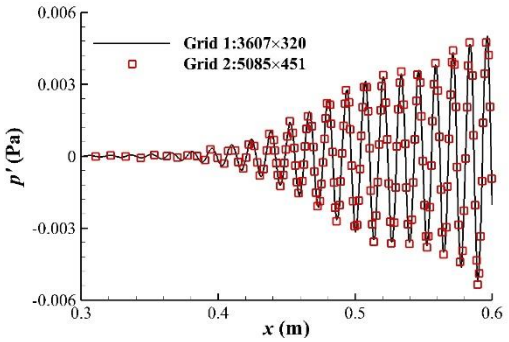

Figure 3-1. Numerical grid verification.

In the case of the porous coating, the coating is placed at $x = 0.3$ m– 0.6 m. The acoustic impedance boundary condition at the wall, $v' = \frac{p'}{Z}$, is adopted to model the porous coating effect. The theoretical model used here to describe the acoustic characteristics of the porous coating is developed by Zhao, et al. [45]. Figure 3-2 shows acoustic waves in the porous coating structure schematically. By considering high-order diffracted modes, the surface impedance *Z* is derived with the follow formulation

$$Z = \rho_w c_w + \frac{\rho_w c_w}{jtan(k_c H)\phi(\rho_w/\tilde{\rho})(k_c/k_0)} - \sum_{-\infty}^{+\infty} \frac{\rho_w c_w k_0}{\sqrt{k_0^2 - \left(\frac{2\pi n}{s}\right)^2}} S_n^2 \tag{3.8}$$

Here, ϕ is the porosity of porous coating, H is the cavity depth, ρ_w is the density at the wall, c_w is the sound speed at the wall, k_0 is the sound wave number at the wall, S_n is the overlap integral between the nth-order diffracted mode and the fundamental mode inside the cavity, $\tilde{\rho}$ is the dynamic density, and k_c is a complex frequency-dependent quantity relating to the thermal and viscous boundary layers inside the narrow cavity. Details of those parameters can be found in Ref.[45]. The structure parameters of porous coating are chosen to be porosity

$\phi = \frac{2b}{s} = 0.76$, depth $H = 1.64 \times 10^{-3}$m, and half-width $b = 1.96 \times 10^{-4}$ m.

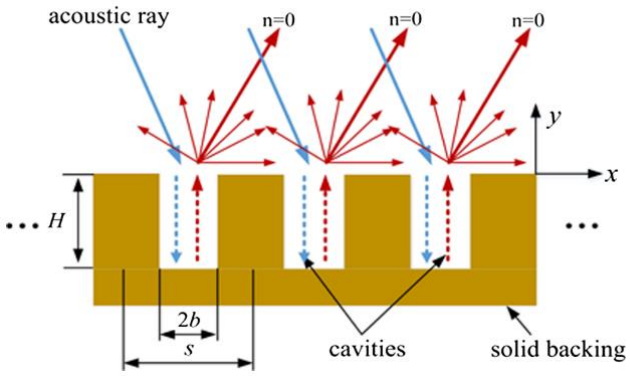

Figure 3-2. Schematic of acoustic waves in the porous coating structure [45].

In the DNS, the steady-state flow field without disturbances is obtained at first. Then, a slot of periodic suction–blowing perturbation is introduced to the steady flow.

$$q_w(x,t) = \varepsilon \sin\left(2\pi \frac{x-x_1}{x_2-x_1}\right) \sin(2\pi f t), \quad x_1 \le x \le x_2 \tag{3.9}$$

Here, q_w is the normal mass flow rate. The suction–blowing region is chosen to be $x_1 =$ 0.03 m, and $x_2 = 0.045$ m. The force amplitude ε =0.001 is adopted to guarantee that the linear assumption is valid. The suction–blowing frequency f is fixed at 495 kHz for both cases, and at this frequency, the supersonic mode is expected to appear at x > 0.34m.

3.3 Linear stability theory results

The spatial LST analysis is performed for the highly cooled wall case with the same flow condition and the same blow-suction frequency as in the DNS calculation. In this highly cooled wall case, Mack's second mode is the F mode instead of the S mode in the adiabatic wall case. The trajectory of the F mode in the $(\frac{c_{ph}}{u_\infty}, \sigma)$ plane are shown in Figure 3-3. Three vertical dashed lines in Figure 3-3 on the left (red), center (blue), and right (green) indicate the location $(1 - 1/M_\infty)$, 1, and $(1 + 1/M_\infty)$, which correspond to slow sound waves,

vorticity/entropy waves, and fast sound waves in the freestream, respectively. Arrows in Figure 3-3 represent the trend in $\frac{c_{ph}}{u_\infty}$ of the F mode as *x* increases. The F mode originates from fast sound waves is stable ($\sigma < 0$). Then, the F mode synchronizes with vorticity/entropy waves and becomes unstable ($\sigma > 0$) after cross vorticity/entropy waves. Finally, the F mode coalesces with slow sound waves and leads to the supersonic mode and a new stable mode.

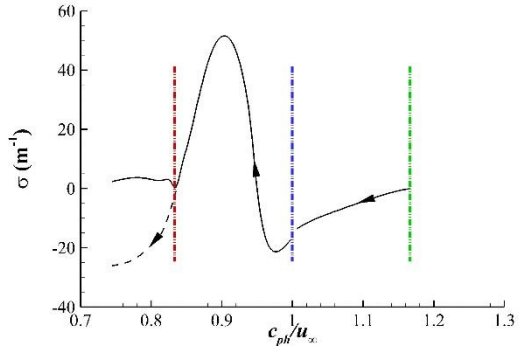

Figure 3-3. The trajectory of the F mode in the ($\frac{c_{ph}}{u_\infty}$, σ) plane. The dashed line shows the new stable mode. Here, u_∞ is the free stream velocity.

3.4 DNS results

An instantaneous snapshot of p', $(\rho u)'$ and $(\rho v)'$ from the results of the DNS of the solid wall and the porous coating are shown in the left column and the right column of Figure 3-4, respectively.

In the solid wall case, the fluctuations induced by the suction/blowing actuator are bifurcated into two regions, one aligning along the shock wave and the other traveling downstream within the boundary layer. An unstable supersonic mode occurs at $x{\sim}0.34m$, and p', $(\rho u)'$, and $(\rho v)'$ are not evanescent above the BL. The so-called region of "spontaneous sound radiation" is enlarged as the perturbations propagated downstream, and it appears as though they were radiating outward at a fixed degree. In general, the peak values of

fluctuations in the streamwise momentum [Figure 3-4 (b1, b2)] are an order of magnitude higher than those of the wall-normal component [Figure 3-4 (c1, c2)].

In contrast to the case of the solid wall, when the disturbances travel downstream through the porous coating ($x = 0.3 - 0.6$ m), there is no visible "spontaneous sound radiation" phenomenon [Figure 3-4 (a2)]. The fluctuations within the BL are significantly suppressed, and this indicates that the porous coatings could effectively suppress the amplification of Mack's second mode and the supersonic mode.

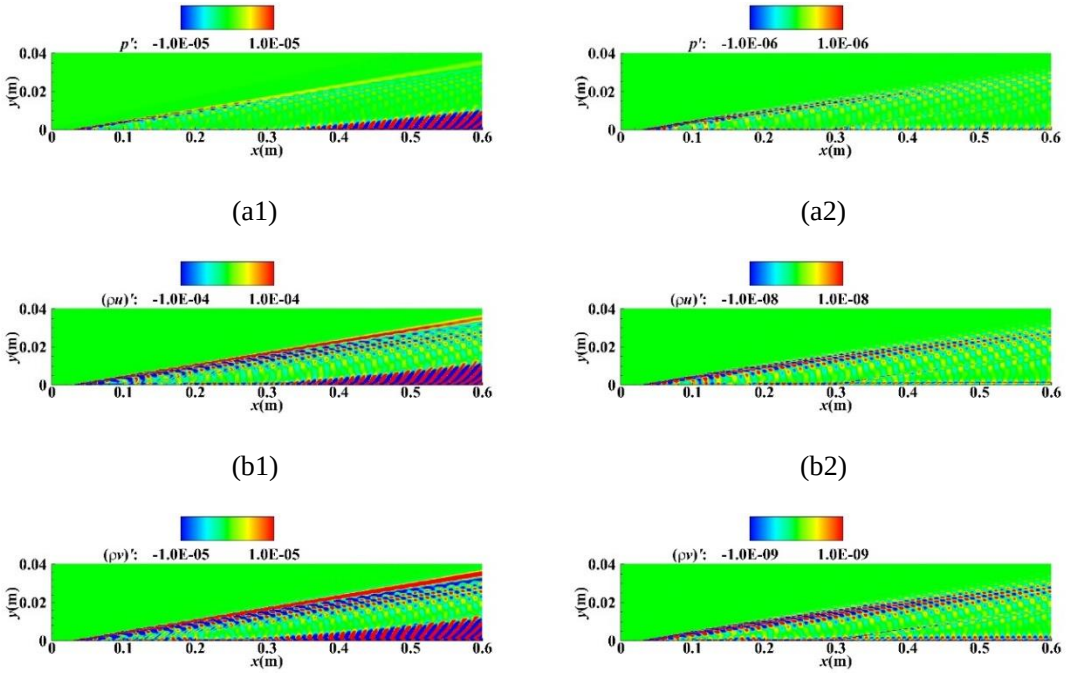

(a1) (a2)

(b1) (b2)

(c1) (c2)

Figure 3-4. Instantaneous snapshots of (a1, a2) p' (Pa), (b1, b2) $(\rho u)'$ (kg/m2/s), and (c1, c2) $(\rho v)'$ (kg/m2/s) in the case of the solid wall (left column) and the porous wall (right column).

3.5 MPT decomposition

The different components are extracted by applying Doak's MPT approach to the

instantaneous fluctuation field. The MPT decomposition is accomplished by solving two Poisson equations in equation (2.11). The Dirichlet boundary condition for momentum potential ($\varphi = 0$) is adopted at the boundaries of the 2D computation region as in Ref. [55]. An instantaneous snapshot of the magnitudes of the vortical component ($\|\boldsymbol{m}_B'\|$), acoustic component ($\|\boldsymbol{m}_A'\|$), and thermal component ($\|\boldsymbol{m}_T'\|$) of the solid wall and the porous wall are depicted in the left column and the right column of Figure 3-5, respectively.

In the solid wall case, the result captures vortical perturbations from small fluctuations induced at the leading shock wave by the blowing–suction actuator of the wall. The vortical and thermal perturbations have the largest and smallest magnitudes, respectively. Both $\boldsymbol{m}_B'$ and $\boldsymbol{m}_A'$ are present in the region of oscillation outside the BL, while the thermal component is not prominent in the "sound radiation." This observation indicates that the "sound radiation" is not sufficiently precise to describe the unstable supersonic mode. Both acoustic and vortical waves exist in the "radiation" region.

Figure 3-6 shows the distribution of $\|\boldsymbol{m}_B'\|$, $\|\boldsymbol{m}_A'\|$, and $\|\boldsymbol{m}_T'\|$ along the *x* axis at *y*=0m in the solid wall case and the porous wall case. On the porous coating, the amplitude of each component is reduced by an order of magnitude at *x*=0.4m [Figure 3-6(a) and Figure 3-6(b)]. The effect of the coating end (x = 0.3m), associated with the juncture between the solid and porous parts, induces vortical and slight acoustic components along the expansion wave. The vortical component continues to be the dominant one in terms of exhibiting the highest amplitude among all FT components [Figure 3-5(a2)]. Moreover, the regions of "sound radiation" in the acoustic and vortical components disappears [Figure 3-5(b2) and Figure 3-5(c2)].

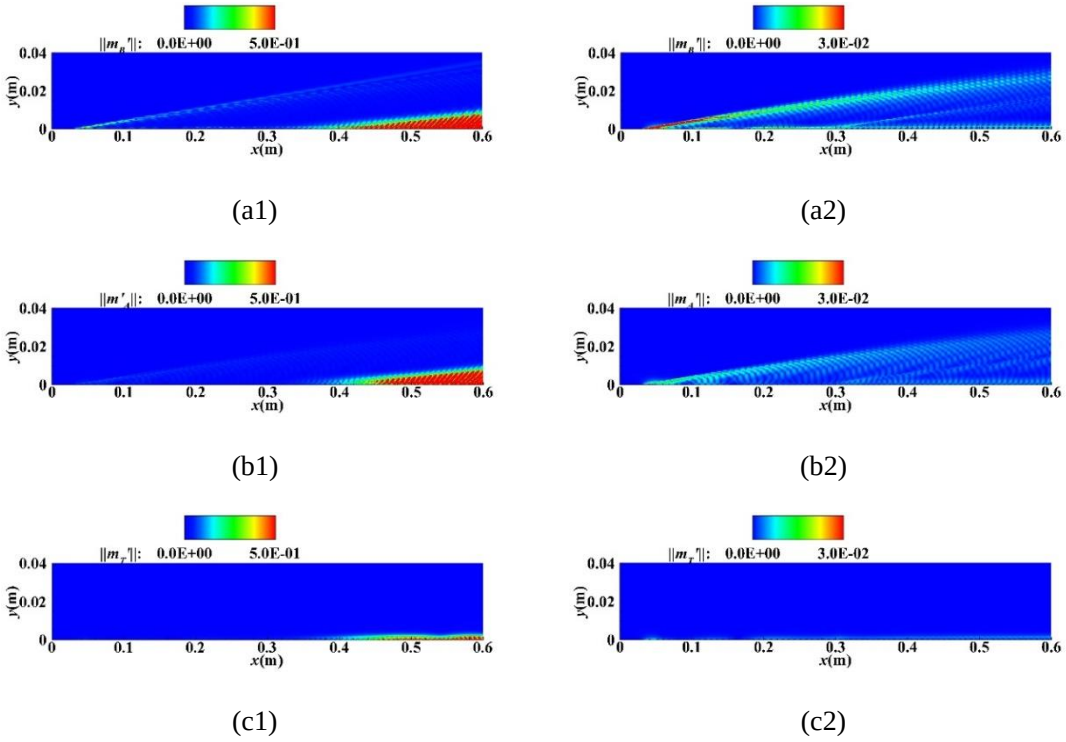

(a1) (a2)

(b1) (b2)

(c1) (c2)

Figure 3-5. Magnitudes of (a1, a2) m'_B, (b1, b2) m'_A, and (c1, c2) m'_T in the case of the solid wall (left column) and the porous wall (right column). (unit: kg/(m2•s).

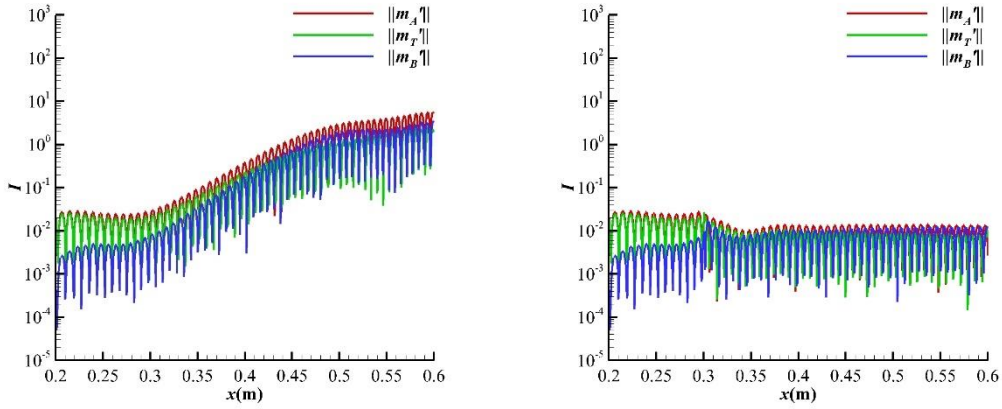

(a) (b)

Figure 3-6. Magnitudes of m'_B, m'_A, and m'_T at y=0m in the case of the solid wall (left column) and the porous wall (right column). (unit: kg/(m2•s).

3.1 Mean energy fluxes

In this section, the mean energy fluxes carried by different components of the MPT is

discussed to provide insights into the development of perturbations in the BL. For convenience of discussion, the x gradient of the streamwise component of the mean energy flux $\frac{\partial}{\partial x}\left(\overline{m'_{Bx}H'}\right)$, $\frac{\partial}{\partial x}\left(\overline{m'_{Ax}H'}\right)$, and $\frac{\partial}{\partial x}\left(\overline{m'_{Tx}H'}\right)$ are denoted by $\boldsymbol{J_{Bx}}$, $\boldsymbol{J_{Ax}}$, and $\boldsymbol{J_{Tx}}$, respectively. Similarly, the y gradient of the normal component of the mean energy flux, $\frac{\partial}{\partial y}\left(\overline{m'_{By}H'}\right)$, $\frac{\partial}{\partial y}\left(\overline{m'_{Ay}H'}\right)$, and $\frac{\partial}{\partial y}\left(\overline{m'_{Ty}H'}\right)$ are denoted by $\boldsymbol{J_{By}}$, $\boldsymbol{J_{Ay}}$, and $\boldsymbol{J_{Ty}}$, respectively. The vortical source $-\overline{\boldsymbol{m}'_B \cdot \boldsymbol{\alpha}'}$, acoustic source $-\overline{\boldsymbol{m}'_A \cdot \boldsymbol{\alpha}'}$, and thermal source $-\overline{\boldsymbol{m}'_T \cdot \boldsymbol{\alpha}'}$ are designated as $\boldsymbol{P_B}$, $\boldsymbol{P_A}$, and $\boldsymbol{P_T}$, respectively. The sources due to thermal diffusion $-\frac{1}{\gamma R}\overline{S'\frac{\partial p'}{\partial t}}$ and $\frac{\gamma-1}{\gamma R}\overline{p'\frac{\partial S'}{\partial t}}$ in equation (2.45) and equation (2.53) are respectively designated as $\boldsymbol{P_{diff1}}$ and $\boldsymbol{P_{diff2}}$. The energy exchange from component a to b, $\overline{\bar{\rho}\boldsymbol{u}'_a \cdot \frac{\partial \boldsymbol{u}'_b}{\partial t}}$, is denoted by $\boldsymbol{Ex_{ab}}$. The sums of each of the right-hand-side source terms in equations (2.37), (2.45), and (2.53) are $\boldsymbol{N_B}$, $\boldsymbol{N_A}$, and $\boldsymbol{N_T}$, respectively. Thus, the energy budgets of equations (2.37), (2.45), and (2.53) can be expressed as

$$\boldsymbol{J_{Bx} + J_{By} = N_B = P_B + Ex_{AB} + Ex_{TB}} \tag{3.10}$$

$$\boldsymbol{J_{Ax} + J_{Ay} = N_A = P_A + P_{diff1} + Ex_{BA} + Ex_{TA}} \tag{3.11}$$

$$\boldsymbol{J_{Tx} + J_{Ty} = N_T = P_T + P_{diff2} + Ex_{BT} + Ex_{AT}} \tag{3.12}$$

$\boldsymbol{J_{Ax}}$, $\boldsymbol{J_{Bx}}$, $\boldsymbol{J_{Tx}}$, $\boldsymbol{J_{Ay}}$, $\boldsymbol{J_{By}}$, and $\boldsymbol{J_{Ty}}$ on the solid wall and the porous coating at x = 0.48 m are illustrated in Figure 3-7. The magnitudes of $\boldsymbol{J_{Ax}}$, $\boldsymbol{J_{Bx}}$, and $\boldsymbol{J_{Tx}}$ are much smaller than those of $\boldsymbol{J_{Ay}}$, $\boldsymbol{J_{By}}$, and $\boldsymbol{J_{Ty}}$ in the BL. This indicates that the source terms on the right-hand side of equations (3.10), (3.11), and (3.12) influences the normal fluctuation energy transport in the first place, possibly because the y gradient of mean flow is much stronger than the x gradient in the BL flow field. In the case of the solid wall, $\boldsymbol{J_{Ay}}$ reaches its positive peak at around y_c = 0.001 m (the critical layer where $\bar{M}(y_c) = \frac{\bar{u}(y_c)-c}{\bar{a}(y_c)} = 0$) and then becomes negative above this

peak. This indicates the acoustic source terms strengthen acoustic fluxes in the *y*-direction around the critical layer and then weaken them in the negative region. $\boldsymbol{J_{By}}$ has a negative peak around the critical layer while $\boldsymbol{J_{Ty}}$ is positive between two sonic lines. In the case of the porous wall, the acoustic flux $\boldsymbol{J_{Ay}}$ behaves similarly to that in the case of the solid wall. $\boldsymbol{J_{By}}$ first reaches a negative peak and then changes to a positive peak above the critical layer, and $\boldsymbol{J_{Ty}}$ shows a contrary trend to $\boldsymbol{J_{By}}$, but with a slightly smaller magnitude. In the detailed analysis of the source terms provided in the next section, the reversals in $\boldsymbol{J_{By}}$ and $\boldsymbol{J_{Ty}}$ are found to be related to the terms of energy exchange.

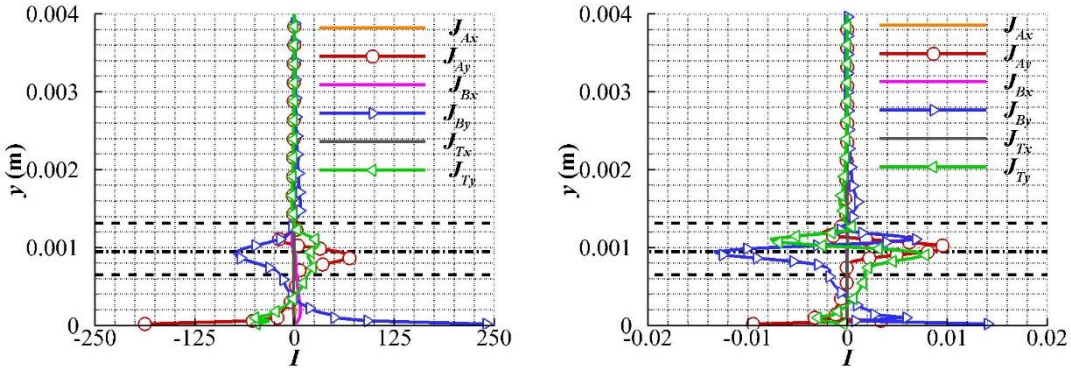

(a) (b)

Figure 3-7. Gradients of mean energy fluxes at x = 0.48m in the cases of the solid wall (a) and the porous coating (b). The sonic line and critical layer are marked using a dashed line and dash-dotted line, respectively (unit: kg/(m•s3).

Figure 3-8 shows the acoustic, vortical, and thermal flux lines in the range of x = 0.45–0.5 m, which indicates the directions of the mean transport of the fluctuation energy according to its respective components in the flow field. The background shows contours of $\boldsymbol{N_A}$, $\boldsymbol{N_B}$, and $\boldsymbol{N_T}$. As shown in Figure 3-8(a1), acoustic fluxes originate around the critical layer owing to the acoustic source terms and diffused. Above this layer, the fluctuation energy is transported

toward the bulk flow by $\boldsymbol{m}_A'$, and leading to the "spontaneous sound radiation." In Figure 3-8 (b1), vortical source terms produce energy for the vortical fluxes in the vicinity of the surface of the plate. Then, vortical fluxes originating from the plate's surface sink near the critical layer. The fluctuation energy is transported from the bulk flow into the BL by $\boldsymbol{m}_B'$. Compared with $\boldsymbol{N_A}$ and $\boldsymbol{N_B}$, the intensity of the thermal source terms is so weak that the thermal component is not prominent in the region of "sound radiation" [Figure 3-8(c1) and Figure 3-5(c1)]. In the case of the porous coating [Figure 3-8(a2)–Figure 3-8(c2)], the sum of the source terms, i.e., $\boldsymbol{N_A}$, $\boldsymbol{N_B}$, and $\boldsymbol{N_T}$, is about four orders of magnitude smaller than that in the case of the solid wall. As shown in Figure 3-8(a2), $\boldsymbol{N_A}$ around the critical layer is so weak that the upward acoustic flux lines finally turn upward. The fluctuation energy is barely transported out of the BL by $\boldsymbol{m}_A'$. As a result, the "spontaneous radiation phenomenon" is absent in the case of the porous coating.

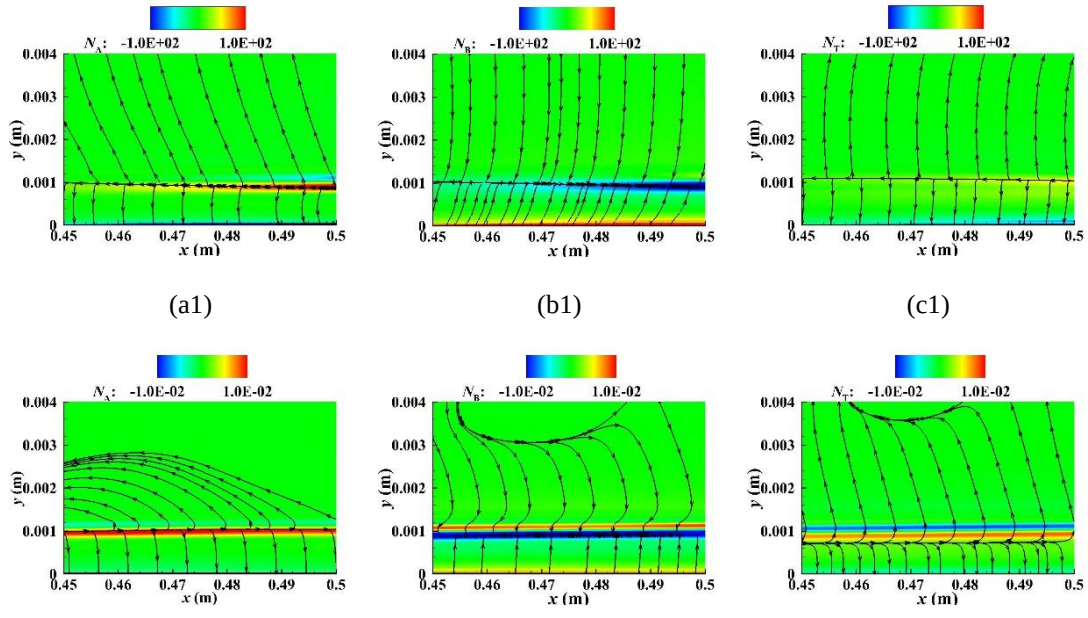

(a1) (b1) (c1)

(a2) (b2) (c2)

Figure 3-8. (a1, a2) acoustic, (b1, b2) vortical, and (c1, c2) thermal fluxes in the cases of the solid wall (upper row) and the porous coating (lower row; unit: kg/(m•s3).

3.2 Source mechanism

Figure 3-9 shows the contour of the acoustic source terms and Figure 3-10 shows the distribution of the acoustic source terms along the y axis at x=0.48m. The left column represents the case of the solid wall and the right column that of the porous coating. In the former case, $\boldsymbol{P_A}$ is a primary energy producer near the critical layer and extracts fluctuation energy from the mean flow. Then, $\boldsymbol{P_A}$ dissipates this fluctuation energy during the upward transport of the fluctuation energy due to $\boldsymbol{m'_A}$ [Figure 3-9(a1)]. $\boldsymbol{P_{diff1}}$ always dissipates the fluctuation energy near the critical layer [Figure 3-9(b1)]. The fluctuation energy is transferred from the vortical part to the acoustic part near the critical layer [Figure 3-9(c1)], while acoustic fluctuation energy is transferred into thermal energy [Figure 3-9(d1)]. The amplitude of $\boldsymbol{Ex_{BA}}$ is larger than that of $\boldsymbol{Ex_{TA}}$. Therefore, $\boldsymbol{Ex_{BA}}$ compensates for the energy loss due to $\boldsymbol{Ex_{TA}}$ and became the other primary energy producer besides $\boldsymbol{P_A}$ near the critical layer. In this regard, the outward acoustic fluxes and "sound radiation" phenomenon are directly related to $\boldsymbol{P_A}$ and $\boldsymbol{Ex_{BA}}$. In the case of the porous wall, the energy exchange terms $\boldsymbol{Ex_{BA}}$ and $\boldsymbol{Ex_{TA}}$ have nearly the same magnitude [Figure 3-9(c2) and Figure 3-9(d2)]. Due to the balance between $\boldsymbol{Ex_{BA}}$ and $\boldsymbol{Ex_{TA}}$, $\boldsymbol{P_A}$ is the unique primary energy producer in this case [Figure 3-9(a2)]. However, $\boldsymbol{P_A}$ is significantly suppressed compared with that in the case of the solid wall, and this weakens the outward transport of the fluctuation energy by $\boldsymbol{m'_A}$.

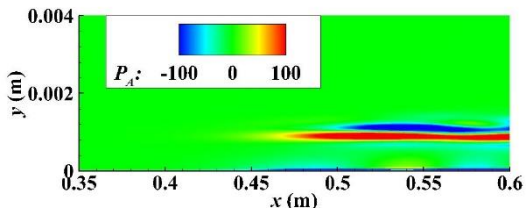

(a1)

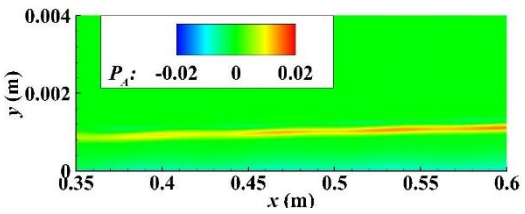

(a2)

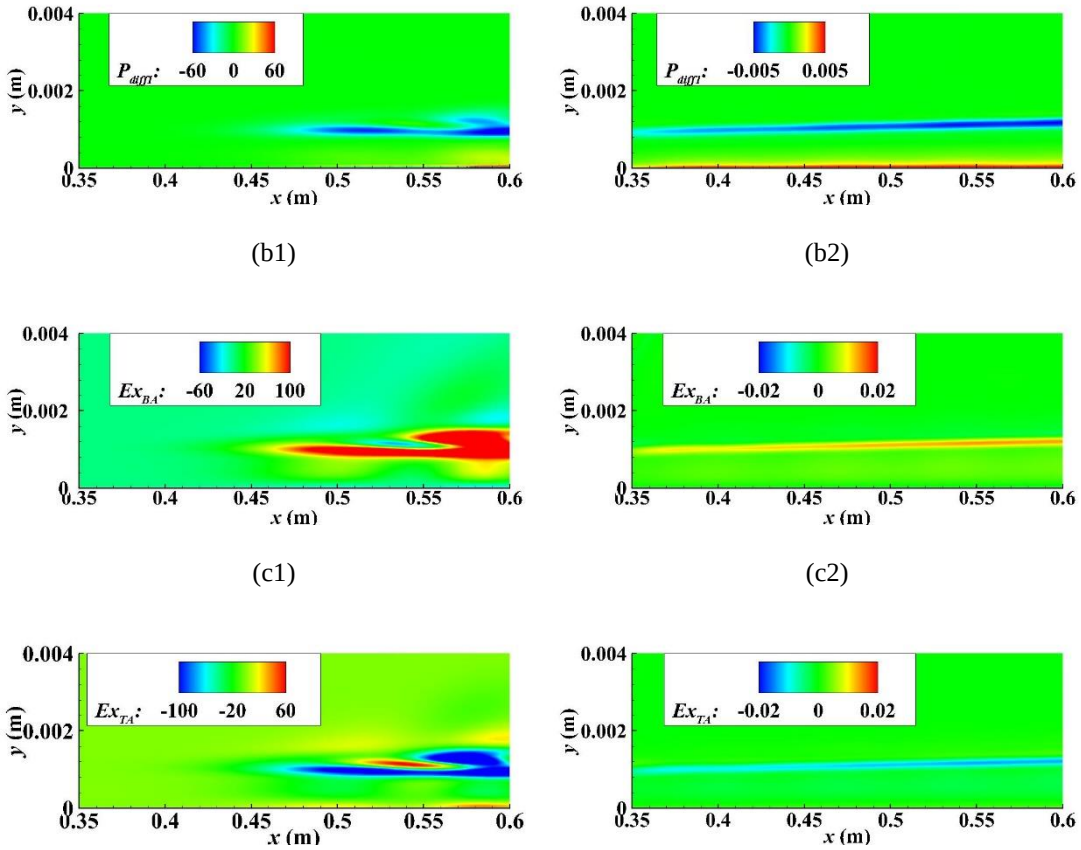

(b1) (b2)

(c1) (c2)

(d1) (d2)

Figure 3-9. Left column: acoustic source terms for the solid wall; right column: acoustic source terms for the porous coating (unit: kg/(m•s^3).

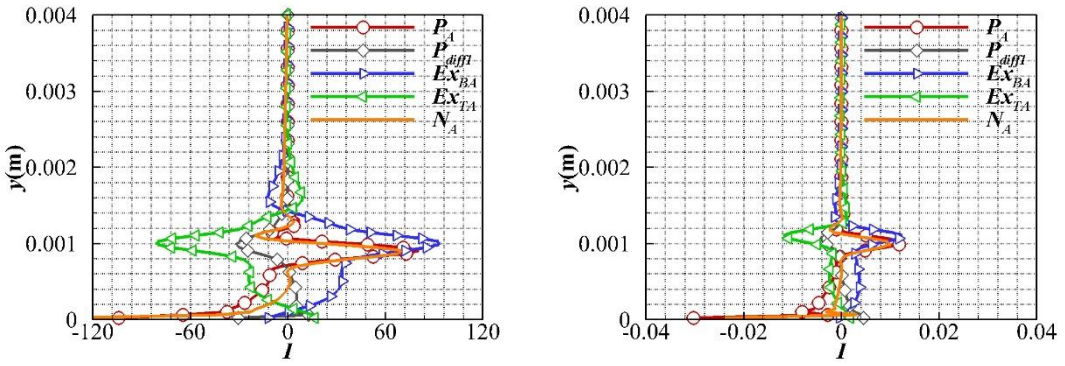

(a) (b)

Figure 3-10. Acoustic source terms at x = 0.48m in the cases of the solid wall (a) and the porous coating (b) (unit: kg/(m•s3).

Figure 3-11 shows the contour of vortical source terms and Figure 3-12 shows the

distribution of the vortical source terms along the y axis at x=0.48m. In the case of the solid wall, $\boldsymbol{P_B}$ is the energy producer in the vicinity of the surface of the plate [Figure 3-11(a1)]. Near the critical layer, vortical energy is transformed into acoustic energy [Figure 3-11(b1)], which leads to a significant sink in the vortical fluxes [Figure 3-8(b1)]. In the case of the porous wall, $\boldsymbol{P_B}$ is suppressed at the plate's surface and thus less vortical energy is transported to the critical layer. Furthermore, $\boldsymbol{Ex_{TB}}$ has a larger amplitude than $\boldsymbol{Ex_{AB}}$, which is in contrast to the case of the solid wall, and leads to reversals in $\boldsymbol{J_{By}}$ and $\boldsymbol{J_{Ty}}$ [Figure 3-7(b)].

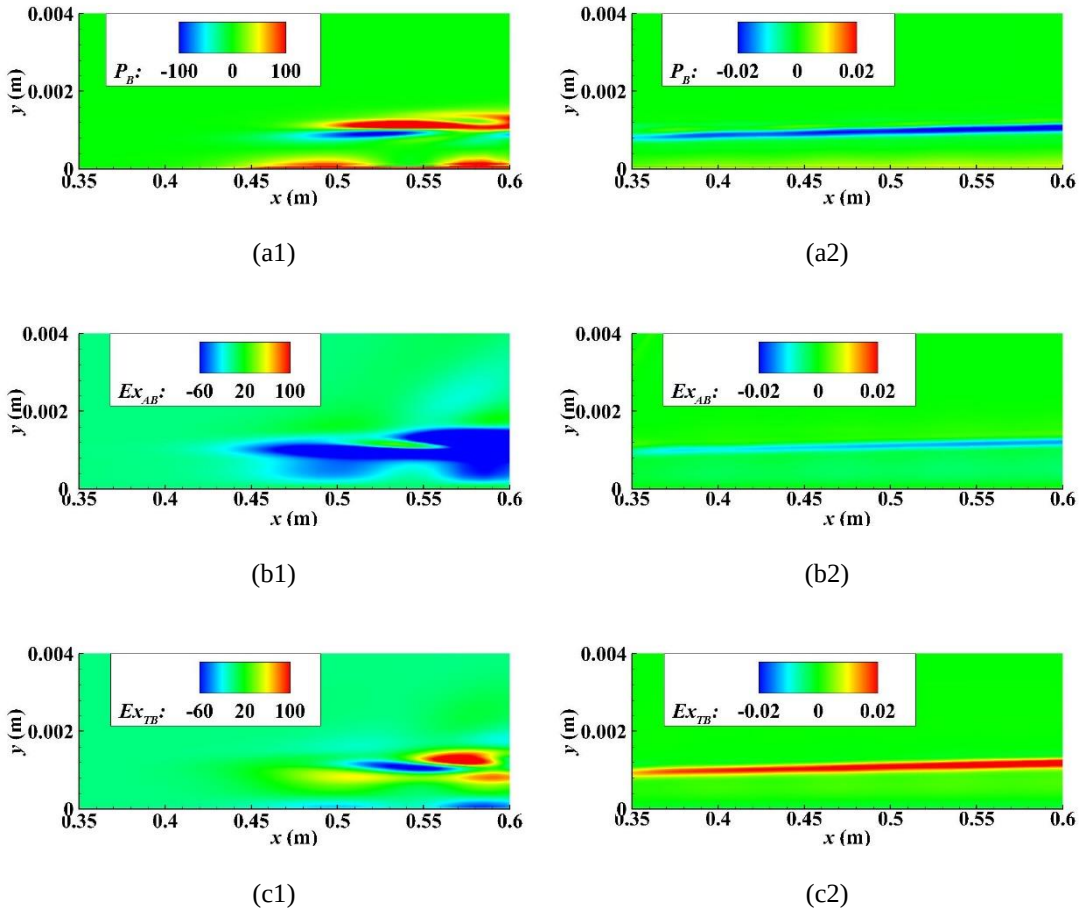

(a1) (a2)

(b1) (b2)

(c1) (c2)

Figure 3-11. Left column: vortical source terms for the solid wall; right column: vortical source terms for the porous coating (unit: kg/(m•s^3).

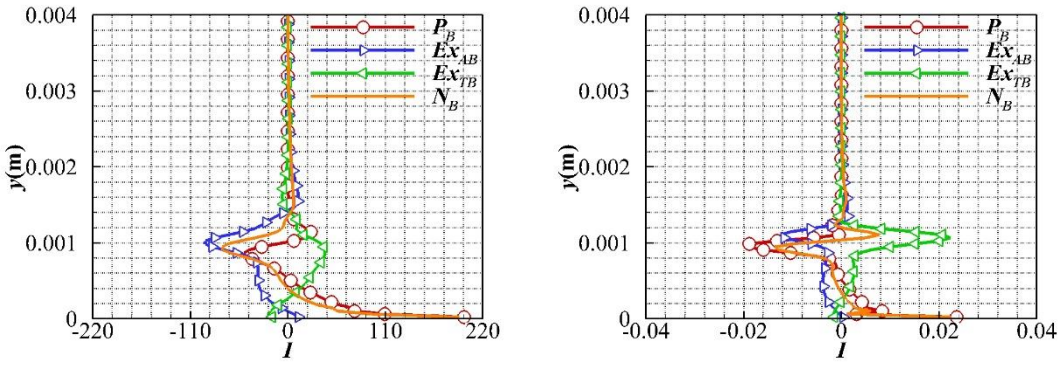

(a) (b)

Figure 3-12. Vortical source terms at x = 0.48m in the cases of the solid wall (a) and the porous coating (b) (unit: kg/(m•s^3).

Figure 3-13 shows the contour of the thermal source terms and Figure 3-14 shows the distribution of the thermal source terms along the y axis at x=0.48m. In the case of the solid wall, $\boldsymbol{Ex_{AT}}$ is the primary energy producer of thermal fluxes, which is transformed from acoustic energy near the critical layer [Figure 3-13(c1)]. Nearly all of the energy produced by $\boldsymbol{Ex_{AT}}$ and $\boldsymbol{P_T}$ is consumed by the negative $\boldsymbol{Ex_{BT}}$ and $\boldsymbol{P_{diff2}}$, leading to a marginal value of $\boldsymbol{N_T}$ [Figure 3-8(c1)]. Therefore, the thermal component is not prominent in the region of "sound radiation." In the case of the porous wall, $\boldsymbol{P_T}$ is the primary energy producer, and is approximately balanced by the negative $\boldsymbol{Ex_{BT}}$ [Figure 3-13(d2)]. The magnitudes of the source terms on the porous coating are much smaller than those over the solid wall.

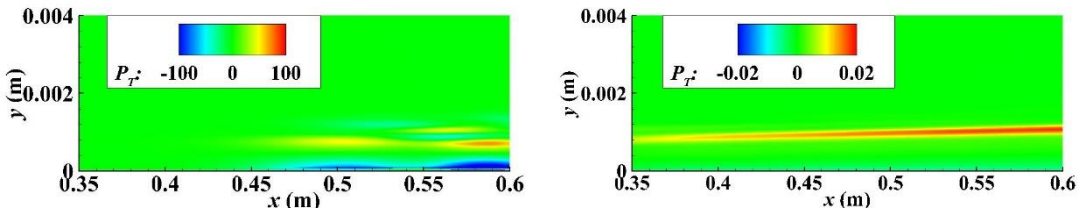

(a1) (a2)

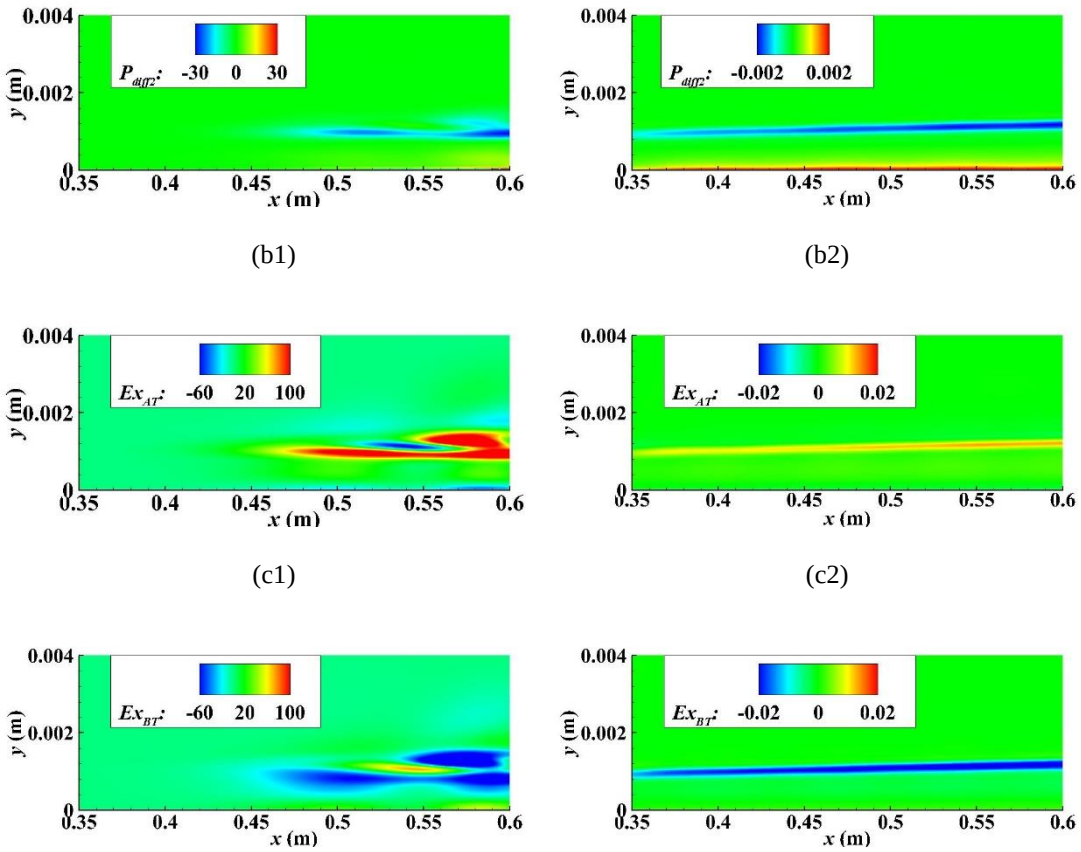

(b1) (b2)

(c1) (c2)

(d1) (d2)

Figure 3-13. Left column: vortical source terms for the solid wall; right column: vortical source terms for the porous coating (unit: kg/(m•s^3).

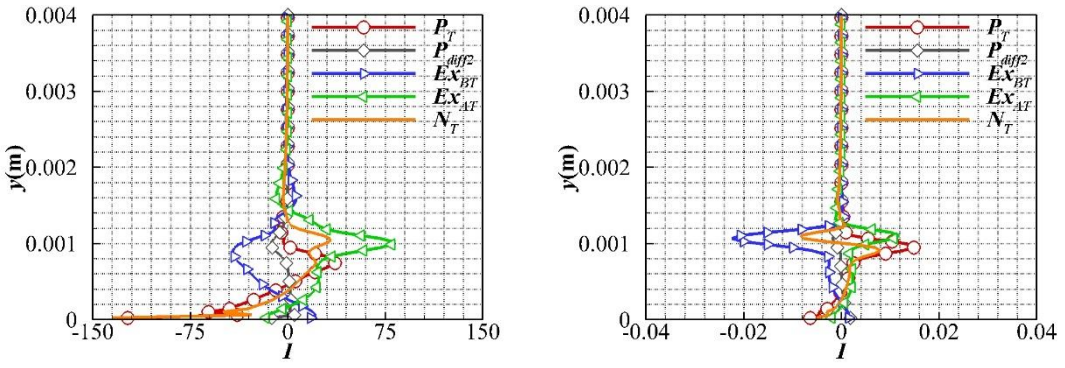

(a) (b)

Figure 3-14. Thermal source terms at x = 0.48m in the cases of the solid wall (a) and the porous coating (b) (unit: kg/(m•s^3).

3.3 Summary

In this chapter, the vortical, acoustic, and thermal components are extracted from the results of DNS for hypersonic BLs on a solid wall and a porous coating by using Doak's MPT decomposition. Three independent energy budget equations for each component are adopted to clarify the contributions of the source terms to each energy flux term. The result shows that the normal transport of the fluctuation energy by the acoustic component is responsible for the mechanisms of "sound radiation" in the supersonic mode. In the case of the solid wall, the vortical and acoustic components coexist in the region of radiation of the supersonic mode. $\boldsymbol{P_A}$ and $\boldsymbol{Ex_{BA}}$ near the critical layer produce energy for acoustic fluxes to transport the fluctuation energy to the bulk flow, which is responsible for the "sound radiation." $\boldsymbol{P_B}$ produced energy for vortical fluxes in the vicinity of the plate surface. However, vortical fluxes sink near the critical layer and fluctuation energy is transformed from the vortical component to the acoustic component. $\boldsymbol{Ex_{AT}}$ and $\boldsymbol{P_T}$ produce energy for thermal fluxes near the critical layer and then fluctuation energy is consumed by $\boldsymbol{Ex_{BT}}$ and $\boldsymbol{P_{diff2}}$. In the case of the porous coating, $\boldsymbol{P_B}$ in the vicinity of the plate's surface is suppressed, and less vortical energy is transported to the critical layer. Therefore, less vortical energy is transformed into acoustic energy and $\boldsymbol{P_A}$ becomes the unique energy producer for acoustic fluxes. The energy produced by $\boldsymbol{P_A}$ cannot compensate for energy loss during the outward transport of the fluctuation energy. Eventually, there is no "spontaneous radiation phenomenon" on the porous coating.

4. MPT analysis of modal growth rate

4.1 Motivation

In chapter 2, we derived three independent energy budget equations for each MPT component for the first time. With these independent energy budget equations, the mean energy flux carried by each component balances with different source terms and energy exchange terms. Source terms indicate the energy exchange between disturbances and the mean flow field, while energy exchange terms represent the energy exchange between different MPT components of disturbances. The sum of three independent energy budget equations gives Doak's original budget equation in which no energy exchange terms are present and the effect of different source terms on different energy flux is ambiguous. Source terms in the MPT energy budget equation can be classified into two categories: 1) the source term due to the interaction between each MPT component and the acceleration vector; 2) the source term arising in the thermal diffusion process.

In chapter 3, we applied three independent energy budget equations to the analysis of the supersonic over highly cooled wall successfully. The acoustic energy flux is confirmed to be responsible for the sound radiation. By comparing the supersonic mode in the solid wall case and the porous wall case, the stabilization mechanism of the porous coating for the supersonic mode is clarified. The diminishing of the vortical source near the flat plate surface leads to the reduction of fluctuation energy transferred from the vortical component to the acoustic component near the critical layer. Thus, the acoustic energy produced near the critical layer is not sufficient to support the outward acoustic energy flux. Consequently, the sound radiation

disappears in the porous wall case.

Considering energy fluxes and source terms, the MPT approach provides a convincing physical interpretation of the sound radiation mechanism of the supersonic mode. Another important issue is the study of the high-speed boundary layer instability is the physical mechanism of the modal growth of Mack's second mode. Numerous existed LST analyses indicated that the synchronization of the S mode and the F mode causes unstable Mack's second mode. The LST results are intriguing. However, the origin of the fluctuation energy that drives the modal growth of Mack's second mode is still mysterious. Therefore, the MPT approach is applied to the LST result of Mack's second mode for the physical explanation of the modal growth of Mack's second mode. The energy analysis in the framework of the MPT approach provides a supplementary to the eigen analysis in the LST.

4.2 Growth rate in the MPT approach

In the study of the supersonic mode, sound radiation is related to the acoustic energy flux. Thus, energy budget equations in the MPT approach are applied directly in the analysis of the sound radiation mechanism of the supersonic mode. Similarly, the key to analyzing the growth rate with the MPT approach is to find the link between the growth rate and the energy budget equation.

As mentioned in Chapter 1, the normal mode in the LST is assumed to have the harmonic wave form $\tilde{\phi}(x,y,z,t) = \hat{\phi}(y)e^{i(\alpha x+\beta z-\omega t)}$. For the spatial LST, the streamwise wave number $\alpha = \alpha_r + i\alpha_i$ is a complex number, and the growth rate $\sigma = -\alpha_i$. The real variables $\phi' = \tilde{\phi} + \tilde{\phi}^*$, the superscript * represents the complex conjugate of a complex variable. The

time average of the product of two disturbances term in the MPT approach is defined as

$$\overline{a'b'} = \frac{\omega}{2\pi}\int_0^{\frac{2\pi}{\omega}} a'b'dt \tag{4.1}$$

where

$$a' = \left[\hat{a}e^{i(\alpha_r x+\beta z-\omega t)} + \hat{a}^* e^{-i(\alpha_r x+\beta z-\omega t)}\right]e^{\sigma x} \tag{4.2}$$

$$b' = \left[\hat{b}e^{i(\alpha_r x+\beta z-\omega t)} + \hat{b}^* e^{-i(\alpha_r x+\beta z-\omega t)}\right]e^{\sigma x} \tag{4.3}$$

Inserting equations (4.2) and (4.3) into equation (4.1), we have

$$\overline{a'b'} = \left(\hat{a}\hat{b}^* + \hat{a}^*\hat{b}\right)e^{2\sigma x} \tag{4.4}$$

Therefore, the *x* derivative of the time-average term $\overline{a'b'}$ in the spatial LST is

$$\frac{\partial\overline{a'b'}}{\partial x} = 2\sigma\left(\hat{a}\hat{b}^* + \hat{a}^*\hat{b}\right)e^{2\sigma x} = 2\sigma\overline{a'b'} \tag{4.5}$$

With equation (4.5), the energy budget equation (2.29) can be rewritten as

$$2\sigma\overline{(\rho u)'H'} + \frac{\partial\overline{(\rho v)'H'}}{\partial y} = \boldsymbol{P_B} + \boldsymbol{P_A} + \boldsymbol{P_T} + \boldsymbol{P_{diff}} \tag{4.6}$$

By now, we have the growth rate σ present in the energy budget equation explicitly. However, there are two terms, $2\sigma\overline{(\rho u)'H'}$ and $\frac{\partial\overline{(\rho v)'H'}}{\partial y}$, on the left-hand side in the equation (4.6). Typically, $\frac{\partial\overline{(\rho v)'H'}}{\partial y}$ has a much larger order of magnitude than $2\sigma\overline{(\rho u)'H'}$ does, as shown in Figure 3-7. Thus, equation (4.6) is not suitable to explain in which manner source terms $\boldsymbol{P_B}$, $\boldsymbol{P_A}$, $\boldsymbol{P_T}$, and $\boldsymbol{P_{diff}}$ affect the growth rate of normal modes in the spatial LST. Another problem is that the equation (4.6) describes the local mean energy balance in the flow field, while the growth rate σ is a global parameter for normal modes of the spatial LST with parallel flow assumption. The growth rate σ in the spatial LST is the same for different physical quantities at different *y* locations. No doubt that the local energy budget equation (4.6) cannot provide a complete description of the contribution of local source terms to the global parameter σ.

Note that the additional term $\frac{\partial\overline{(\rho v)'H'}}{\partial y}$, which cannot be ignored in the local energy budget

equation (4.6), is a *y*-derivative term and the boundary condition for $(\rho v)'$ of the discrete mode in the spatial LST are

$$(\rho v)' = 0, y = 0 \; and \; y \longrightarrow +\infty \tag{4.7}$$

The integration of $\frac{\partial \overline{(\rho v)' H'}}{\partial y}$ from $y = 0$ to $y \longrightarrow +\infty$ is

$$\int_0^{+\infty} \frac{\partial \overline{(\rho v)' H'}}{\partial y} dy = \overline{(\rho v)' H'}\Big|_0^{+\infty} = 0 \tag{4.8}$$

Therefore, the integration of equation (4.6) from $y = 0$ to $y \longrightarrow +\infty$ gives

$$2\sigma \int_0^{+\infty} \overline{(\rho u)' H'} dy = \int_0^{+\infty} \boldsymbol{P_B} dy + \int_0^{+\infty} \boldsymbol{P_A} dy + \int_0^{+\infty} \boldsymbol{P_T} dy + \int_0^{+\infty} \boldsymbol{P_{diff}} dy \tag{4.9}$$

Here, the growth rate σ is independent of the *y* coordinate. The *y*-derivative term $\frac{\partial \overline{(\rho v)' H'}}{\partial y}$ is eliminated in the global integration energy budget equation.

Furthermore, equation (4.9) can be rewritten as

$$\sigma = \frac{\int_0^{+\infty} \boldsymbol{P_B} dy + \int_0^{+\infty} \boldsymbol{P_A} dy + \int_0^{+\infty} \boldsymbol{P_T} dy + \int_0^{+\infty} \boldsymbol{P_{diff}} dy}{2 \int_0^{+\infty} q_x dy} = \sigma_B + \sigma_A + \sigma_T + \sigma_{diff} \tag{4.10}$$

Here, $\overline{(\rho u)' H'}$ is denoted as q_x. The boundary layer is viewed as a waveguide for instability waves, the integration term $\int_0^{+\infty} q_x dy$ is thus the flux of instability waves in the waveguide. Contribution terms of each source term to the growth rate σ is defined as

$$\sigma_B = \frac{\int_0^{+\infty} \boldsymbol{P_B} dy}{2 \int_0^{+\infty} q_x dy}, \sigma_A = \frac{\int_0^{+\infty} \boldsymbol{P_A} dy}{2 \int_0^{+\infty} q_x dy}, \sigma_T = \frac{\int_0^{+\infty} \boldsymbol{P_T} dy}{2 \int_0^{+\infty} q_x dy}, \sigma_{diff} = \frac{\int_0^{+\infty} \boldsymbol{P_{diff}} dy}{2 \int_0^{+\infty} q_x dy} \tag{4.11}$$

4.3 Spatial linear stability analysis

The self-similar solution of the laminar compressible boundary layer on a flat plate is obtained as the basic state for the spatial linear stability analysis

$$(Cf'')' + ff'' = 0 \tag{4.12}$$

$$\left(\frac{C}{Pr} g'\right)' + fg' + \frac{u_e^2}{H_e}\left[C\left(1 - \frac{1}{Pr}\right) f' f''\right]' = 0 \tag{4.13}$$

$$C = \frac{\rho \mu}{\rho_e \mu_e}, \frac{u_e^2}{H_e} = \frac{(\gamma - 1) M^2}{1 + \frac{1}{2}(\gamma - 1) M^2}, \frac{\rho_e}{\mu_e} = \left[1 + \frac{1}{2}(\gamma - 1) M^2\right] g - \frac{1}{2}(\gamma - 1) M^2 f'^2 \tag{4.14}$$

Here, $f'(\eta) = \frac{u}{u_e}$, $g(\eta) = \frac{H}{H_e}$. H is the total enthalpy, ρ is the density, μ is the viscosity coefficient, Pr is the Prandtl number, γ is the specific heat ratio, and M is the Mach number. The prime denotes the differentiation with respect to η and the subscript e denotes the parameters in the freestream. The self-similar independent variables are given by the Howarth– Dorodnitsyn transformations and Mangler transformation by the coordinates

$$\xi = \int_0^x \rho_e \mu_e \bar{u}_e dx \, , \eta = \frac{\bar{u}_e}{\sqrt{2\xi}} \int_0^y \rho dy \tag{4.15}$$

Here, x is the streamwise direction and y is the normal direction to the wall. The conventional no-slip boundary conditions are adopted at the wall.

$$\eta = 0: f = f' = 0, g = g_w \; for \; isothermal \; wall \; or \; g' = 0 \; for \; adiabatic \; wall \tag{4.16}$$

$$\eta \longrightarrow \infty: f' = 1, g = 1 \tag{4.17}$$

In the spatial linear stability analysis hereinafter, the gas is assumed to be calorically and thermally perfect with $Pr = 0.72$ and $\gamma = 1.4$. The viscosity μ is approximated by Sutherland's law.

$$\frac{\mu}{\mu_{ref}} = \frac{T_{ref}+S}{T+S}\left(\frac{T}{T_{ref}}\right)^{\frac{3}{2}} \tag{4.18}$$

Here, $S = 110.4K$, $T_{ref} = 273.15K$, and $\mu_{ref} = 1.716 \times 10^{-5} Pa \cdot s$. The free-stream parameter is $M = 6.0$, $T_e = 43.18K$, and the unit Reynolds number is $Re_u = 1.05 \times 10^7 m^{-1}$. In this case, the adiabatic wall temperature is $T_w = 300K$. The frequency is fixed at 138.74kHz.

In the spatial LST with parallel flow assumption, the small disturbance is harmonic in time, $\phi'(x, y, z, t) = \hat{\phi}(y) e^{i(\alpha x + \beta z - \omega t)}$. ω and β are real numbers, while α is a complex number. Since Mack's second mode is two-dimensional, β is fixed to be 0 in the spatial LST in this study. The linearized Navier-Stokes equations for disturbances is written in the matrix

form, as in Ref. [64]

$$\frac{\partial}{\partial y}\left(\boldsymbol{L}_0\frac{\partial \phi'}{\partial y}\right)+\boldsymbol{L}_1\frac{\partial \phi'}{\partial y}=\boldsymbol{H}_1\phi'+\boldsymbol{H}_2\frac{\partial \phi'}{\partial x} \tag{4.19}$$

Here, $\boldsymbol{L}_0$, $\boldsymbol{L}_1$, $\boldsymbol{H}_1$, and $\boldsymbol{H}_2$ are 9×9 matrices. ϕ' has 9 components:

$$\phi'=\left(u',\frac{\partial u'}{\partial y},v',p',T',\frac{\partial T'}{\partial y},\frac{\partial u'}{\partial x},\frac{\partial v'}{\partial x},\frac{\partial T'}{\partial x}\right) \tag{4.20}$$

In which u, v, p, and T are the streamwise velocity, normal velocity, pressure, and temperature, respectively.

With the harmonic wave form of small disturbances, we have

$$\frac{\partial}{\partial y}\left(\boldsymbol{L}_0\frac{\partial \hat{\phi}}{\partial y}\right)+\boldsymbol{L}_1\frac{\partial \hat{\phi}}{\partial y}=\boldsymbol{H}_1\hat{\phi}+i\alpha\boldsymbol{H}_2\hat{\phi} \tag{4.21}$$

Here,

$$\hat{\phi}=\left(\hat{u},\frac{\partial \hat{u}}{\partial y},\hat{v},\hat{p},\hat{T},\frac{\partial \hat{T}}{\partial y},\frac{\partial \hat{u}}{\partial x},\frac{\partial \hat{v}}{\partial x},\frac{\partial \hat{T}}{\partial x}\right) \tag{4.22}$$

The boundary condition for the discrete modes of the spatial LST is

$$y=0:\hat{u}=\hat{v}=\hat{T}=0 \tag{4.23}$$

$$y\to\infty:\hat{u},\hat{v},\hat{T}\longrightarrow 0 \tag{4.24}$$

Finally, the governing equations (4.21) are discretized along with boundary conditions (4.23) and (4.24), a matrix eigenvalue problem is formulated as

$$A\hat{\phi}=i\alpha B\hat{\phi} \tag{4.25}$$

By solving the general eigenvalue problem (4.25), the dispersion relation $\alpha=\alpha(\omega)$ and the eigenfunction $\hat{\phi}$ of discrete normal modes of the spatial LST are obtained.

4.4 Spatial LST results of the Mach 6.0 adiabatic wall case

Figure 4-1 shows the phase speed $C_r=\frac{\omega}{\alpha_r}$ and imaginary part of wave number α_i of the

S mode and F mode in the Mach 6.0 boundary layer over the adiabatic wall. The growth rate $\sigma = -\alpha_i$ in the spatial LST. In Figure 4-1(a), three horizontal dashed lines indicate the phase speed of fast acoustic waves (upper, $C_{ph} = 1 + \frac{1}{M}$), vorticity/entropy waves (middle, $C_{ph} = 1$), and slow acoustic waves (lower, $C_{ph} = 1 - \frac{1}{M}$) in the freestream. Two vertical dotted line in Figure 4-1(a) indicate the location of SP1 (the synchronization point of the S mode and vorticity/entropy waves, $x \sim 0.76m$) and SP2 (the synchronization point of the S mode and F mode, $x \sim 0.1m$). In Figure 4-1(b), the S mode becomes most unstable at $x \sim 0.11m$, which is at the downstream of the synchronization point. The synchronization point of the S mode and F mode causes Mack's second mode.

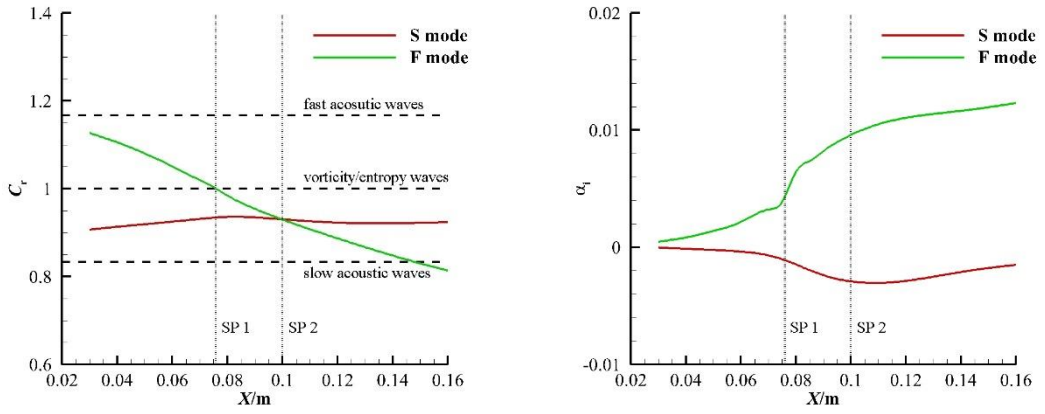

(a) (b)

Figure 4-1. The (a) phase speed $C_r = \frac{\alpha_r}{\omega}$ and (b) imaginary part of wave number α_i of the S mode and the F mode in the spatial linear analysis for the Mach 6.0 boundary layer over the adiabatic wall. C_r and α_i are dimensionless. The characteristic velocity is the freestream velocity u_e and the characteristic length is the local boundary layer thickness $L_{ref} = \sqrt{\frac{x}{Re_u}}$.

Figure 4-2 shows the eigenfunction of the S mode at the synchronization point $x = 0.1m$. The eigenfunction is normalized by p' at $y = 0$. Both p' and T' shows a peak at the critical layer, where $\bar{u} = C_r$. In a thin layer near the wall, u', v', and T' decreases to 0 due to viscosity

effect to satisfy their boundary condition at the wall.

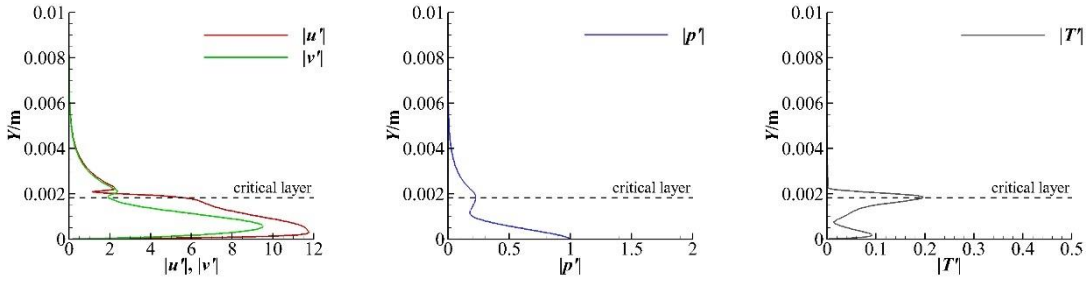

(a) (b) (c)

Figure 4-2. The eigenfunction of unstable Mack's second mode (the S mode) at the synchronization point *x*=0.1m: (a) absolute values of u', v'; (b) the abosolute value of p'; (c) the abosolute value of T'. The horinzontal dashed line indicate the location of the critical layer, where $\bar{u} = C_r$.

4.5 MPT decomposition of Mack's second mode

With the harmonic ansatz for perturbations, the Poisson equation (2.11) becomes

$$\nabla^2\varphi_A = -\frac{i\omega\hat{p}}{\bar{a}^2}, \nabla^2\varphi_T = \frac{i\omega(\gamma-1)\bar{\rho}\hat{S}}{\gamma R} \tag{4.26}$$

Similarly, the harmonic ansatz is adopted for the acoustic momentum potential φ_A and thermal momentum potential φ_T. Equation (4.26) is rewritten as

$$-\alpha^2\varphi_A + \frac{\partial^2\varphi_A}{\partial y^2} = -\frac{i\omega\hat{p}}{\bar{a}^2}, -\alpha^2\varphi_T + \frac{\partial^2\varphi_T}{\partial y^2} = \frac{i\omega(\gamma-1)\bar{\rho}\hat{S}}{\gamma R} \tag{4.27}$$

Along with the boundary condition

$$y = 0: \varphi_A = 0, \varphi_T = 0 \tag{4.28}$$

$$y \to \infty: \varphi_A = 0, \varphi_T = 0 \tag{4.29}$$

Equation (4.27) is solved numerically and MPT components are obtained as

$$m_A = -i\alpha\varphi_A, n_A = -\frac{\partial\varphi_A}{\partial y} \tag{4.30}$$

$$m_T = -i\alpha\varphi_T, n_T = -\frac{\partial\varphi_T}{\partial y} \tag{4.31}$$

$$m_B = (\bar{\rho}\hat{u} + \bar{u}\hat{\rho}) - (m_A + m_T), n_B = \bar{\rho}\hat{v} - (n_A + n_T) \tag{4.32}$$

Figure 4-4 shows the scalar potential φ_A and φ_T of the S mode at the synchronization point $x = 0.1m$. The magnitude of φ_T is more than three times of the magnitude of φ_A. The MPT components of the S mode at $x = 0.1m$ are plotted in Figure 4-4. For notational convenience, these components are designated $\boldsymbol{m_B'} = (m_B, n_B)$, $\boldsymbol{m_A'} = (m_A, n_A)$, and $\boldsymbol{m_T'} = (m_T, n_T)$, respectively. The vortical component has the largest magnitude order. The y-component of MPT components at the wall is not vanished, while their sum $m_B + m_A + m_T = (\rho v)' = 0$ at y=0.

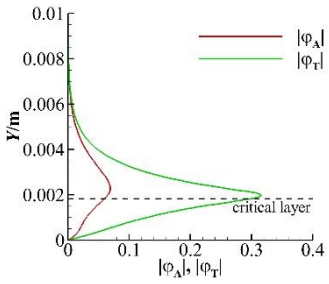

Figure 4-3. The absolute value of acoustic momentum potential φ_A and thermal momentum potential φ_T of untsable Mack's second mode (the S mode) at *x*=0.1m.

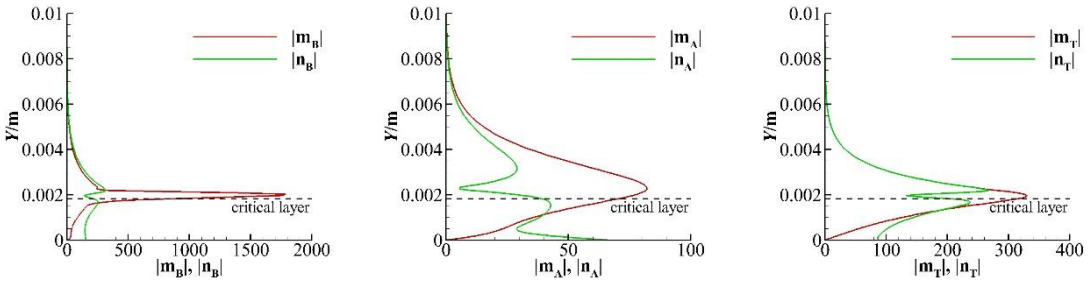

(a) (b) (c)

Figure 4-4. The absolute value of (a) the vortical component, (b) the acoustic component, and (c) the thermal component of unstable Mack's second mode (the S mode) at *x*=0.1m.

4.6 Growth rate analysis of the unstable S mode

Figure 4-5 shows $\boldsymbol{q_x}$ of the S mode at *x*=0.076m (SP1) and *x*=0.1m (SP2). The eigenfunction of the S mode is normalized by the fluctuation pressure $\hat{\boldsymbol{p}}$ at the wall. It is noted that $\boldsymbol{q_x}$ is positive in the lower region of the boundary layer and becomes negative near the critical layer. The magnitude of $\boldsymbol{q_x}$ near the critical layer is much larger than it in other regions. Consequently, the integration term $\int_0^\infty \boldsymbol{q_x} dy$ is negative for the S mode in the spatial LST. $\int_0^\infty \boldsymbol{q_x} dy$ appears in the equation (4.10) as denominator. Eventually, negative source terms destabilize the S mode due to the negative $\int_0^\infty \boldsymbol{q_x} dy$. This counterintuitive result is because $\boldsymbol{q_x}$, which is regards as the "energy" term in integration MPT's energy budget equation, is not positive definite.

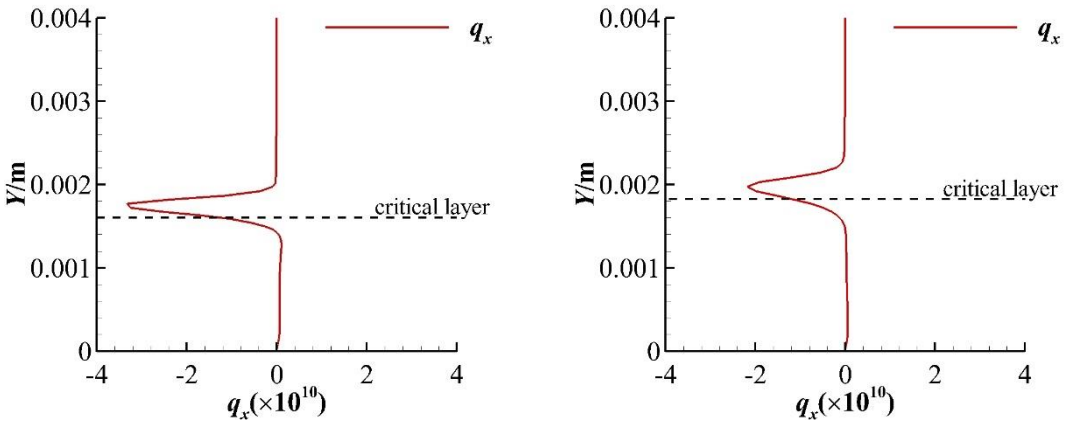

Figure 4-5. q_x of the S mode (mormalized by $\hat{p}$ at the wall) at (a) *x*=0.076m (SP1) and (b) *x*=0.1m (SP2).

Source terms of the (normalized) S mode at *x*=0.076m (SP1) and *x*=0.1m (SP2) are plotted in Figure 4-6(a) and Figure 4-6(b), respectively. Obviously, the vortical source term $\boldsymbol{P_B}$ is always opposite to the thermal source term $\boldsymbol{P_T}$. The acoustic source term $\boldsymbol{P_A}$ is positive at the wall and reach a negative peak near the wall. $\boldsymbol{P_A}$ reaches a positive peak below the critical

layer and becomes negative above the critical layer. The thermal diffusion source term $\boldsymbol{P_{diff}}$ is always negative in the boundary layer. There are two negative peaks in $\boldsymbol{P_{diff}}$. One is in the vicinity of the wall and the other is above the critical layer. Due to the negative integration term $\int_0^\infty \boldsymbol{q_x} dy$, the negative $\boldsymbol{P_{diff}}$ destabilize the S mode, which extract energy from the mean flow for the amplification of the S mode.

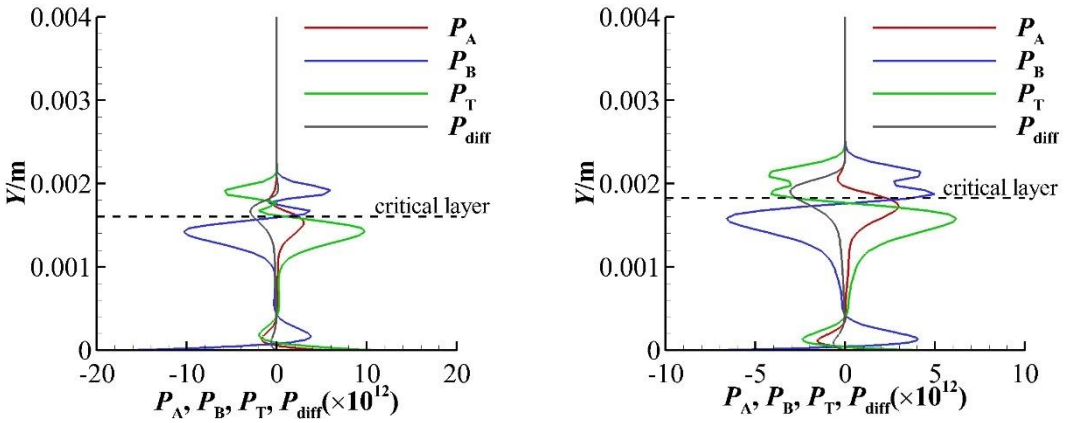

Figure 4-6. Source terms of the S mode (normalized by $\hat{p}$ at the wall) at (a) x=0.076m (SP1) and (b) x=0.1m (SP2).

As defined in equation (4.11), the global contribution of each source term in Mack's second mode is plotted in Figure 4-7(a). Two dotted lines indicate the location of synchronization points. σ_{diff} and σ_B are positive, while σ_A and σ_T are negative. It means that the thermal diffusion source $\boldsymbol{P_{diff}}$ and the vortical source $\boldsymbol{P_B}$ provide energy for the growth of the unstable S mode while $\boldsymbol{P_A}$ and $\boldsymbol{P_T}$ stabilize the S mode. Obviously, σ_A is coupled to σ_{diff} and σ_B is coupled to σ_T. $|\sigma_B|$ and $|\sigma_T|$ reach their peak at the SP1, where the S mode synchronizes with vorticity/entropy waves in the freestream. $|\sigma_{diff}|$ reach its peak at SP2, where the S mode synchronizes with the F mode. $|\sigma_A|$ reach its peak at the downstream of SP2. Figure 4-7(b) shows coupling effects $\sigma_A + \sigma_{diff}$ and $\sigma_B + \sigma_T$. $\sigma_A + \sigma_{diff}$ is positive and

becomes maxmum at the upstream of SP2. $\sigma_B + \sigma_T$ is negative and becomes minimum between SP1 and SP2. Thus, the coupling effect of σ_A and σ_{diff} is responsible to the modal growth of Mack's second mode at SP2. According to above analysis, it is concluded that the thermal diffusion source term $\boldsymbol{P_{diff}}$ plays the key role in the amplification of Mack's second mode at SP2 in the Mach 6.0 boundary layer with the adiabatic wall. σ_{diff} reaches its peak at SP2, which leads to Mack's second mode. Due to the exsitence of σ_A, σ_B,and σ_T, Mack's second mode becomes most unstable at the downstream of the SP2.

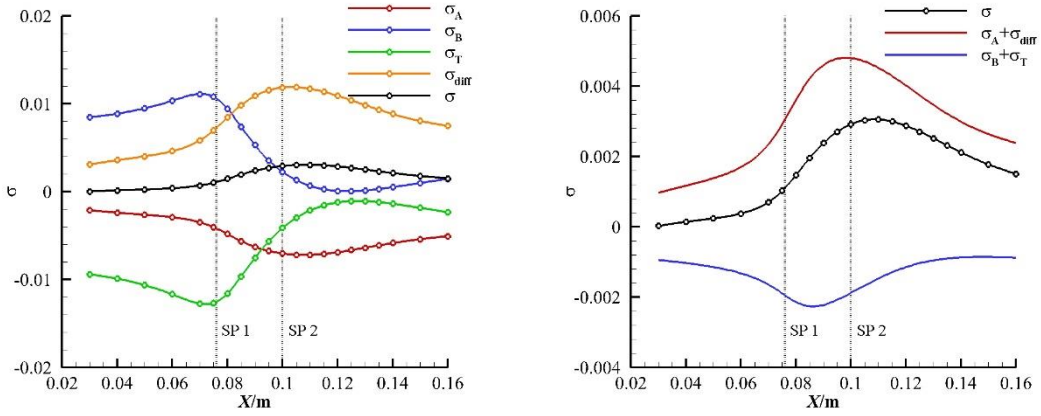

(a) (b)

Figure 4-7. (a) the global contribution of source terms on the growth rate σ; (b) the global contribution of coupling effects $\sigma_A + \sigma_{diff}$ and $\sigma_B + \sigma_T$.

4.7 Thermal diffusion source P_{diff}

Both the vortical source term $\boldsymbol{P_B}$ and the thermal diffusion source term $\boldsymbol{P_{diff}}$ produce energy for the amplification of the unstable S mode in the boundary layer. However, $\boldsymbol{\sigma_B}$ couples with $\boldsymbol{\sigma_T}$ and $\boldsymbol{\sigma_B + \sigma_T}$ is negative. Moreover, $\boldsymbol{\sigma_{diff}}$ becomes largest at SP2. It is generally acknowledged that the synchronization of the S mode and the F mode at SP2 leads to Mack's second mode. Thus, the thermal diffusion source term $\boldsymbol{P_{diff}}$ is the key energy

producer related to Mack's second mode. The thermal diffusion source term $\boldsymbol{P_{diff}}$ is related to the interaction between the fluctuation pressure p' and the fluctuation entropy S'. In Doak's MPT approach, the fluctuation pressure p' is related to the acoustic component while the fluctuation entropy S' is related to the thermal component. $\boldsymbol{P_{diff}}$ represents a thermal acoustic effect that produces energy for the amplification of Mack's second mode. As shown in Figure 4-6, the thermal diffusion source term $\boldsymbol{P_{diff}}$ has two negative peaks in the vicinity of the wall and near the critical layer, which means that the thermal-acoustic effect is significant in these regions.

It is noted that the MPT decomposition is based on the linearized mass conservation equation while the energy budget equation is based on the linearized momentum conservation equation. The question arises naturally that how the linearized energy conservation equation affects the energy balance described in the energy budget equation.

Firstly, considering the energy conservation equation in a usual standard form

$$(\rho T)\left[\frac{\partial S}{\partial t} + (\boldsymbol{u}\cdot\nabla)S\right] = \Phi \tag{4.33}$$

Here, $\Phi = \nabla\cdot(k\nabla T) + \overline{\overline{\boldsymbol{S}}}\cdot(\nabla\boldsymbol{u})$ includes the thermal conduction effect and viscous dissipation effect. Then, the linearization of equation (4.33) for a 2D parallel shear flow with unique mean pressure gives

$$\bar{\rho}\bar{T}\left(\frac{\partial s'}{\partial t} + \bar{u}\frac{\partial s'}{\partial x} + v'\frac{\partial \bar{s}}{\partial y}\right) = \Phi' \tag{4.34}$$

The 2D parallel shear flow with unique mean pressure is a typical assumption for boundary layer flow.

Equation (4.34) can be rewritten as

$$\frac{\partial s'}{\partial t} + \bar{u}\frac{\partial s'}{\partial x} = -v'\frac{\partial \bar{s}}{\partial y} + \frac{\Phi'}{\bar{\rho}\bar{T}} \tag{4.35}$$

The left-hand side of equation (4.35) is the change rate of the fluctuation entropy observed in the reference frame with the mean velocity. The first term on the right-hand side of equation (4.35), $-v'\frac{\partial \bar{S}}{\partial y}$, is entropy exchange between neighbor layers with different mean entropy due to disturbance velocity, while the second term $\frac{\Phi'}{\bar{\rho}\bar{T}}$ is the fluctuation entropy generated in the irreversible process.

Considering disturbances with the harmonic waveform, equation (4.35) is rewritten as

$$\hat{S} = -\frac{\hat{v}}{i(\alpha\bar{u}-\omega)}\frac{\partial \bar{S}}{\partial y} + \frac{1}{\bar{\rho}\bar{T}}\frac{\hat{\Phi}}{i(\alpha\bar{u}-\omega)} \tag{4.36}$$

Equation (4.36) is valid for non-neutral instability waves. For a neutral instability wave, $\alpha\bar{u} - \omega = 0$ at the critical layer. However, what we concern about is the physical mechanism of unstable Mack's second mode. The neutral instability wave case is not taken into consideration in this study.

Furthermore, two new variables are introduced into the analysis of the fluctuation entropy

$$\frac{\partial \eta}{\partial t} + \bar{u}\frac{\partial \eta}{\partial x} = v', \frac{\partial \Psi'}{\partial t} + \bar{u}\frac{\partial \Psi'}{\partial x} = \Phi' \tag{4.37}$$

The dimension of the variable η is displacement and the dimension of the variable Φ' is energy per unit volume. The harmonic waveform of v' and Φ' gives

$$\hat{\eta} = \frac{\hat{v}}{i(\alpha\bar{u}-\omega)}, \hat{\Psi} = \frac{\hat{\Phi}}{i(\alpha\bar{u}-\omega)} \tag{4.38}$$

And, we have

$$\hat{S} = -\hat{\eta}\frac{\partial \bar{S}}{\partial y} + \frac{\hat{\Psi}}{\bar{\rho}\bar{T}} \tag{4.39}$$

Thus, the fluctuation entropy S' can be expressed as the sum of two parts

$$S' = -\eta\frac{\partial \bar{S}}{\partial y} + \frac{\Psi'}{\bar{\rho}\bar{T}} \tag{4.40}$$

The first part is fluctuation entropy caused by fluctuation displacement between neighbor

layers with different mean entropy. The second part is fluctuation entropy due to the viscous effect. Thus, the fluctuation entropy S' is split into the inviscid part $S'_{inv} = -\eta \frac{\partial \bar{S}}{\partial y}$ and the viscous part $S'_{vis} = \frac{\Psi'}{\bar{\rho}\bar{T}}$.

Finally, the time average of $\frac{p'}{R}$ and $\frac{\partial S'}{\partial t}$ gives the thermal diffusion source term

$$P_{diff} = \overline{\frac{p'}{R}\frac{\partial S'}{\partial t}} = -\overline{\frac{p'}{R}\frac{\partial \eta}{\partial t}}\frac{\partial \bar{S}}{\partial y} + \frac{1}{\bar{p}}\overline{p'\frac{\partial \Psi'}{\partial t}} \tag{4.41}$$

The first part $-\overline{\frac{p'}{R}\frac{\partial \eta}{\partial t}}\frac{\partial \bar{S}}{\partial y}$ is the inviscid thermal-acoustic effect denoted as P_{inv} and the second part $\frac{1}{\bar{p}}\overline{p'\frac{\partial \Psi'}{\partial t}}$ is the viscous thermal-acoustic effect denoted as P_{vis}.

Figure 4-8 shows the $\frac{P_{diff}}{Q_x}$, $\frac{P_{inv}}{Q_x}$, and $\frac{P_{vis}}{Q_x}$ of the S mode at x=0.076m (SP1) and x=0.1m (SP2). Here, $Q_x = \int_0^\infty q_x dy$ is the integration of q_x. $\frac{P_{diff}}{Q_x}$ has two positive peaks near the wall and the critical layer, which indicates the thermal-acoustic effect is significant in these two regions. $\frac{P_{diff}}{Q_x}$ almost overlaps $\frac{P_{vis}}{Q_x}$ near the wall. The viscous effect P_{vis} dominates P_{diff} near the wall, while P_{inv} is negligible here. $\frac{P_{vis}}{Q_x}$ near the wall is almost the same at SP1 and SP2. $\frac{P_{inv}}{Q_x}$ has a positive peak at the critical layer, while $\frac{P_{vis}}{Q_x}$ has a negative peak here. P_{inv} destabilizes the S mode around the critical layer, while P_{vis} stabilizes the S mode here.

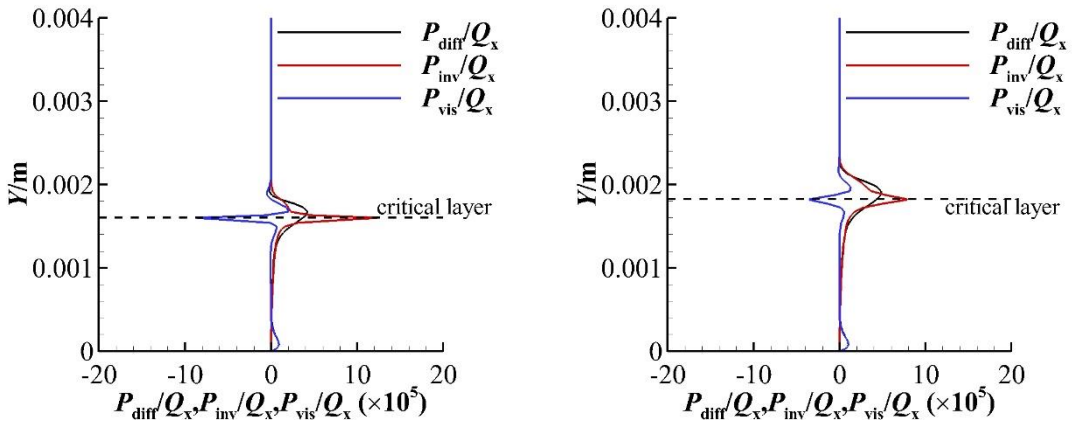

Figure 4-8. $\frac{P_{diff}}{Q_x}$, $\frac{P_{inv}}{Q_x}$, and $\frac{P_{vis}}{Q_x}$ of the S mode at x=0.076m (SP1) and x=0.1m (SP2).

Another concern is the relation between the thermal diffusion source P_{diff} and the

dilatation term ($\nabla \cdot \boldsymbol{u}'$), which is important in the previous research of Tian and Wen [53]. It is noted that

$$\Phi' = \bar{\rho}\bar{T}\left(\frac{\partial S'}{\partial t} + \bar{u}\frac{\partial S'}{\partial x} + v'\frac{\partial \bar{S}}{\partial y}\right) = \frac{\gamma R}{\gamma - 1}\bar{\rho}\left(\frac{\partial T'}{\partial t} + \bar{u}\frac{\partial T'}{\partial x} + v'\frac{\partial \bar{T}}{\partial y}\right) - \left(\frac{\partial p'}{\partial t} + \bar{u}\frac{\partial p'}{\partial x}\right) \tag{4.42}$$

As shown in Tian and Wen [53],

$$\bar{\rho}\left(\frac{\partial T'}{\partial t} + \bar{u}\frac{\partial T'}{\partial x} + v'\frac{\partial \bar{T}}{\partial y}\right) = -(\gamma - 1)\left(\frac{\partial u'}{\partial x} + \frac{\partial v'}{\partial y}\right) + \frac{k(\gamma - 1)}{R}\frac{\partial^2 T'}{\partial y^2} + \varepsilon \tag{4.43}$$

ε is a negligible term. By substituting equation (4.44) into equation (4.42), we have

$$\Phi' = -\gamma R\left(\frac{\partial u'}{\partial x} + \frac{\partial v'}{\partial y}\right) + \gamma k\frac{\partial^2 T'}{\partial y^2} - \left(\frac{\partial p'}{\partial t} + \bar{u}\frac{\partial p'}{\partial x}\right) + \frac{\gamma R}{\gamma - 1}\varepsilon \tag{4.44}$$

The dilatation term is included in Φ' and affects P_{vis}. The observation that P_{vis} is dominant near the wall is consistent with the result of Tian and Wen [53].

4.8 Summary

In this chapter, the integral energy budget equation is developed to study the modal growth rate of the S mode in the Mach 6.0 boundary layer with the adiabatic wall. The vortical source and the thermal diffusion source destabilize the S mode, while the acoustic source and the thermal source stabilize the S mode. It is found that σ_A is coupled to σ_{diff} and σ_B is coupled to σ_T. $\sigma_B + \sigma_T$ is negative while $\sigma_A + \sigma_{diff}$. $|\sigma_B|$ and $|\sigma_T|$ reach their peak at the SP1, where the S mode synchronizes with vorticity/entropy waves in the freestream. $|\sigma_{diff}|$ reach its peak at SP2, where the S mode synchronizes with the F mode. $|\sigma_A|$ reach its peak downstream of SP2. Therefore, the instability mechanism of Mack's second mode (the unstable S mode around SP2) is related to the thermal diffusion source P_{diff}. The thermal diffusion source P_{diff} is caused by the interaction between the fluctuation pressure and the fluctuation entropy, which is thus a thermal-acoustic effect. Based on the linearization energy

equation, the thermal diffusion source P_{diff} is split into the inviscid part P_{inv} and the viscous part P_{vis}. The inviscid thermal diffusion source P_{inv} is related to the exchange between neighbor layers with different mean entropy, while the viscous thermal diffusion source P_{vis} is related to the thermal conduction and viscous dissipation. P_{diff} is significant near the wall and around the critical layer. P_{vis} almost overlaps P_{diff} and destabilizes the S mode near the wall. P_{inv} is dominant around the critical layer and destabilizes the S mode, while P_{vis} is also significant and stabilizes the S mode at the critical layer.

5. MPT analysis of acoustic metasurfaces

5.1 Acoustic metasurface

Ultrasonic absorptive coating (UAC) is an effective method to suppress the Mack second mode composed of regular or irregular microcavities. Meanwhile, UAC has minimal effects on the mean flow among various passive/active transition control strategies. Typically, UAC dissipates the Mack second mode disturbance energy through the viscosity in the narrow micropores and hence stabilizes the BL.

The concept of the acoustic metasurface is introduced by Zhao, et al. [46] as the extension of UAC to suppress the Mack second mode and stabilize the hypersonic boundary layer (HBL). Acoustic metasurfaces are planar metamaterial structures composed of monolayer or multilayer stacks of subwavelength building blocks. In this sense, UAC is one form of acoustic metasurface that dissipates disturbance energy via its absorption characteristics. However, in addition to absorption capability, a metasurface can exhibit artificially designed acoustic characteristics, such as wave-front modulation, sound insulation, and so on [65, 66]. The impedance-near-zero acoustic metasurface proposed by Zhao, et al. [46] can effectively suppress the Mack second mode via out-of-phase behavior between the incident and reflected waves. Recently, Zhao, et al. [67] further proposed the reflection-controlled acoustic metasurface composed of periodical subwavelength groove groups that can change the reflection direction of disturbance waves.

Although the stabilizing effects of various acoustic metasurfaces on HBL have been proven, the physics-based analysis of these multi phenomena is still unclear. Thus, the MPT approach is

applied to clarify the fundamental mechanism of acoustic metasurfaces to suppress the Mack second mode instability.

5.2 Direct numerical simulation

In this study, the disturbance flowfield of the Mach 6.0 boundary layer with the solid wall, absorptive metasurface, impedance-near-zero metasurface, and reflection-controlled metasurface is obtained by the two-dimensional DNS. The DNS method can be referred to in section 3.2. The unit Reynolds number was $1.05\times10^{7}m^{-1}$. The freestream temperature and wall temperatures were 43.18 K and 300 K, respectively. The blow-suction disturbance is located at x=0.01m~0.015m. The blow-suction frequency is fixed at 138.74kHz.

Figure 5-1 shows the 2-D (absorptive and impedance-near-zero) acoustic metasurface with subwavelength grooves schematically. The 2-D reflection-controlled metasurface with subwavelength grooves is plotted in Figure 5-2 schematically. The structure parameters of acoustic metasurfaces in the DNS are listed in table 5-1. Acoustic metasurfaces are placed at x=0.12m~0.18m in the 2D DNS.

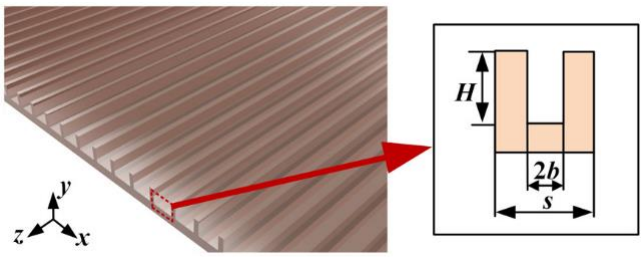

Figure 5-1. Schematic illustration of (absorptive and impedance-near-zero) acoustic metasurface with subwavelength grooves. *H* and b are the depth and half-width of the cavity. *s* is the cavity spacing.

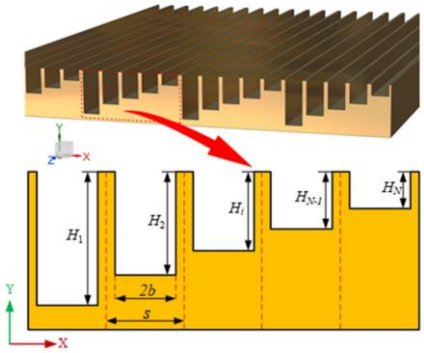

Figure 5-2. Schematic illustration of reflection-controlled metasurface with subwavelength grooves.

Table 5-1. Structure parameters of acoustic metasurfaces

	H(mm)	b(mm)	*s*(mm)
absorptive metasurface	1.633	0.196	0.5158
impedance-near-zero metasurface	0. 55466	0.416	1.04
reflection-controlled metasurface	1.056; 0.7904; 0.6246; 0.4676;0.2642	0.196	0.4946

5.3 Acoustic characteristic of acoustic metasurfaces

Before considering the hypersonic flowfield, the full-wave finite element simulations are performed to examine the acoustic characteristics of the designed metasurfaces in quiescent air using COMSOL Multiphysics®. For completeness, the contours of all kinds of surfaces are presented in Figure 5-3. The x' coordinate in the streamwise direction and the y' coordinate normal to the wall are normalized by the reference flat-plate length of 0.2 m. The amplitude of reflected waves on the absorptive metasurface is minimal, which strongly proves its absorption characteristics. The amplitude of reflected waves on the impedance-near-zero metasurface is smaller than on the rigid surface. It can't be ignored that the pattern of the

reflection-controlled metasurface is quite different from other coatings, the reflected waves propagate upstream in the direction parallel to the surface. The full-wave finite element simulations show acoustic wave manipulation characteristics of each metasurface.

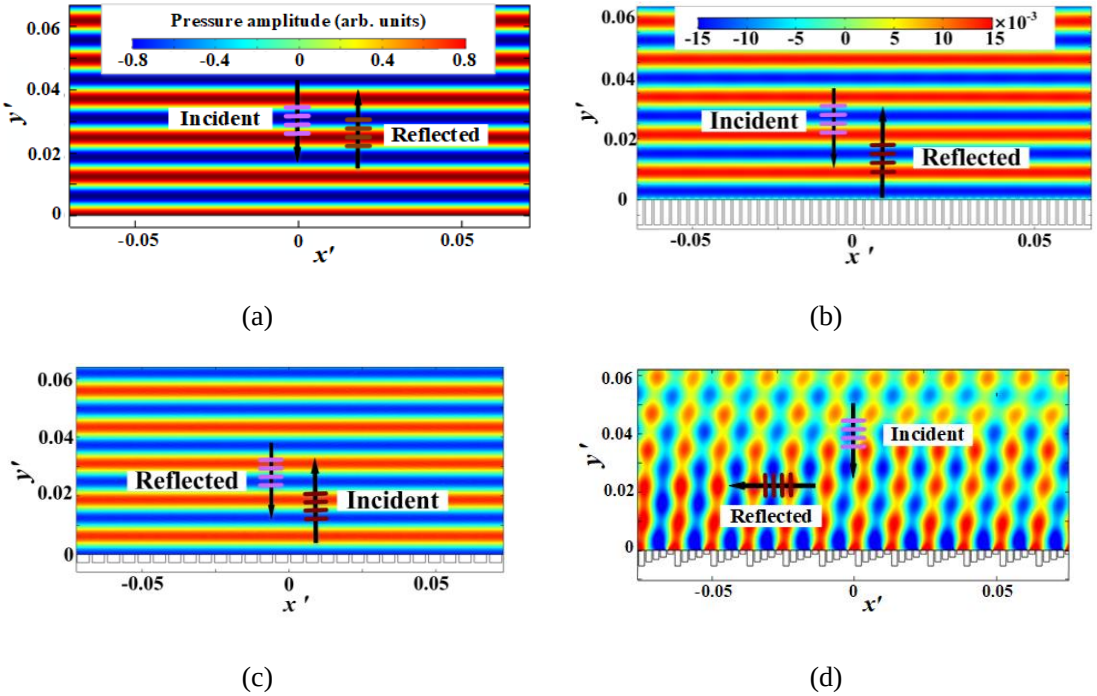

Figure 5-3. Simulated scattered pressure fields for various acoustic metasurfaces in the absence of hypersonic fluid flow: (a) rigid surface, (b) absorptive metasurface, (c) impedance-near-zero metasurface, (d) reflection-controlled metasurface.

5.4 Mean flow

It is necessary to assess whether the mean flow has changed or been affected. This is an important question to be addressed to explore the real cause of the change in the growth rate of Mack's second mode. With this in mind, the mean flow on the rigid surface and acoustic metasurfaces are compared. As shown in Figure 5-4, the profiles of velocity and temperature above the metasurfaces are consistent with those above the rigid surface, which indicates the designed metasurfaces have little effect on the mean flow field.

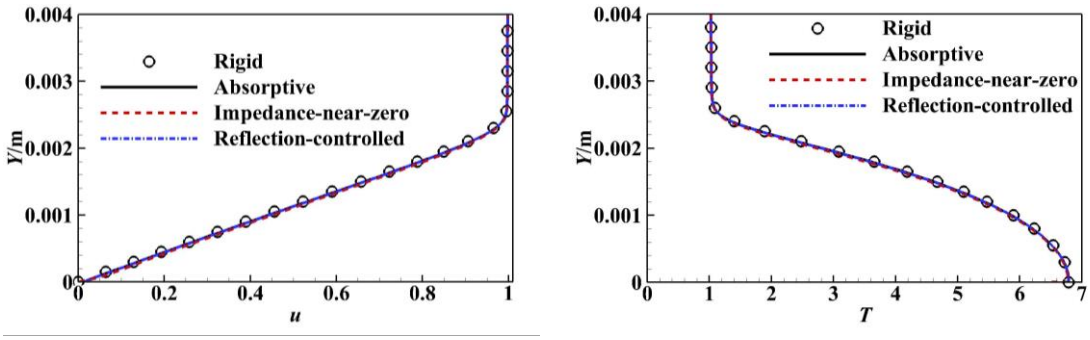

(a) (b)

Figure 5-4. Comparisons of streamwise velocity and temperature profiles at x = 0.15m: (a) streamwise velocity profile and (b) temperature profile.

5.5 Disturbance flow field

The instantaneous fluctuating pressure contours for all cases are shown in Figure 5-5. The typical "two-cell" structure is observed on a rigid surface in Figure 5-5a. After x=0.11 m, the fluctuations are considerably amplified, which indicates the domination of Mack's second mode. Notably, x=0.11 m corresponded to the synchronization point of the discrete modes predicted by the LST. However, on the acoustic metasurfaces, the "two-cell" patterns are destroyed in different ways. For the absorptive metasurface case (Figure 5-5b), the upper mode cells tend to fuse with the lower parts and the trailing legs sink into the microgrooves. For the impedance-near-zero metasurface (Figure 5-5c), the trailing leg moves within the cavity. For reflection-controlled metasurface, the mode structures are divided into several segments in the normal direction as shown in Figure 5-5d.

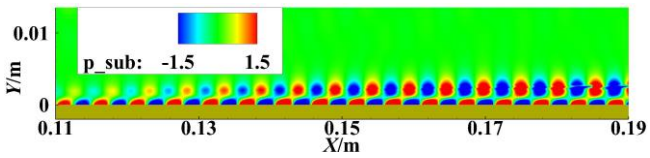

(a)

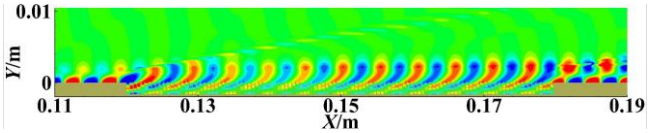

(b)

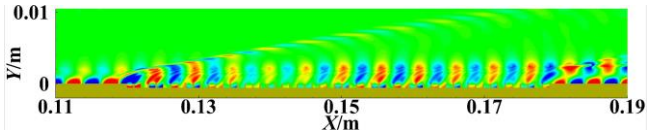

(c)

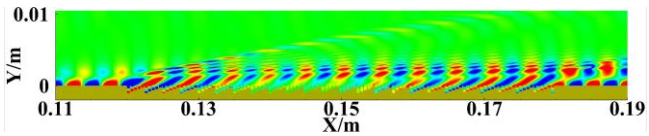

(d)

Figure 5-5. Fluctuating pressure contours for (a) rigid surface, (b) absorptive metasurface, (c) impedance-near-zero metasurface, (d) reflection-controlled metasurface.

Figure 5-6 shows the streamwise variation of the upper envelope of maximum fluctuating pressure on the wall. The fluctuating pressure is greatly reduced when passing through the acoustic metasurfaces. After the acoustic metasurfaces, the amplitude rises quickly. It is thought the destruction of Mack second mode propagation pattern in the BL inhabiting its growth rate and stabilize the BL.

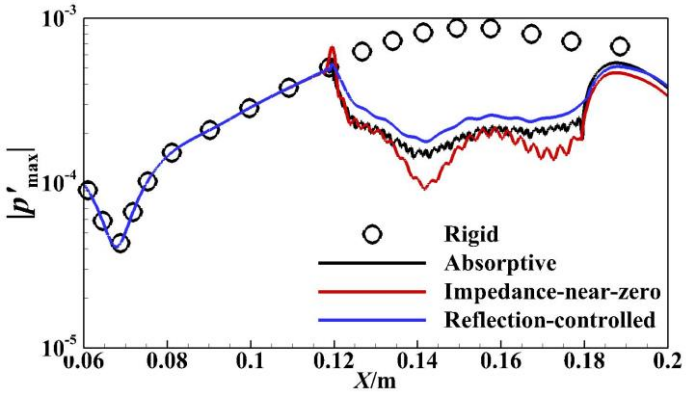

Figure 5-6. Streamwise variation of the upper envelope of maximum fluctuating pressure for various surfaces.

5.6 Growth rate analysis

In the growth rate analysis of the S mode in the spatial LST in Chapter 4, it is noted that

$$\frac{\partial\overline{(\rho u)'H'}}{\partial x} = -2\alpha_i\overline{(\rho u)'H'} \tag{5.1}$$

The growth rate of the S mode is $\sigma = -\alpha_i$. Equation (5.1) is strictly valid with the parallel flow assumption. In DNS results, the boundary layer thickness is growing as *x* increases. With the local parallel assumption, the growth rate σ_2 in the rigid surface case is defined as

$$\sigma_2 = \frac{1}{2\int_0^\infty q_x dy}\frac{\partial q_x}{\partial x} \tag{5.2}$$

Here, $q_x = \overline{(\rho u)'H'}$.

Similar to equation (4.11), the contribution of each source term to the growth rate σ_2 is

$$\sigma_{2A} = \frac{\int_0^\infty P_A dy}{2\int_0^\infty q_x dy}, \sigma_{2B} = \frac{\int_0^\infty P_B dy}{2\int_0^\infty q_x dy}, \sigma_{2T} = \frac{\int_0^\infty P_T dy}{2\int_0^\infty q_x dy}, \sigma_{2diff} = \frac{\int_0^\infty P_{diff} dy}{2\int_0^\infty q_x dy} \tag{5.3}$$

For the DNS with acoustic metasurfaces, the definition of growth rate σ_2 is not suitable. Considering a 2-D parallel shear flow over acoustic metasurfaces with regular micro-structure, the mean flow field is periodic with the unit cell period *s*. According to Floquet theory, the 2-D disturbance wave can be expressed in the form

$$\tilde{\phi}(x, y, t) = \hat{\phi}(x, y)e^{i(\alpha x - \omega t)} \tag{5.4}$$

Here, $\hat{\phi}(x, y) = \hat{\phi}(x + T_p, y)$ is the periodic function with the period T_p. $T_p = s$ for absorptive metasurfaces and impedance-near-zero metasurface, while $T_p = 5s$ for reflection-controlled metasurfaces.

Similar to equation (4.4), the time-average of any two disturbance terms can be expressed as

$$\overline{a'b'} = \left(\hat{a}\hat{b}^* + \hat{a}^*\hat{b}\right)e^{-2\alpha_i x} \tag{5.5}$$

Here, $\hat{a}(x, y)$ and $\hat{b}(x, y)$ are the periodic function with the period *s*. Thus, we have

$$\overline{a'b'}\big|_{x+T_p} = \overline{a'b'}\big|_x e^{-2\alpha_i T_p} \tag{5.6}$$

The growth rate $\sigma = -\alpha_i$ in the parallel shear flow over acoustic metasurface satisfies that

$$\sigma = \frac{1}{2s} ln\left(\frac{\overline{a'b'}|_{x+T_p}}{\overline{a'b'}|_x}\right) \tag{5.7}$$

The integration of the energy budget equation (2.29) over a unit cell gives

$$\int_0^\infty q_x dy\Big|_{x_0}^{x_0+T_p} = \oint P_A dS + \oint P_B dS + \oint P_T dS + \oint P_{diff} dS \tag{5.8}$$

With equation (5.7) and the local parallel assumption, the growth rate σ_3 in DNS of acoustic metasurfaces is defined as

$$\sigma_3 = \frac{1}{2s} ln\left(\frac{\int_0^\infty q_x dy\big|_{x+T_p}}{\int_0^\infty q_x dy\big|_x}\right) \tag{5.9}$$

Therefore, the contribution of each source term to the growth rate σ_3 is

$$e^{2\sigma_{3A}T_p} - 1 = \frac{\oint P_A dS}{\int_0^\infty q_x dy\big|_x} \Longrightarrow \sigma_{3A} = \frac{1}{2T_p} ln\left(\frac{\oint P_A dS}{\int_0^\infty q_x dy\big|_x} + 1\right) \tag{5.10}$$

$$e^{2\sigma_{3B}T_p} - 1 = \frac{\oint P_B dS}{\int_0^\infty q_x dy\big|_x} \Longrightarrow \sigma_{3B} = \frac{1}{2T_p} ln\left(\frac{\oint P_B dS}{\int_0^\infty q_x dy\big|_x} + 1\right) \tag{5.11}$$

$$e^{2\sigma_{3T}T_p} - 1 = \frac{\oint P_T dS}{\int_0^\infty q_x dy\big|_x} \Longrightarrow \sigma_{3T} = \frac{1}{2T_p} ln\left(\frac{\oint P_T dS}{\int_0^\infty q_x dy\big|_x} + 1\right) \tag{5.12}$$

$$e^{2\sigma_{3diff}T_p} - 1 = \frac{\oint P_{diff} dS}{\int_0^\infty q_x dy\big|_x} \Longrightarrow \sigma_{3diff} = \frac{1}{2T_p} ln\left(\frac{\oint P_{diff} dS}{\int_0^\infty q_x dy\big|_x} + 1\right) \tag{5.13}$$

Figure 5-7 plots the contribution of each source term to the growth rate on various surfaces. The growth rate σ_2/σ_3 is suppressed over acoustic metasurfaces. However, σ_2/σ_3 is still positive and disturbance waves still grow over acoustic metasurfaces. This result is different from the fluctuation pressure distribution along the wall, as plotted in Figure 5-6. Similar to the growth rate analysis of the S mode plotted in Figure 4-7, σ_{2B}/σ_{3B} couples with σ_{2T}/σ_{3T}, while σ_{2A}/σ_{3A} couples with $\sigma_{2diff}/\sigma_{3diff}$. $\sigma_{2diff}/\sigma_{3diff}$ and σ_{2B}/σ_{3B} is positive, while σ_{2A}/σ_{3A} and σ_{2T}/σ_{3T} is negative. $\sigma_{2diff}/\sigma_{3diff}$ is larger than σ_{2A}/σ_{3A} in magnitude, and σ_{2B}/σ_{3B} is smaller than σ_{2T}/σ_{3T} in magnitude. Therefore, the thermal diffsion source P_{diff} is still critical to the

amplification of disturbances waves in the DNS results with the rigid surface and acoustic measurfaces.

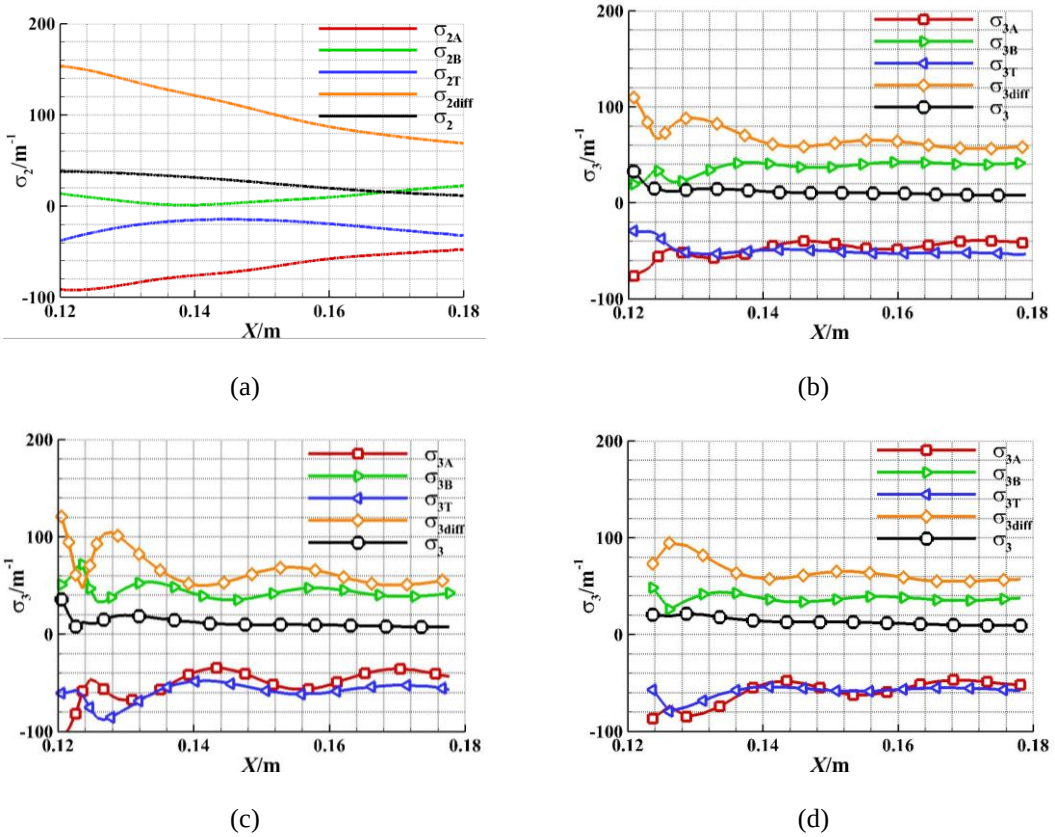

Figure 5-7. Contribution of each source term to the growth rate on various surfaces based on DNS results: (a) rigid surface, (b) absorptive metasurface, (c) impedance-near-zero metasurface, (d) reflection-controlled metasurface.

5.7 Source mechanisms

The quantitative analysis of the contribution of each source term to the growth rate over the rigid surface and acoustic metasurface indicates that the thermal diffusion source plays a key role in the amplification of disturbance waves. There is no qualitative difference in the case with different acoustic metasurface.

Acoustic source terms $\boldsymbol{P_A}$ over the rigid surface and acoustic metasurfaces are plotted in

Figure 5-8. It should be addressed again that the negative source term leads to a positive growth rate and causes instability in HBL. In most areas, the acoustic source terms are close to zero. The positive/negative source terms that affect the growth rate of disturbance are mainly located at the wall and near the critical layer. In Figure 5-8b, 5-7c, and 5-7d, the negative acoustic source terms near the wall are attenuated due to microcavities. The effect of microcavities on acoustic source terms $\boldsymbol{P_A}$ here stabilizes disturbance waves. However, positive acoustic source terms appear at y~0.0025m in Figure 5-8b, 5-7c, and 5-7d. The effect of microcavities on acoustic source terms $\boldsymbol{P_A}$ here destabilizes disturbance waves. Periodic structure appears around the critical layer is apparent in Figure 5-8d.

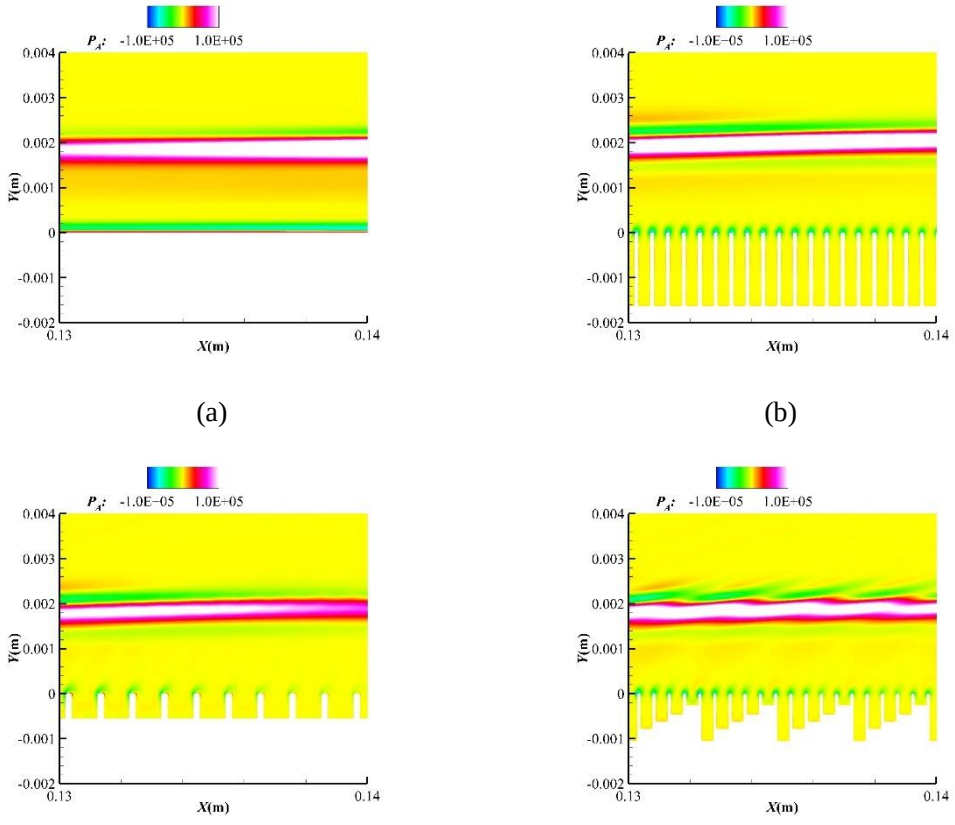

Figure 5-8. Acoustic source term P_A over (a) rigid surface, (b) absorpotive metasurface, (c) impedance-near-zero metasurface, and (d) reflection-controlled metasurface.

Vortical source terms $\boldsymbol{P_B}$ over rigid surface and acoustic metasurfaces are plotted in Figure 5-9. Similarly, the positive vortical source terms near the wall are attenuated due to microcavities in Figure 5-9b, 5-8c, and 5-8d. The effect of microcavities on vortical source terms $\boldsymbol{P_B}$ here destabilizes disturbance waves. The attenuation effect in Figure 5-9c is most significant. The periodic structure also appears around the critical layer in Figure 5-9d.

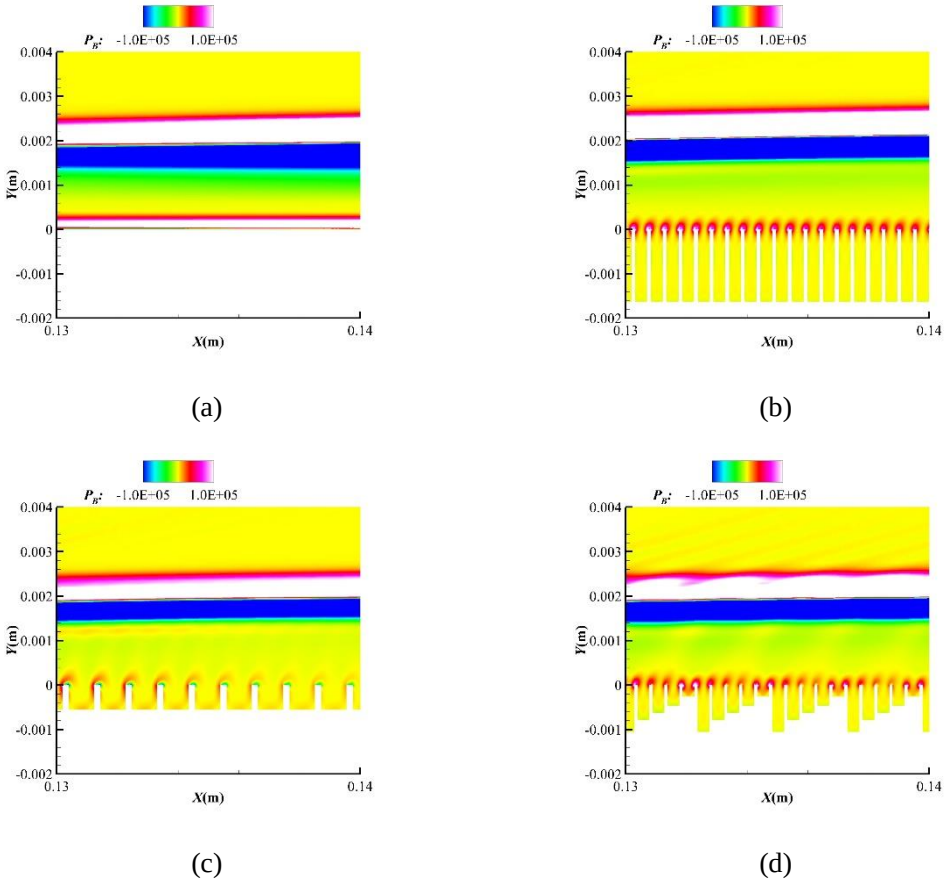

Figure 5-9. Vortical source term $\boldsymbol{P_B}$ over (a) rigid surface, (b) absorpotive metasurface, (c) impedance-near-zero metasurface, and (d) reflection-controlled metasurface.

Thermal source terms $\boldsymbol{P_T}$ over the rigid surface and acoustic metasurfaces are plotted in Figure 5-10. Similarly, the negative thermal source terms near the wall are attenuated due to microcavities in Figure 5-10b, 5-9c, and 5-9d. The effect of microcavities on thermal source terms $\boldsymbol{P_T}$ here stabilizes disturbance waves. Thermal source terms $\boldsymbol{P_T}$ even change to be

positive at the wall between microcavities in Figure 5-10c. Periodic perturbation to the thermal source term around the critical layer is not significant in Figure 5-10d.

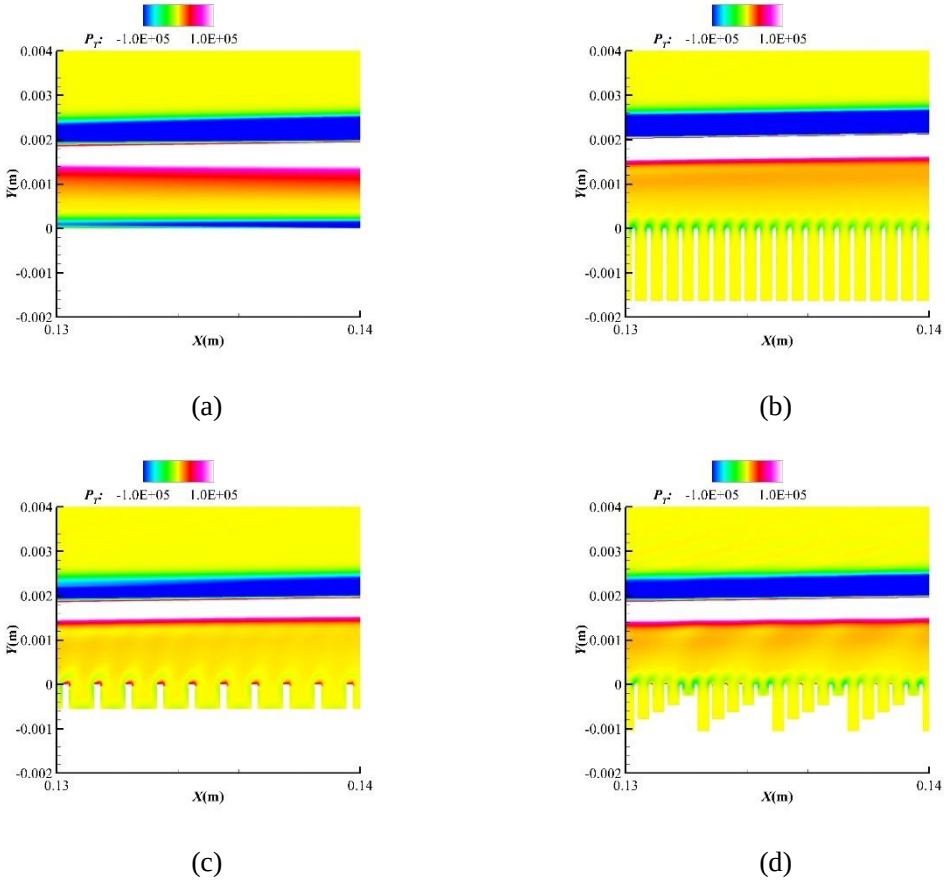

Figure 5-10. Thermal source term P_T over (a) rigid surface, (b) absorpotive metasurface, (c) impedance-near-zero metasurface, and (d) reflection-controlled metasurface.

Thermal diffusion source terms $\boldsymbol{P_{diff}}$ over rigid surface and acoustic metasurfaces are plotted in Figure 5-11. The quantitative analysis of the growth rate in section 5.6 suggests that the thermal diffusion source terms $\boldsymbol{P_{diff}}$ are critical in the amplification of disturbance waves. Thus, the effect of microcavities on the thermal diffusion source is the key to explain the stabilization mechanism of different acoustic metasurfaces. In Figure 5-11a, it is observed that thermal diffusion source terms $\boldsymbol{P_{diff}}$ over the rigid surface are negative in the whole flow field and have the largest magnitude near the wall and around the critical layer. In Figure

5-11b, 5-10c, and 5-10d, the negative thermal diffusion source terms $\boldsymbol{P_{diff}}$ are attenuated significantly near the wall due to microcavities. The effect of microcavities on thermal source terms $\boldsymbol{P_{diff}}$ here stabilizes disturbance waves. The attenuation effect of microcavities is weakest over the reflection-controlled metasurface and strongest over the impedance-near-zero metasurface. In Figure 5-11b, thermal diffusion source terms $\boldsymbol{P_{diff}}$ become positive with small amplitude at y~0.0016m. In Figure 5-11c, thermal diffusion source terms $\boldsymbol{P_{diff}}$ become positive with relatively larger magnitude around y~0.0014m. In Figure 5-11d, periodic spots of positive thermal diffusion source terms $\boldsymbol{P_{diff}}$ with the largest magnitude appear below and above the critical layer.

The thermal diffusion source $\boldsymbol{P_{diff}}$ is the time average of $\frac{p'}{R}$ and $\frac{\partial s'}{\partial t}$. p' is related to sound waves reflected back and forth in the boundary layer flow field. Acoustic metasurfaces change the boundary condition of sound waves at the wall. Thus, all three kinds of metasurfaces have a significant effect on $\boldsymbol{P_{diff}}$ near the wall**.** However, the property of reflected sound waves caused by microcavities is different in different metasurfaces. For absorptive metasurfaces, the incident sound wave is dissipated in the narrow and deep cavity and no sound wave is reflected back. As a consequence, $\boldsymbol{P_{diff}}$ around the critical layer is affected slightly by absorptive metasurfaces. For impedance-near-zero and reflection controlled metasurfaces, incident sound wave is reflected intensely by microcavities. Consequently, the phase difference between $\frac{p'}{R}$ and $\frac{\partial s'}{\partial t}$ near the critical layer is affected significantly in impedance-near-zero and reflection controlled metasurface cases. By changing the direction of reflected sound wave in the reflection controlled metasurface case, $\boldsymbol{P_{diff}}$ above the critical layer is even affected significantly by reflected sound waves.

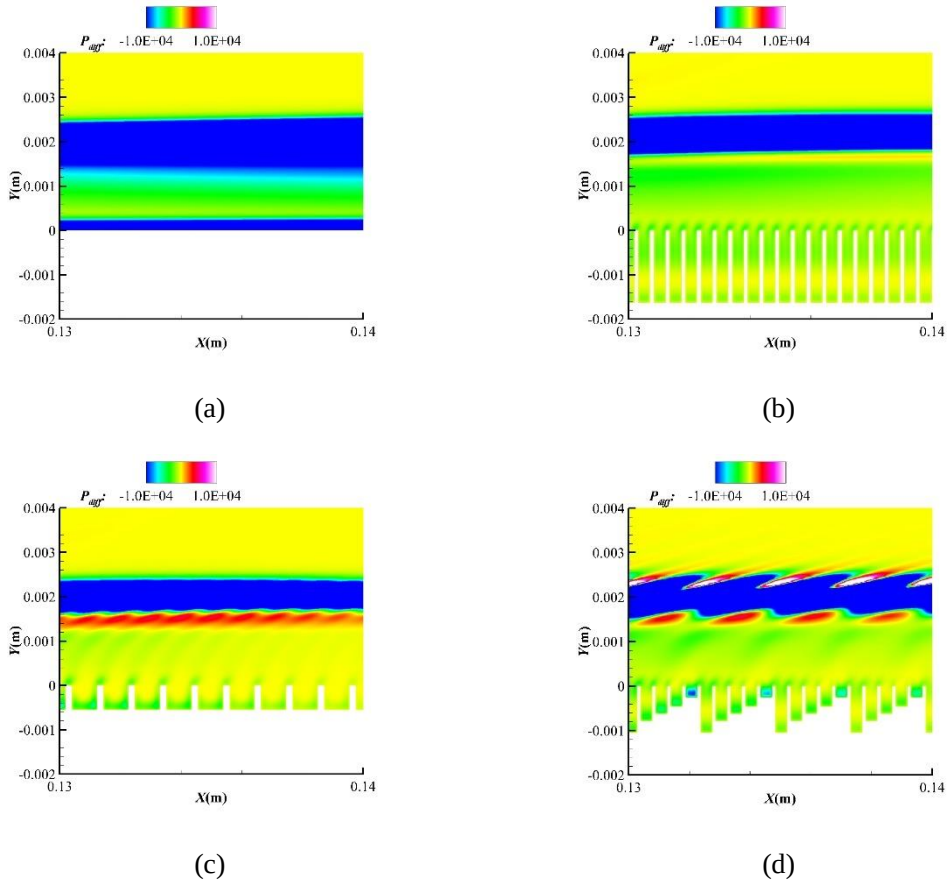

Figure 5-11. Thermal diffusion source term P_{diff} over (a) rigid surface, (b) absorpotive metasurface, (c) impedance-near-zero metasurface, and (d) reflection-controlled metasurface.

5.8 Summary

In this chapter, the stabilization mechanism of acoustic metasurfaces in the Mach 6.0 boundary layer is studied through the MPT approach. The growth rate σ_2 and σ_3 for rigid surface and acoustic metasurfaces, respectively, are defined based on the integrated energy budget equation. The qualitative analysis of the contribution of each source term indicates that thermal diffusion source terms P_{diff} play a key role in the amplification of disturbance waves. Contours of thermal diffusion source terms P_{diff} provide an intuitive interpretation of the stabilization

mechanism of different acoustic metasurfaces. In the rigid surface case, thermal diffusion source terms P_{diff} reach negative peaks near the wall and around the critical layer. In acoustic metasurface cases, thermal diffusion source terms P_{diff} are attenuated by microcavities. The attenuation effect is strongest in the impedance-near-zero case and weakest in the reflection-controlled case. The effect of microcavities on thermal diffusion source terms P_{diff} around the critical layer is insignificant in the absorptive metasurface case, while it is significant in the impedance-near-zero metasurface case and the reflection-controlled metasurface. Thermal diffusion source terms P_{diff} changes to positive around y~0.0014m over the impedance-near-zero metasurface. Spots of positive thermal diffusion source terms P_{diff} with very large amplitude appears periodically above and below the critical layer over the reflection-controlled metasurface. It is concluded that 1) the stabilization mechanism of the absorptive metasurface is mainly the attenuation effect near the wall due to microcavities; 2) the stabilization mechanism of the impedance-near-zero metasurface includes the attenuation effect near the wall and the effect on thermal diffusion source terms below the critical layer; 3) the reflection-controlled metasurface has the weakest attenuation effect near the wall but the strongest effect on thermal diffusion source terms around the critical layer.

6. Conclusions

The momentum potential theory (MPT) is applied to the study of the physical mechanism of hypersonic boundary layer instabilities. The MPT approach is an elegant method that provides a decomposition to instability waves in a general flow field and obtains an energy budget equation governing the development of instability waves. However, there is ambiguity in the original MPT approach proposed by Doak [54], which restricts the application of the MPT approach. To overcome the restriction, three independent energy budget equations are developed to clarify the sound radiation mechanism of the supersonic mode. Then, the MPT approach is applied to the study of the modal growth of instability waves. The difficulty in this problem is that the growth rate of instability waves is not related to the energy budget equation explicitly. For this reason, the integrated energy budget equation is developed to clarify the effect of source terms on the growth rate. It is found that the thermal diffusion source term plays a key role in the modal growth of instability waves. Furthermore, the integrated energy budget equation is adopted to provide a physical interpretation of the stabilization mechanism of different acoustic metasurfaces. The results indicate that the stabilization mechanism of different acoustic metasurfaces is attributed to the attenuation effect on thermal diffusion source terms near the wall and the effect on thermal diffusion source terms around the critical layer.

6.1 Recommendations for Future Work

The present work represents an exploratory study of hypersonic boundary instabilities in the MPT framework. As such, this work should be viewed as laying the foundation for more

future work in depth. Some suggestions are provided here to guide future efforts.

Firstly, the application of the MPT approach to the study of instabilities in the reacting flow. The chemical reaction is significant in high-enthalpy wind tunnel experiments and some real-flight cases. The existence of chemical reactions causes complicated instabilities in the flow field. It has been mentioned that the MPT approach can be extended to the multi-chemical-components flow directly. It is interesting and worthwhile to explore the physical mechanism underlying the instabilities caused by chemical reactions in the MPT framework.

Secondly, the application of the MPT approach to the study of instabilities in the nonlinear stage. In the present work, only the linear instability of the boundary layer with small disturbances assumption is considered. Although the linear assumption simplifies the MPT decomposition process and the derivation of the energy budget equation in a great deal, the MPT approach itself is not limited to the linear case. The continuity equation (2.1) is linear for the momentum density $\boldsymbol{m}$, the MPT decomposition is thus valid in nonlinear cases. MPT energy budget equation in nonlinear cases can be derived as following. The scalar product of equation (2.21) and the momentum density $\boldsymbol{m}$ gives

$$\boldsymbol{m}\cdot\frac{\partial \boldsymbol{u}}{\partial t}+\boldsymbol{m}\cdot\nabla H=\boldsymbol{m}\cdot\boldsymbol{\alpha} \tag{6.1}$$

Equation (6.1) can be rewritten as

$$\frac{\partial}{\partial t}\left(\frac{1}{2}\rho\boldsymbol{u}\cdot\boldsymbol{u}\right)+\nabla\cdot(\boldsymbol{m}H)+h\frac{\partial \rho}{\partial t}=\boldsymbol{m}\cdot\boldsymbol{\alpha} \tag{6.2}$$

The time average of equation (6.2) is

$$\nabla\cdot(\overline{\boldsymbol{m}}\overline{H})+\overline{h\frac{\partial \rho}{\partial t}}=\overline{\boldsymbol{m}\cdot\boldsymbol{\alpha}} \tag{6.3}$$

Equation (6.3) can be expressed as

$$\nabla\cdot\left(\overline{\boldsymbol{m}'H'}+\bar{\boldsymbol{m}}\bar{H}\right)+\overline{h'\frac{\partial \rho'}{\partial t}}=\overline{\boldsymbol{m}'\cdot\boldsymbol{\alpha}'}+\bar{\boldsymbol{m}}\cdot\bar{\boldsymbol{\alpha}} \tag{6.4}$$

The time average of equation (2.21) is

$$\nabla \bar{H} = \bar{\boldsymbol{\alpha}} \tag{6.5}$$

The scalar product of equation (6.5) and $\bar{\boldsymbol{m}}$ gives

$$\nabla \cdot (\bar{\boldsymbol{m}} \bar{H}) = \bar{\boldsymbol{m}} \cdot \bar{\boldsymbol{\alpha}} \tag{6.6}$$

Substituting equation (6.6) into equation (6.4) gives

$$\nabla \cdot \left(\overline{\boldsymbol{m}' H'}\right) + \overline{h' \frac{\partial \rho'}{\partial t}} = \overline{\boldsymbol{m}' \cdot \boldsymbol{\alpha}'} \tag{6.7}$$

The energy budget equation in nonlinear cases is the same as equation (2.29) in the linear cases. Thus, the MPT approach is promised in the study of the physical mechanisms of nonlinear instabilities, such as secondary instability, bypass mechanism, breakdown, etc. However, three independent energy budget equations for each MPT component are no longer valid without linear assumption.

6.2 Final word

The present work is one small step in the understanding of the complicated physic mechanism of hypersonic boundary layer instabilities and the laminar flow control in the hypersonic flow. There are still many difficulties in this area from the fundamental physics to the practical engineering. Hopefully, the on-going experimental, computational and theoretical investigations will deepen our understanding of the mystery of the boundary layer transition and leads to the realization of the space travel dream in the future.

References

[1] K. F. Stetson and G. H. Rushton, "Shock Tunnel Investigation of Boundary-Layer Transition," *AIAA Journal*, vol. 5, no. 5, pp. 899-906, 1967.

[2] J. M. Kendall, "Supersonic Boundary Layer Stability Experiments," in *Boundary Layer Transition Study Group Meeting*, Aerospace Corp., San Bernardino, Calif., 1967.

[3] J. M. Kendall, "Wind Tunnel Experiments Relating to Supersonic and Hypersonic Boundary-Layer Transition," *AIAA Journal*, vol. 13, no. 3, pp. 290-299, 1975.

[4] K. F. Stetson, E. R. Thompson, J. C. Donaldson, and L. G. Siler, "Laminar Boundary Layer Stability Experiments on a Cone at Mach 8. Part I: Sharp cone," *AIAA Paper*, pp. 83-1761, 1983.

[5] K. F. Stetson, E. R. Thompson, J. C. Donaldson, and L. G. Siler, "Laminar Boundary Layer Stability Experiments on a Cone at Mach 8. Part II: Blunt Cone," *AIAA Paper*, pp. 84-0006, 1984.

[6] K. F. Stetson, E. R. Thompson, J. C. Donaldson, and L. G. Siler, "Laminar Boundary Layer Stability Experiments on a Cone at Mach 8. Part III: Sharp cone at Angle of Attack," *AIAA Paper*, pp. 85-0492, 1985.

[7] K. F. Stetson, E. R. Thompson, J. C. Donaldson, and L. G. Siler, "Laminar Boundary Layer Stability Experiments on a Cone at Mach 8. Part IV: On Unit Reynolds Number and Enviromental Effects," *AIAA Paper*, pp. 86-1087, 1986.

[8] K. F. Stetson, E. R. Thompson, J. C. Donaldson, and L. G. Siler, "Laminar Boundary Layer Stability Experiments on a Cone at Mach 8. Part V: Tests With a Cooled Model," *AIAA Paper*, pp. 89-1895, 1989.

[9] A. D. Kosinov, A. A. Maslov, and S. G. Shevelkov, "Experiments on the stability of supersonic laminar boundary layers," *Journal of Fluid Mechanics*, vol. 219, 1990.

[10] S. J. Laurence, A. Wagner, and K. Hannemann, "Experimental study of second-mode instability growth and breakdown in a hypersonic boundary layer using high-speed schlieren visualization," *Journal of Fluid Mechanics*, vol. 797, pp. 471-503, 2016.

[11] R. E. Kennedy, S. J. Laurence, M. S. Smith, and E. C. Marineau, "Visualization of the second-mode instability on a sharp cone at Mach 14," in *2018 AIAA Aerospace Sciences Meeting*, 2018, p. 2083.

[12] S. J. Laurence *et al.*, "Time-Resolved Visualization of Instability Waves in a Hypersonic Boundary Layer," (in English), *Aiaa Journal*, vol. 50, no. 1, pp. 243-246, Jan 2012.

[13] S. J. Laurence, A. Wagner, and K. Hannemann, "Schlieren-based techniques for investigating instability development and transition in a hypersonic boundary layer," *Experiments of Fluids*, 2014.

[14] L. M. Mack, "Boundary-layer linear stability theory," in *AGARD Conference*, NATO, Paris, 1984, vol. 224, pp. 1-1 - 1-22.

[15] M. R. Malik, "Prediction and control of transition in supersonic and

hypersonic boundary layers," *AIAA Journal,* vol. 27, no. 11, pp. 1487-1493, 1989.

[16] H. L. Reed, W. Saric, and D. Arnal, "Linear stability theory applied to boundary layers," *Annual Review of Fluid Mechanics,* no. 28, pp. 389-482, 1996.

[17] M. R. Malik, "Numerical methods for hypersonic boundary layer stability," *Journal of Computational Physics,* vol. 86, no. 2, pp. 376-413, 1990.

[18] A. V. Fedorov and A. Tumin, "High-Speed Boundary-Layer Instability: Old Terminology and a New Framework," *AIAA Journal,* vol. 49, no. 8, pp. 1647-1657, 2011.

[19] A. V. Fedorov and A. P. Khokhlov, "Prehistory of Instability in a Hypersonic Boundary Layer," *Theoretical and Computational Fluid Dynamics,* vol. 14, pp. 359-375, 2001.

[20] G. Erlebacher and M. Y. Hussaini, "Numerical experiments in supersonic boundary-layer stability," *Physics of Fluids A: Fluid Dynamics,* vol. 2, no. 1, pp. 94-104, 1990.

[21] Y. Ma and X. Zhong, "Receptivity of a supersonic boundary layer over a flat plate. Part 1. Wave structures and interactions," *Journal of Fluid Mechanics,* vol. 488, pp. 31-78, 2003.

[22] Y. Ma and X. Zhong, "Receptivity of a supersonic boundary layer over a flat plate. Part 2. Receptivity to free-stream sound," *Journal of Fluid Mechanics,* vol. 488, pp. 79-121, 2003.

[23] Y. Ma and X. Zhong, "Receptivity of a supersonic boundary layer over a flat plate. Part 3. Effects of different types of free-stream disturbances," *Journal of Fluid Mechanics,* vol. 532, pp. 63-109, 2005.

[24] X. Zhong and X. Wang, "Direct Numerical Simulation on the Receptivity, Instability, and Transition of Hypersonic Boundary Layers," *Annual Review of Fluid Mechanics,* vol. 44, no. 1, pp. 527-561, 2012.

[25] A. Tumin, X. Zhong, and X. Zhong, "Numerical simulation and theoretical analysis of perturbations in hypersonic boundary layers," *AIAA journal,* vol. 49, no. 3, pp. 463-471, 2011.

[26] A. M. Tumin, X. Wang, and X. Zhong, "Direct numerical simulation and the theory of receptivity in a hypersonic boundary layer," 2007.

[27] A. V. Fedorov, "Transition and Stability of High-Speed Boundary Layers," *Annual Review of Fluid Mechanics,* no. 43, pp. 79-95, 2011.

[28] M. Morkovin, E. Reshotko, and T. Herbert, "Transition in open flow systems: a reassessment," *Bull. Am. Phys. Soc,* vol. 39, no. 9, p. 1882, 1994.

[29] P. V. Chuvakhov and A. V. Fedorov, "Spontaneous radiation of sound by instability of a highly cooled hypersonic boundary layer," *Journal of Fluid Mechanics,* vol. 805, pp. 188-206, 2016.

[30] N. Malmuth *et al.*, "Problems in high speed flow prediction relevant to control," *AIAA Paper,* vol. 2695, p. 1998, 1998.

[31] A. V. Fedorov, N. D. Malmuth, A. Rasheed, and H. G. Hornung, "Stabilization of Hypersonic Boundary Layers by Porous Coatings," *AIAA Journal,* vol. 39, no. 4, pp. 605-610, 2001.

[32] A. V. Fedorov, A. Shiplyuk, A. Maslov, E. Burov, and N. Malmuth, "Stabilization of a hypersonic boundary layer using an ultrasonically absorptive coating,"

Journal of Fluid Mechanics, vol. 479, pp. 99-124, 2003.

[33] A. Fedorov and N. Malmuth, "Parametric studies of hypersonic laminar flow control using a porous coating of regular microstructure," in *46th AIAA Aerospace Sciences Meeting and Exhibit*, 2008, p. 588.

[34] A. Fedorov, G. Brès, M. Inkman, and T. Colonius, "Instability of Hypersonic Boundary Layer on a Wall with Resonating Micro-Cavities," in *49th AIAA Aerospace Sciences Meeting including the New Horizons Forum and Aerospace Exposition*, 2011.

[35] A. Rasheed, H. G. Hornung, A. V. Fedorov, and N. D. Malmuth, "Experiments on Passive Hypervelocity Boundary-Layer Control Using an Ultrasonically Absorptive Surface," *AIAA Journal*, vol. 40, no. 3, pp. 481-489, 2002.

[36] X. Wang and X. Zhong, "Numerical simulations on mode S growth over feltmetal and regular porous coatings of a Mach 5.92 flow," in *49th AIAA Aerospace Sciences Meeting including the New Horizons Forum and Aerospace Exposition*, 2011, p. 375.

[37] D. Bountin *et al.*, "Stabilization of a hypersonic boundary layer using a wavy surface," *AIAA journal*, vol. 51, no. 5, pp. 1203-1210, 2013.

[38] A. Wagner, M. Kuhn, J. Martinez Schramm, and K. Hannemann, "Experiments on passive hypersonic boundary layer control using ultrasonically absorptive carbon–carbon material with random microstructure," *Experiments in Fluids*, vol. 54, no. 10, 2013.

[39] G. A. Brès, M. Inkman, T. Colonius, and A. V. Fedorov, "Alternate Designs of Ultrasonic Absorptive Coatings for Hypersonic Bounday Layer Control," *AIAA Paper*, vol. 4217, p. 2009, 2009.

[40] Bres *et al.*, "Second-mode attenuation and cancellation by porous coatings in a high-speed boundary layer," *Journal of Fluid Mechanics*, vol. 726, pp. 312–337, 2013.

[41] I. Egorov, A. Novikov, and A. Fedorov, "Direct numerical simulation of supersonic boundary layer stabilization using grooved wavy surface," in *48th AIAA Aerospace Sciences Meeting*, 2010, pp. 2010-1245.

[42] A. Maslov *et al.*, "Hypersonic Laminar Flow Control Using a Porous Coating of Random Microstructure," *AIAA paper*, vol. 1112, p. 2006, 2006.

[43] R. C. Tritarelli, S. K. Lele, and A. Fedorov, "Stabilization of a hypersonic boundary layer using a felt-metal porous coating," *Journal of Fluid Mechanics*, vol. 769, pp. 729-739, 2015.

[44] X. Tian, R. Zhao, T. Long, and C. Y. Wen, "Reverse Design of Ultrasonic Absorptive Coating for the Stabilization of Mack Modes," *AIAA Journal*, vol. 57, no. 6, pp. 2264-2269, 2019.

[45] R. Zhao, T. Liu, C. Y. Wen, J. Zhu, and L. Cheng, "Theoretical Modeling and Optimization of Porous Coating for Hypersonic Laminar Flow Control," *AIAA Journal*, vol. 56, no. 8, pp. 2942-2946, 2018.

[46] R. Zhao, T. Liu, C. Y. Wen, J. Zhu, and L. Cheng, "Impedance-Near-Zero Acoustic Metasurface for Hypersonic Boundary-Layer Flow Stabilization," *Physical Review Applied*, vol. 11, no. 4, 2019.

[47] R. Zhao, C. Y. Wen, T. H. Long, X. D. Tian, and Y. Wu, "Spatial Direct Numerical Simulation of the Hypersonic Boundary-Layer Stabilization Using Porous

Coatings," *AIAA Journal,* vol. 57, no. 1, pp. 1-5, 2019.

[48] R. Zhao, C. Y. Wen, X. D. Tian, T. H. Long, and W. Yuan, "Numerical simulation of local wall heating and cooling effect on the stability of a hypersonic boundary layer," *International Journal of Heat & Mass Transfer,* vol. 121, pp. 986-998, 2018.

[49] R. Zhao, X. X. Zhang, and C. Y. Wen, "Theoretical Modeling of Porous Coatings with Simple Microstructures for Hypersonic Boundary-Layer Stabilization," *AIAA Journal,* vol. 58, no. 2, pp. 1-6, 2019.

[50] X. Wang and X. Zhong, "Phase angle of porous coating admittance and its effect on boundary-layer stabilization," in *41st AIAA Fluid Dynamics Conference and Exhibit*, 2011, p. 3080.

[51] O. Reynolds, "On the Dynamical Theory of Incompressible Viscous Fluids and the Determination of the Criterion," *Philosophical Transactions of the Royal Society A,* vol. 186, pp. 123-164, 1895.

[52] J. J. Kuehl, "Thermoacoustic interpretation of second-mode instability," *AIAA Journal,* vol. 56, no. 9, pp. 3585-3592, 2018.

[53] X. Tian and C. Wen, "Growth mechanisms of second-mode instability in hypersonic boundary layers," *Journal of Fluid Mechanics,* vol. 908, 2021.

[54] P. Doak, "Momentum potential theory of energy flux carried by momentum fluctuations," *Journal of sound and vibration,* vol. 131, no. 1, pp. 67-90, 1989.

[55] S. Unnikrishnan and D. V. Gaitonde, "Interactions between vortical, acoustic and thermal components during hypersonic transition," *Journal of Fluid Mechanics,* vol. 868, pp. 611-647, 2019.

[56] L. Kovásznauy, "Turbulence in supersonic flow," *Journal of the Aeronautical Sciences,* vol. 20, pp. 657-682, 1953, Art. no. 10.

[57] N. Bitter and J. Shepherd, "Stability of highly cooled hypervelocity boundary layers," *Journal of Fluid Mechanics,* vol. 778, pp. 586-620, 2015.

[58] C. P. Knisely and X. Zhong, "Supersonic Modes in Hot-Wall Hypersonic Boundary Layers with Thermochemical Nonequilibrium Effects," in *2018 AIAA Aerospace Sciences Meeting*, 2018, p. 2085.

[59] C. P. Knisely and X. Zhong, "Significant Supersonic Modes and the Wall Temperature Effect in Hypersonic Boundary Layers," *AIAA Journal,* vol. 57, no. 4, pp. 1552-1566, 2018.

[60] C. P. Knisely and X. Zhong, "Sound radiation by supersonic unstable modes in hypersonic blunt cone boundary layers. I. Linear stability theory," *Physics of Fluids,* vol. 31, no. 2, p. 024103, 2019.

[61] C. P. Knisely and X. Zhong, "Sound radiation by supersonic unstable modes in hypersonic blunt cone boundary layers. II. Direct numerical simulation," *Physics of Fluids,* vol. 31, no. 2, p. 024104, 2019.

[62] C. H. Mortensen, "Toward an understanding of supersonic modes in boundary-layer transition for hypersonic flow over blunt cones," *Journal of Fluid Mechanics,* vol. 846, pp. 789-814, 2018.

[63] S. Unnikrishnan and D. V. Gaitonde, "Instability characteristics of cooled hypersonic boundary layers," in *AIAA Scitech 2020 Forum*, 2020, p. 0588.

[64] A. M. Tumin, "Three-dimensional spatial normal modes in compressible boundary layers," *Journal of Fluid Mechanics*, vol. 586, pp. 295-322, 2007.

[65] Y. Li, X. Jiang, B. Liang, J. C. Cheng, and L. Zhang, "Metascreen-Based Acoustic Passive Phased Array," *Physical Review Applied*, vol. 4, no. 2, p. 024003, 2015.

[66] M. Kim, W. Lee, C. I. Park, and J. H. Oh, "Elastic wave energy entrapment for reflectionless metasurface," *Physical Review Applied*, 2020.

[67] R. Zhao, Y. Dong, X. Zhang, C. Wen, T. Long, and W. Yuan, "Control of Reflected Waves with Acoustic Metasurfaces for Hypersonic Boundary-Layer Stabilization," *AIAA Journal*, vol. 59, no. 6, pp. 1893-1898, 2021.